

Self-Assembled Monolayers as Wettability Modifiers

by
Tianlang Yu

A dissertation submitted to the Department of Chemistry,
College of Natural Sciences and Mathematics
in partial fulfillment of the requirements for the degree of

DOCTOR OF PHILOSOPHY

in Chemistry

Chair of Committee: T. Randall Lee

Committee Member: Thomas Teets

Committee Member: Jakoah Brgoch

Committee Member: Steven Baldelli

Committee Member: Ramon Colorado

University of Houston
December 2020

Copyright 2020, Tianlang Yu

ACKNOWLEDGMENTS

First and foremost, I am deeply grateful to my research advisor Professor T. Randall Lee. I would also like to extend my gratitude to my committee members Dr. Brgoch, Dr. Thomas Teets, Steven Baldelli, and Dr. Ramon Colorado for the time taken out of their busy day to review this dissertation.

I would like to thank the Lee group members for their professional and friendship since the first day I joined the group. I would like to give my special thanks to Dr. Maria Maquez for her kindness and help with all my papers and dissertation. I would also like to thank Dr. Oussama Zenasni, Dr. Yi-Ting Chen, Dr. Chulsoon Park, Dr. Amin Shakiba, Dr. Tingting Liu, Dr. Daniela Deleon, Dr. Johnson Hoang, Dr. Lydia St. Hill, Dr. Riddhiman Medhi, Dr. Pannaree Srinoi, and Dr. Hung-Vu Tran for their valuable guidance of my research. I would like to thank the other Lee group members: Siwakorn Sakunkaewkasem (Will), Yunsoo Choi, Jiyoung Lee, Nhat Ngo, Pooria Tajalli, Mina Omidian, Kontee Thongthai, Jong Moon Lee, Minh Nguyen, Jia Shiang Liao, Marvin Valverde. I am also grateful for all my friends in Houston.

Finally, I would like to thank my family for their support in these years. I would not have come this far without their loves.

Thank you for everything,

Tianlang Yu

ABSTRACT

This dissertation investigates the development of new nanoscale coatings in the form of self-assembled monolayers (SAMs) used as surface wettability modifiers. The aim of this research is to use SAMs to mimick polymer surfaces (PE and PTFE), alter the interfacial properties of gold surfaces, and microstructure GaAs substrates for transistors and solar cells.

In the first study, the synthesis of two cyclohexyl-terminated alkanethiols (**HCyHnSH**; $n = 10$ and 11) and their fluorinated analogs $C_6F_{11}(CH_2)_nSH$ ($n = 10$ and 11 ; **FCyHnSH**) was performed. These ring-terminated adsorbates were used to generate self-assembled monolayers (SAMs) on gold surfaces to serve as model polymeric interfaces on metal substrates. Comparison of the contact angles of a wide range of contacting liquids on these SAMs and their polymeric analogs, polyethylene (PE) and polytetrafluoroethylene (PTFE), found that these liquids exhibited similar wettability on the **HCyHnSH** SAMs and PE surfaces, and separately on the **FCyHnSH** SAMs and PTFE surfaces.

The second study investigates two types of mixed self-assembled monolayers (SAMs) derived from adsorbates having cyclohexyl and phenyl tailgroups mixed with their perfluorinated analogs, respectively. The XPS results suggest that the relative solubility and steric bulkiness of the tail group moiety are two major contributions to the observed preferential adsorption. Moreover, the homogeneously mixed surfaces and precise-controlled surface composition were achieved by the mixture of adsorbates terminated with the phenyl tailgroup and its perfluorinated analog, which show a linear relationship between the mole fraction on the surface and the mole fraction in solution.

In the third study, we investigate six different monodentate and bidentate alkanethiols on GaAs surfaces, used for surface passivation. The results show the bidentate alkanethiols exhibit excellent stability and can be used as a new type of material for the surface passivation of GaAs. Finally, we developed a new microstructuring method for GaAs substrates, reverse patterning lithography (RPL), which combines the use of microcontact printing (μ CP) of a custom-designed fluorinated adsorbate on GaAs and the deposition of a polymeric resin as a wet-etching resist. Positive pattern formation on GaAs wafers of various designed shapes with sharp edges were obtained using the RPL technique. The RPL method benefits from being cost-effective and time-efficient compared to conventional photolithography and has the potential for use in the fabrication of various GaAs devices, including photovoltaics, light-emitting diodes, and microwave and radio-frequency transistors.

Table of Contents

ACKNOWLEDGMENTS	iii
ABSTRACT	iv
Table of Contents	vi
List of Tables	x
List of Schemes	xi
List of Figures	xii
Chapter 1: Crosslinked Self-Assembled Monolayers: Formation and Applications	1
1.1. Introduction	1
1.2. Aromatic Thiol-Based SAMs.....	3
1.2.1. Formation.....	5
1.2.2. Electron-Beam Lithography.....	8
1.2.3. Surface Functionalization	10
1.2.4 Surface-Initiated Polymerization	12
1.2.5 Carbon Nanomembranes (CNMs)	14
1.3. Olefinic- and Acetylenic-Based Alkanethiols.....	18
1.3.1 Formation.....	18
1.3.2 Photolithography.....	23
1.3.3 SAM-Coated Nanoparticles	23
1.3.4 Single-Layer Polydiacetylene Fabrication	24
1.4. Other Aliphatic alkanethiols.....	25
1.4.1 Formation.....	25
1.4.2 Electron-Beam Lithography.....	26
1.5. Silane-Based Alkanethiols	27

1.5.1	Formation	27
1.5.2	Surface-Initiated Polymerization	28
1.5.3	Surface Passivation	30
1.6.	Crosslinked SAMs realized by hydrogen bonding.....	32
1.7.	Boronic Acid-Based Alkanethiols.....	34
1.8	Summary	36
Chapter 2: Mimicking Polymer Surfaces Using Cyclohexyl- and Perfluorocyclohexyl-Terminated Self-Assembled Monolayers.....		37
2.1.	Introduction	37
2.2.	Experimental Procedures.....	42
2.2.1.	Materials and Methods.....	42
2.2.2.	Synthesis of the Adsorbates	43
2.2.3.	Preparation and Characterization of the SAMs	50
2.3.	Results and Discussion.....	52
2.3.1.	Ellipsometric Thickness Measurements.	52
2.3.2.	Analysis of the Chemical Composition of the Films Using XPS.	54
2.3.3.	Assessment of Chain Conformational Order Using PM-IRRAS.....	57
2.3.4.	Contact Angle Measurements.....	60
2.4.	Conclusions	64
Chapter 3: SAMs on Gold Derived from Adsorbates Having Cyclohexyl and Phenyl Tailgroups Mixed with their Phase-Incompatible Perfluorinated Analogs		65
3.1.	Introduction	65
3.2.	Experimental Procedures.....	67

3.2.1. Materials and Methods.....	67
3.2.2. Adsorbate Synthesis.....	68
3.2.3. Preparation and Characterization of the SAMs	71
3.3. Results and Discussion.....	72
3.3.1. Ellipsometric Thickness Measurements.	73
3.3.2. XPS Composition Analysis and Packing of the SAMs.	74
3.3.3. Assessment of Chain Conformational Order Using PM-IRRAS.....	81
3.3.4 Contact Angle Measurements.....	83
3.4. Conclusions	85
Chapter 4: Surface Passivation of GaAs using Bidentate Alkanethiols	87
4.1. Introduction	87
4.2. Experimental Procedures.....	90
4.2.1. Materials and Methods.....	90
4.2.3. Preparation and Characterization of the SAMs on GaAs	91
4.3. Results and Discussion.....	93
4.3.1. Ellipsometric Thickness Measurements.	93
4.3.2. Contact Angle Measurements.....	94
4.3.3. XPS Analysis of the Composition and Packing of SAMs.....	98
4.4. Conclusions	105
Chapter 5: Microstructuring GaAs Using Reverse-Patterning Lithography: Implications for Transistors and Solar Cells	107
5.1. Introduction	107
5.2. Experimental Section	110

5.2.1 Materials	110
5.2.2 Fabrication of PDMS Stamps	111
5.2.3 Microcontact Printing Procedure	111
5.2.4 Characterization of the PFPDT-Printed GaAs	111
5.3. Results and Discussion.....	112
5.3.1 Analysis of PFPDT SAM Composition on GaAs Using XPS.....	112
5.3.2 Analysis of the Lithography Results.....	117
5.4. Conclusions	119
Chapter 6: Conclusions	120
Bibliography	123

List of Tables

	<u>Page</u>
2.1 Ellipsometric thicknesses of the H18SH , HCyHnSH , and FCyHnSH SAMs	52
2.2 XPS Binding Energies (eV) and Relative Chain Packing Densities of the investigated SAMs	55
2.3 Peak Assignments (cm-1) for the PM-IRRAS Spectra of the H18SH , HCyHnSH , and FCyHnSH SAMs	59
2.4 Advancing Contact Angles (θ_a , °) of the Investigated SAMs and Polymers Using Various Probe Liquids	61
3.1 Absorbate Mole Fraction in Solution Used to Generate the Corresponding Mixed SAMs	72
3.2 Ellipsometric Thicknesses of the Three Investigated Mixed SAMs	73
3.3 Relative Packing Densities (%) ^a of the Mixed SAMs as Determined by XPS	77
4.1 Ellipsometric thicknesses of SAMs on GaAs derived from the investigated alkanethiols	93
4.2 Advancing contact angles of the investigated SAMs against water and hexadecane and surface energies of the investigated surfaces	95
4.3 Peak assignment and binding energies (eV) from XPS spectra of bare GaAs and PF PDT SAM on GaAs (100) by stamping	100
5.1 Peak Assignment and Binding Energies (eV) from XPS Spectra of the Bare GaAs and PF PDT -Printed GaAs(100) Surfaces	115
5.2 Ellipsometric Thickness of the PF PDT SAM, Advancing Contact Angles of Water and Diiodomethane on the Investigated Surfaces, and Surface Energies of the Investigated Surfaces	116

List of Schemes

	<u>Page</u>
2.1 Illustration of the investigated SAMs, HCyHnSH (left) and FCyHnSH (right), on gold that mimic PE and PTFE interfaces	40
2.3 Synthetic route for the preparation of 10-cyclohexyldecane-1-thiol (HCy10SH) and 11-cyclohexylundecane-1-thiol (HCyH11SH)	43
2.3 Synthetic Route for the Preparation of 10-(Perfluorocyclohexyl)decane-1-thiol (FCyH10SH) and 11-(Perfluorocyclohexyl)undecane-1-thiol (FCyH11SH)	47
3.1 Preparation of 12,12-Difluoro-12-(perfluorophenyl)dodecane-1-thiol (FPHFH11SH)	68
5.1 Illustration of Reverse Patterning Lithography for Microstructuring GaAs Substrates	108
5.2 Illustration of Bidentate Fluorinated (5-(9,9,10,10,11,11,12,12,13,13,14,14,15,15,16,16,16-Heptadecafluorohexadecyloxy)-1,3-phenylene)dimethanethiol (PFPDT) for μ CP of GaAs Substrates	109

List of Figures

	<u>Page</u>
1.1 Figure 1.1. Six different types of crosslinked SAMs: (a) Aromatic thiol-based SAMs, (b) acetylenic-based alkanethiols, (c) other aliphatic alkanethiols, (d) silane-based alkanethiols, (e) boronic acid-based alkanethiols, and (f) crosslinked SAMs realized by hydrogen bonding.	2
1.2 Structures of the precursors used for crosslinked aromatic thiol-based SAMs.	3
1.3 E-beam induced crosslinking of (a) aliphatic SAMs; (b) aromatic SAMs; (c) nitro-terminated aromatic SAMs; (d) nitrile-terminated aromatic SAMs.	4
1.4 Schematic representation of the different steps involved in the crosslinking of aromatic SAMs: (a) irradiation, (b) emission of secondary electrons, (c) dissociation of C-H bonds, (d) self-quenching.	6
1.5 XPS data for pristine and crosslinked SAMs. XPS spectra for C 1s and S 2p regions of pristine (in yellow) and electron irradiated (50 eV, 60 mC/cm ²) monolayers (in blue) of (a) biphenyl-terminated SAM, (b) terphenyl thiol SAM.	8
1.6 Irradiation-induced crosslinked NBPT SAM. (a) Schematic representation of the EUV irradiation process, (b) XPS spectra for NBPT on gold before and after EUV irradiation.	11
1.7 Schematic representation of polymer brush fabrication.	13
1.8 Schematic representation of the transfer of CNMs onto other surfaces such as metal grids.	14
1.9 HIM images of CNMs converted from various pristine SAMs and then transferred onto TEM grids. The upper left insets show the pristine SAMs.	15
1.10 Conversion of BPT SAMs into graphene on copper substrates: (a) Schematic representation, (b) XPS spectra for the products in each step.	17
1.11 Schematic representation of the polymerization process of DATs on Au.	19
1.12 Mechanism for 1,4-photopolymerization of diacetylenes. (a) Array of diacetylene molecules. (b) An excited diradical monomer (red circles). (c) Coupling of the neighboring monomer (red arrows). (d) Diradical	20

	dimer. (e) Chain propagation reaction toward both sides until termination of reactive radicals (blue circles).	
1.13	(a) ATR-FTIR and (b) Raman spectra for C3-DATs and C3-poly-DATs on Au (111) surfaces.	21
1.14	Schematic representation of the polymerization of mercaptomethyl styrene on Au.	22
1.15	A schematic showing cross-linked gold nanoparticles with CBSH-X.	24
1.16	Schematic representation of the fabrication of single-layer polydiacetylene through coassembled PCDA and DT double layers.	25
1.17	The formation of a crosslinked SAM of CCHT via electron irradiation.	26
1.18	The SEM images Au surfaces patterned using SAMs as resists: a) cis-CCHT, b) trans-CCHT, and c) DDT.	27
1.19	Schematic representation of crosslinked MPTMS SAM formation on Au.	28
1.20	Surface-initiated polymerization of PMMA from crosslinked ATRP initiators on Au.	29
1.21	Temperature-dependent surface-initiated polymerization of MMA from various initiators; \diamond PMMA grown from a standard initiator; \blacklozenge PMMA grown from the crosslinked initiator; and \square PMMA grown from a silane initiator on SiO ₂ .	30
1.22	Schematic representation of a MPTMS coating on the surface of GaAs: (a) cleaned and etched GaAs sample, (b) primary layer formation, and (c) polymer formation.	32
1.23	Structures of 4 different crosslinked SAMs realized by hydrogen bonding.	33
1.24	Schematic representation of 4-carboxythiophenol SAM on Au at low pH, and ion adsorption ($M^+ = Cd(OH)^+$ or $Pb(OH)^+$) at high pH.	34
1.25	Schematic representation of a crosslinked boronic anhydride surface.	35
2.1	Molecular structures of the cyclohexyl-terminated thiols used in this study	40
2.2	XPS spectra of the (A) Au 4f, (B) S 2p, (C) C 1s, and (D) F 1s binding regions of the SAMs.	54

2.3	PM-IRRAS spectra showing the C–H stretching region of the H18SH , HCyHnSH , and FCyHnSH SAMs.	58
2.4	Deconvolution of the peaks in PM-IRRAS spectra of (A) HCyH10SH and (B) HCy11SH .	59
2.5	Comparison of the advancing contact angles of various probe liquids for: (A) the HCyHnSH SAMs and PE ; (B) the FCyHnSH SAMs and PTFE . W = water; F = formamide; MF = methylformamide; DMF = dimethylformamide; ACN = acetonitrile; SQ = squalane; HD = hexadecane. HD fully wets the HCyHnSH SAMs and PE .	62
3.1	Molecular structures of the adsorbates used to generate mixed SAMs on gold.	67
3.2	XPS spectra of the (a) S 2p, (b) C 1s, and (c) F 1s binding regions of the mixed SAMs derived from HCyH11SH and FCyH11SH .	75
3.3	XPS spectra of the (a) S 2p, (b) C 1s, and (c) F 1s binding regions of the mixed SAMs derived from PhH12SH and FPhFH11SH .	76
3.4	(a) CF ₂ / Au ratio and (b) F/Au ratio of the mixed SAMs derived from HCyH11SH and FCyH11SH .	79
3.5	(a) CF/Au ratio and (b) F/Au ratio of the mixed SAMs derived from PhH12SH and FPhFH11SH .	80
3.6	PM-IRRAS spectra of the mixed SAMs derived from (a) HCyH11SH / FCyH11SH and (b) PhH12SH / FPhFH11SH .	82
3.7	(a) Advancing contact angles of water and diiodomethane on the mixed SAMs derived from HCyH11SH and FCyH11SH , and (b) surface energies of the mixed SAMs derived from HCyH11SH and FCyH11SH .	84
3.8	(a) Advancing contact angles of water and diiodomethane on the mixed SAMs derived from FPhFH11SH and PhH12SH , and (b) surface energies of the mixed SAMs derived from FPhFH11SH and PhH12SH .	85
4.1	Molecular structures of the 6 adsorbates in this study.	90
4.2	(a) Advancing contact angles of water and hexadecane and (b) surface energies of bare GaAs and the investigated SAMs.	97
4.3	XPS spectra of the Ga 3d binding region after (a) 30 min and (b) 2 days of ambient exposure and As 3d after (c) 30 min and (d) 2 days of ambient exposure of the SAMs.	99

4.4	Ratio of oxide to bulk of As 3d integrated intensities after 2 days of ambient exposure.	101
4.5	XPS spectra of the S 2p after (a) 30 min and (b) 2 days of ambient exposure, C 1s after (c) 30 min and (d) 2 days of ambient exposure of the SAMs.	103
4.6	Ratio of the total C 1s integrated intensities divided by the number of C atoms (n) to all the As 3d integrated intensities after 30 min (black squares) and 2 days (red circles) of ambient exposure.	104
4.7	XPS spectra of the F 1s after (a) 30 min and (b) 2 days ambient exposure, O 1s after (c) 30 min and (d) 2 days ambient exposure of the SAMs.	105
5.1	XPS spectra of the (A) Ga 3d, (B) As 3d, (C) O 1s, (D) F 1s, (E) C 1s, and (F) S 2p binding regions of the bare GaAs and PF PDT -printed GaAs(100) surface. The GaAs surface was exposed to ambient conditions for 30 min. The red dashed lines represent deconvoluted peaks.	114
5.2	Cross-section profiles for mesa with a diameter = 250.0 μm atop GaAs with corresponding microscope images (A, D) before etching, (B, E) after etching, and (C, F) after etching and resin removal.	118
5.3	Microscope images of (A) mesas with a diameter of 100 μm and (B) microstructures on GaAs of different sizes and shapes.	119

Chapter 1: Crosslinked Self-Assembled Monolayers: Formation and Applications

1.1. Introduction

The discovery of the spontaneous adsorption of organic alkane disulfides to metal substrates, such as gold, in 1983 by Nuzzo and Allara as the first example of self-assembled monolayers (SAMs) and the subsequent use of alkanethiols has led to the wide spread use SAMs.¹⁻³ Over the past few decades, SAMs have been widely used as a robust surface modification method in various industrial fields, such as in microelectromechanical system (MEMS) devices,⁴ antifouling coatings for biomaterials,⁵ and microcontact printing.⁶⁻⁷ Compared to conventional polymer coatings, such as polytetrafluoroethylene (PTFE), SAMs applied onto a surface can be controlled to reach thicknesses in the nanometer range with high uniformity and hydrophobicity.⁸⁻⁹ For example, silane-based SAMs are routinely applied as nanocoatings in MEMS devices due to their ability to decrease adhesion and friction leading to enhanced performance.¹⁰⁻¹²

Compared to normal silane SAMs, which only bind to metal oxides and silicon, thiol-based adsorbates are more compatible toward the surfaces of metal, such as gold, silver, and copper, or III-V compounds, such as GaAs.¹³ As a well-known system, stability has been the major issue that has hindered thiol-based SAMs for further applications. Compared to N-heterocyclic carbenes (NHC)-based SAMs on gold or silane-based SAMs on silicon, which form strong covalent bonds between the adsorbates and substrates, the S-Au interaction is less stable in ambient conditions.¹⁴⁻¹⁵ Previous research has shown that normal alkanethiol SAMs organized by van der Waals (vdW) interaction are sensitive to temperature and desorb from gold surfaces at 70 °C.^{2,16} In addition, strong oxidizing reagents damage thin films and produce disulfides in a short period of time.

To broaden the application of SAMs, researchers have put in great effort to develop a more stable SAM system on gold that shows good resistance to high temperature and harsh chemical conditions. Intermolecular crosslinking is one of the effective methods to enhance the thermal and chemical stability of SAMs. It is noted that SAM molecules consists of three key parts: the headgroup binding to the corresponding substrate; the methylene spacer, which provides vdW interchain interaction; and the tailgroup.¹⁷ Theoretically intermolecular crosslinking can occur in all three parts of SAMs. However, unlike the natural formation of a polymerized network for the silane headgroup, the bonding nature of sulfur atoms of thiols determines that crosslinking at the headgroup for thiol-based SAMs is not achievable.¹⁸⁻¹⁹

This chapter focuses on the crosslinking process of corresponding adsorbates, and their applications in materials science. The crosslinked SAMs introduced in this chapter are divided into six categories: (1) aromatic thiol-based SAMs, (2) olefinic- and acetylenic-based alkanethiols, (3) other aliphatic alkanethiols, (4) silane-based alkanethiols, (5) boronic acid-based alkanethiols, and (6) crosslinked SAMs realized by hydrogen bonding (see Figure 1.1).

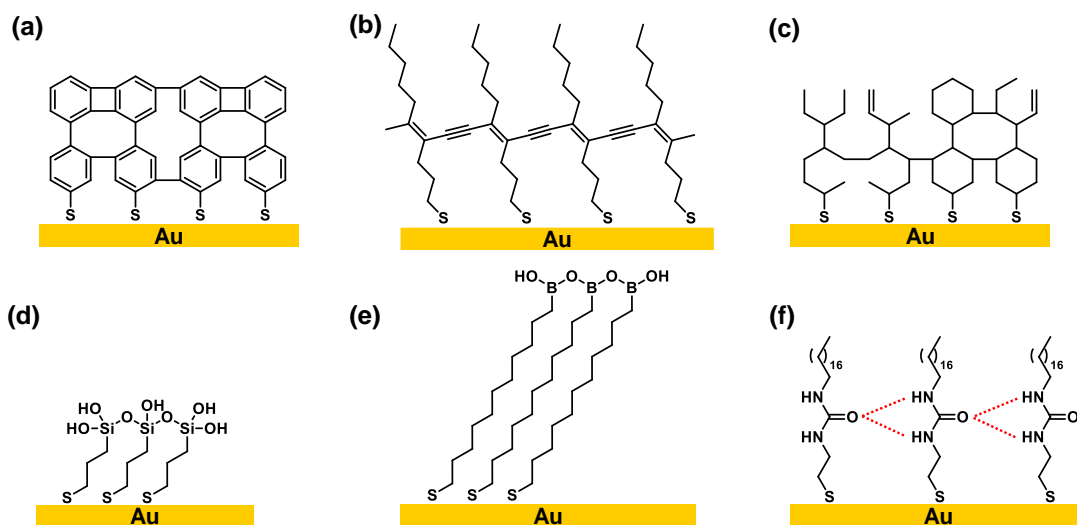


Figure 1.1. Six different types of crosslinked SAMs: (a) Aromatic thiol-based SAMs, (b) acetylenic-based alkanethiols, (c) other aliphatic alkanethiols, (d) silane-based alkanethiols, (e) boronic acid-based alkanethiols, and (f) crosslinked SAMs realized by hydrogen bonding

1.2. Aromatic Thiol-Based SAMs

In 1999, Geyer et al. discovered that biphenyl-4-thiol (BPT) can crosslink laterally upon low energy electron irradiation at 50 eV.²⁰ Additionally, Angelova et al. found that not only a BPT SAM, but various kinds of SAMs based on aromatic thiols or thiolates can also undergo similar intermolecular crosslinking, which turns the original system into a crosslinked aromatic SAM system (see Figure 1.2).²¹

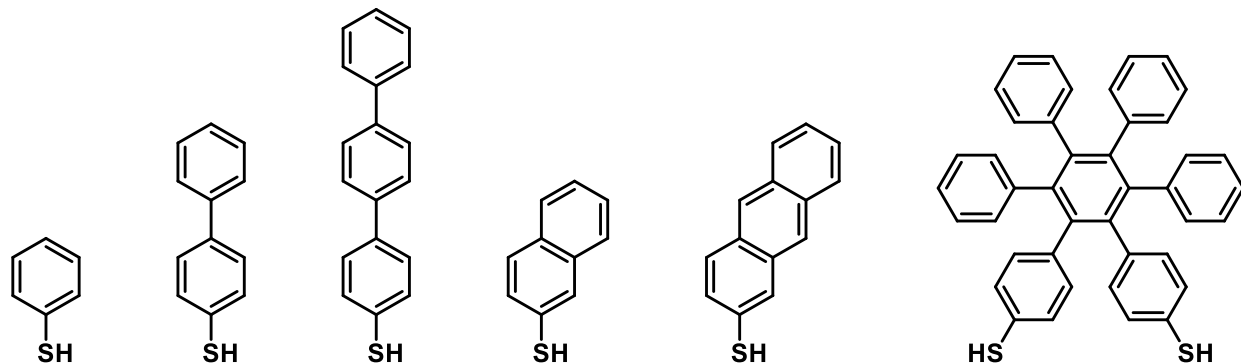


Figure 1.2. Structures of the precursors used for crosslinked aromatic thiol-based SAMs. Adapted from references 21, copyright 2013 American Chemical Society.

Figure 1.3 summarizes electron-induced crosslinking of aromatic thiol-based SAMs with three different tailgroups, compared to alkanethiol with alkyl chain. In contrast to BPT SAM forming a crosslinked 2D network under electron irradiation (Figure 1.3b), normal alkanethiol with alkyl chain partially desorb from gold surfaces and form double bonds randomly, as shown in Figure 1.3a.²² Figure 1.3c shows that compared to hydrocarbon aromatic SAMs, nitro-terminated aromatic SAMs not only show crosslink upon electron irradiation but also have their nitro groups reduced to amino groups.²³ In addition, Zharnikov and coworkers discovered that crosslinking of

biphenylthiol SAMs terminated with CH_2NO_2 reduce to SAMs terminated with CH_2NH_2 upon electron irradiation, as shown in Figure 1.3d.²⁴

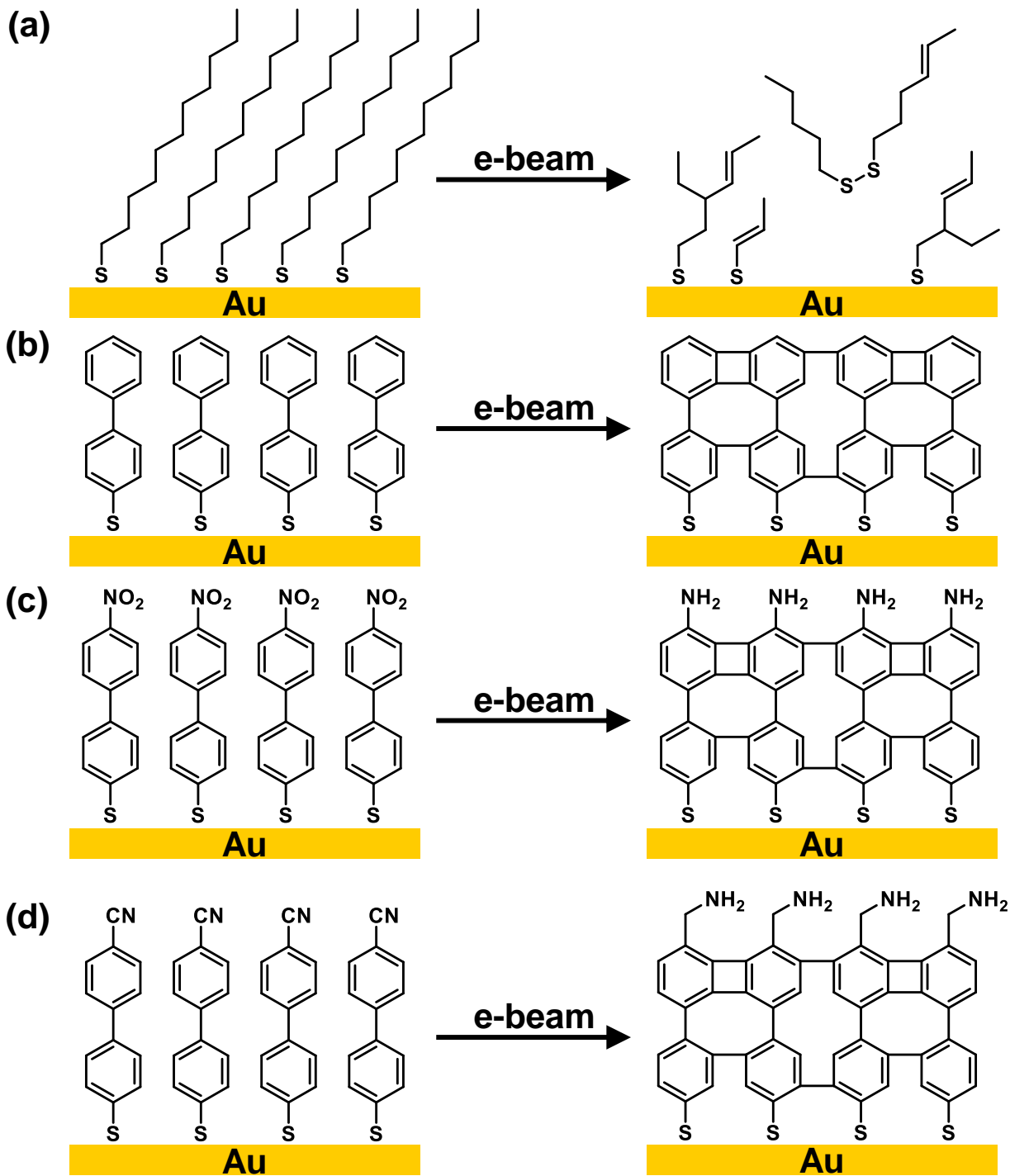
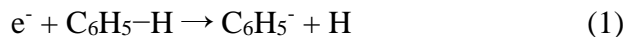


Figure 1.3. Electron induced crosslinking of (a) aliphatic SAMs; (b) aromatic SAMs; (c) nitro-terminated aromatic SAMs; (d) nitrile-terminated aromatic SAMs. Adapted from reference 25, copyright 2012 American Chemical Society.

1.2.1. Formation

Taking BPT SAM as an example, the formation for the crosslinking can be summarized as a dissociative electron attachment (DEA) process (see Figure 1.4).²⁶ First, under the impact of irradiation such as electrons and X-rays, a gold substrate emits secondary electrons, as shown in Figure 1.4a and 1.4b.²⁷ The dissociative primary and secondary electrons lead to C-H bond cleavage of phenyl rings with hydrogen atoms left behind, which yields transient negative ions (TNI), as shown in Figure 1.4c.²⁸ In this process, the electron affinity of the phenyl radical is 1.1 eV, which is higher than that of hydrogen (0.75 eV).²⁹ Thus, the dissociative electron attaches to the phenyl fragment ion instead of hydrogen. The DEA process for benzene is expressed in Equation 1.



The key factor for lateral crosslinked product is the stability of the aromatic backbones, leading to the formation of single and double bonds between the phenyl rings, followed by the release of hydrogen. At the end of the reaction, the lateral crosslinking is terminated by the self-quenching of electron tunneling to the gold surface (see Figure 1.4d).²⁶ In addition, researchers found that crosslinking of aromatic SAMs also occurs upon exposure to other sources of irradiation such as X-rays (10-100 eV),³⁰ helium ion beam (HIM, 35 keV),³¹ and extreme UV (EUV, 92.5 eV).³² These results further confirmed that primary electrons originating from the incoming electron beam are not necessary, and that, instead, secondary electrons emitted from the gold surface play a more important role in the crosslinking process.

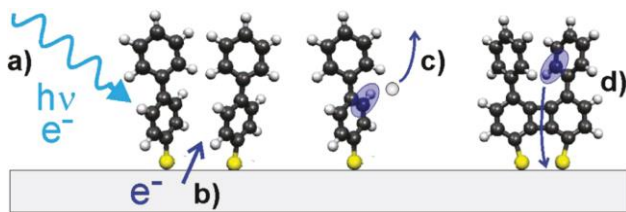


Figure 1.4. Schematic representation of the different steps involved in the crosslinking of aromatic SAMs: (a) irradiation, (b) emission of secondary electrons, (c) dissociation of C-H bonds, (d) self-quenching. Reprinted with permission from reference 26, copyright 2009 American Chemical Society.

In addition to irradiation energy, another key parameter for crosslinking aromatic SAMs is the electron dose, which is used to measure the quantity of charge per unit area upon irradiation. Interestingly, there is only a slight difference in crosslinking conditions (electron energy and dose) between extensive SAM precursors. To determine the optimal conditions for irradiation-induced crosslinking, scientists have used the cross section σ as a parameter when a rate reaches saturation behavior.³³ The cross section for the electron irradiation involves a balance between the crosslinking degree of the SAMs and the damage to the gold interface, which is determined as the primary electron energy of 50 eV.²⁸ Recently, Koch and coworkers investigated the crosslinking efficiency of halogenated biphenyl thiols.³⁴ The authors found that iodide-substituted biphenyl thiol showed more efficient electron-induced crosslinking than fluorine- or bromine-substituted species. Moreover, the electron dose determines the degree of crosslinking, and the crosslinking degree of the SAMs increases with the electron dose, reaching a maximum of ~90% at an electron dose of ~50 mC/cm² and above, as determined from X-ray photoelectron spectroscopy (XPS).³⁵ However, complete 100% crosslinked SAMs are not achievable because of the steric effect of the biphenyl structure.²⁶ Upon irradiation at higher doses, no further change to the resulting film itself is observed, but the gold interface is damaged and crosslinked films are desorbed from surfaces.³⁵

Compared to the pristine BPT SAM, infrared (IR) spectra for the crosslinked product show that two peaks due to the C-H stretching vibration of the pristine phenyl ring at 3046 cm^{-1} and 3038 cm^{-1} disappear after electron irradiation. Figure 1.5 shows the XPS spectra for the C 1s and S 2p regions of (a) biphenyl-terminated SAMs and (b) terphenyl thiol SAMs following electron irradiation (50 eV , 60 mC/cm^2).²¹ In the C 1s region, the integrated C 1s peak decreases in both of the SAMs investigated after crosslinking. The carbon content in the biphenyl-terminated SAM with hydrocarbon chains is decreased by 16%, and the calculated thickness is decreased from 12 \AA to 10 \AA , as determined from XPS. To explain these results, Schnack and coworkers performed a molecular dynamics simulation for crosslinking various biphenyl-terminated SAMs, which indicated that partial dissociation of the aromatic rings takes place to maximize the 2D molecular network.³⁶ In the XPS spectra obtained for S 2p, pristine SAMs exhibit a characteristic peak due to the bound thiols (red lines), which is a doublet and attributed to S $2p_{3/2}$ and S $2p_{1/2}$ at binding energies of 162.0 eV and 163.0 eV , respectively.³⁷ The new peak appearing at 163.5 eV for the crosslinked SAMs suggests the formation of unbound sulfur species or disulfides because of the cleavage of S-Au bonds after irradiation, as shown by the green line obtained by spectral deconvolution. The results obtained from low-energy electron diffraction (LEED) and a scanning tunneling microscope (STM) also indicate loss of long-range order in the crosslinked aromatic SAMs.

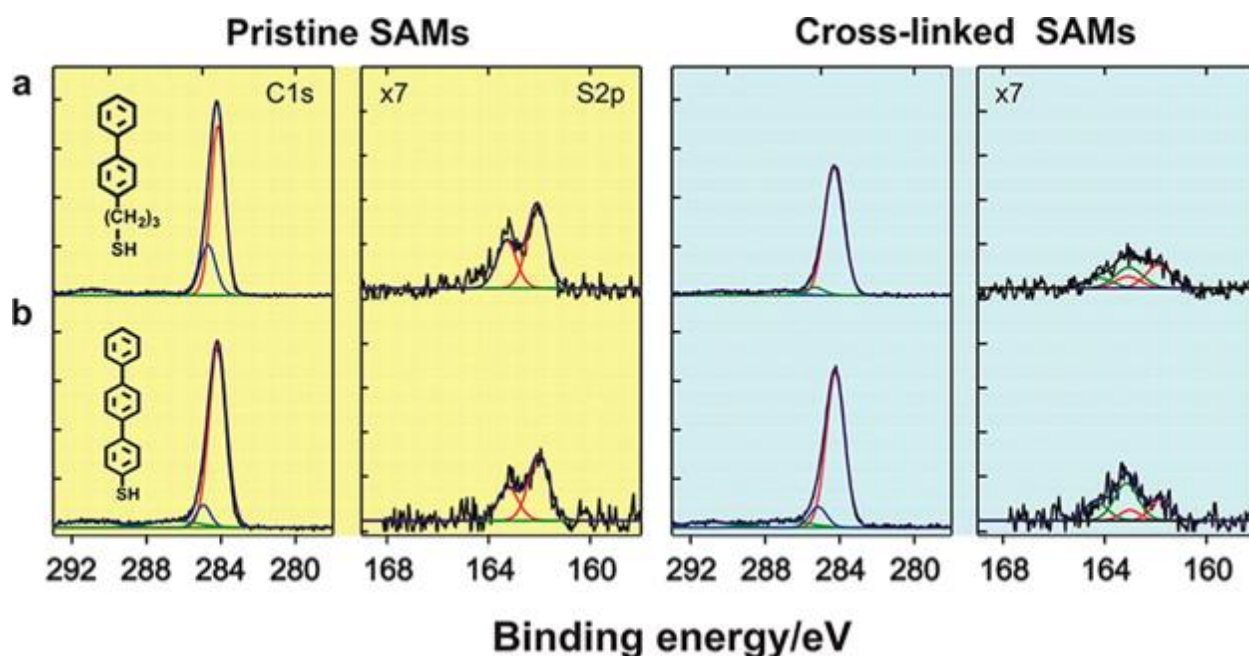


Figure 1.5. XPS data for pristine and crosslinked SAMs. XPS spectra for C 1s and S 2p regions of pristine (in yellow) and electron irradiated (50 eV, 60 mC/cm²) monolayers (in blue) of (a) biphenyl-terminated SAM, (b) terphenyl thiol SAM. Adapted from reference 21, copyright 2013 American Chemical Society.

1.2.2. Electron-Beam Lithography

In the modern semiconductor industry, lithography is one of the basic processes used for transferring a designed pattern onto semiconductor substrates, followed by an etching or metal deposition process to fabricate microelectronic devices.³⁸ Mainstream lithography techniques include photolithography, electron-beam (e-beam) lithography, and ion-beam lithography.³⁹ In the case of e-beam lithography, surface patterning is achieved by directly controlling an electron beam to write onto a resist-coated surface.⁴⁰ There are two types of e-beam resist in e-beam lithography: positive and negative. With a positive resist, the areas exposed to the e-beam are removed by a developer solution in the next step, to expose the bare substrate. In contrast, for a negative resist, only the areas of the resist exposed to the e-beam remain, while the other areas are removed.⁴¹ To fabricate a high resolution and high aspect ratio pattern on a surface, the negative

resist used in e-beam lithography needs to have high sensitivity to electrons, small molecular size, and low thickness.⁴²

When the crosslinked BPT SAM was first discovered by Geyer and coworkers in 1999, the authors noted that the crosslinked SAM showed good resistance to chemical etching solution.²⁰ Compared to a conventional polymeric resist such as PMMA, crosslinked aromatic SAMs have the potential to be used as negative resists in e-beam lithography. To test BPT SAMs for use as negative resists, Hinze and coworkers patterned BPT-coated gold substrates with an e-beam. Then, the patterned SAM-coated surface was placed into a 0.2 M KCN/1 M KOH solution for chemical etching, also called a wet etching process. After wet etching, the gold surface with crosslinked SAMs remained while the other pristine SAM areas were etched away, which showed clear patterns with a depth of 20 nm and small width of down to 10 nm.⁴³

Subsequently, Yildirim and coworkers investigated the lithography properties of crosslinked aromatic SAMs containing one, two, and three phenyl rings.³⁵ The BPT SAM exhibits the best performance as a negative resist, as the phenyl thiol fails to form a highly crosslinked network and the pristine terphenyl thiol SAMs are hard to remove by wet etching. Fluorinated SAMs (FSAMs) have been used for surface modification thanks to the excellent hydrophobic and low surface friction properties of fluorinated materials.⁴⁴ However, FSAMs are vulnerable to radiation damage by low-energy electrons.⁴⁵ To solve this issue, Terfort and coworkers investigated crosslinked perfluoroterphenyl-terminated SAMs exposed to low-energy electrons with a low dose (10 eV, 30 mC/cm²).⁴⁶ Note that the cleavage of C-F bonds observed upon irradiation follows the behavior of hydrocarbon aromatic SAMs. Additionally, the crosslinked FSAMs can be used as e-beam resists and hydrophobic coatings.

In summary, BPT SAM and its derivatives have been widely used in e-beam lithography.²⁵ Chemical etching, direct laser patterning,⁴⁷ thermodesorption,⁴⁸ and SAM exchange^{32,49} can be used to remove pristine SAMs on a surface to form a pattern. All the methods mentioned above utilize the high stability of crosslinked SAMs compared to pristine SAMs.

1.2.3. Surface Functionalization

Surface functionalization plays an important role in biotechnology applications. By modifying a surface with different chemical functional groups, researchers can immobilize and detect biomolecules efficiently.⁵⁰ In 2007, Turchanin and coworkers crosslinked 4'-Nitro-4-biphenylthiol (NBPT) by EUV through a stencil mask to fabricate a patterned amino-terminated SAM, as shown in Figure 1.6a.³² XPS spectra show that after irradiation, the peak in the N 1s region shifts from 405.5 eV to 399.2 eV and the peak intensity in the O 1s region decreases significantly, which represent the fully reduction of amino functional groups from nitro functional groups, as shown in Figure 1.6b.

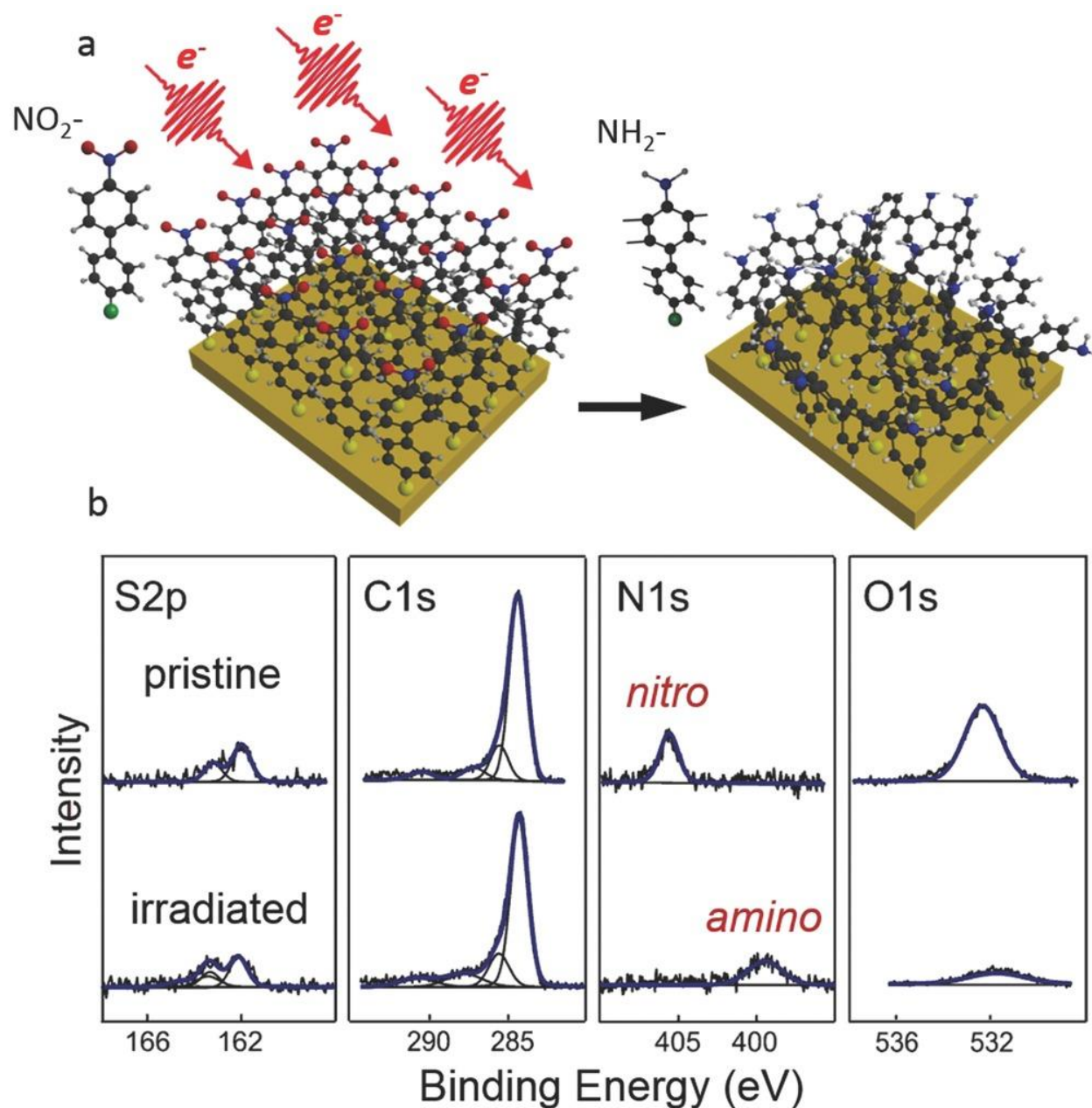


Figure 1.6. Irradiation-induced crosslinked NBPT SAM. (a) Schematic representation of the EUV irradiation process, (b) XPS spectra for NBPT on gold before and after EUV irradiation. Reprinted with permission from reference 51, copyright 2016 Wiley.

In a follow-up study, a NBPT SAM was used for the fabrication of a protein microarray for biodetection applications.⁵²⁻⁵³ The NBPT SAM on gold was crosslinked by e-beam irradiation through a stencil mask. The remainder of the pristine NBPT SAM was exchanged with protein-

resistant SAMs terminated with an ethylene glycol (OEG) segment.⁵⁴ Finally, a chelator was added to the surface, followed by drop casting of a protein solution. Thanks to the strong binding between amino groups and the target protein, only the electron-irradiated areas were covered with proteins that showed strong fluorescence.⁵² Nitrile-terminated aromatic SAMs, which also reduce to amino-terminated crosslinked SAMs upon irradiation, have been investigated by Zharnikov and coworkers.²⁴ Researchers found that compared to the NBPT SAM, cyanobiphenyl thiol (CBPT) forms less dense amino groups on the surface after irradiation, due to partial defragmentation of tailgroups. For the aforementioned crosslinked perfluoroterphenyl-terminated SAMs, researchers have adopted this system for metal deposition for electronic applications, which utilize crosslinked films to prevent intercalation of metal atoms.⁵⁵

1.2.4 Surface-Initiated Polymerization

Surface-initiated polymerization (SIP) shows promise for protective coating applications, such as antifouling and anticorrosion.⁵⁶ Recently, the NBPT SAM has attracted more and more attention in this application because of its precise control of polymer growth in selective areas with nanometer resolution.⁵⁷⁻⁵⁸ In this method, NBPT SAM was patterned by e-beam lithography, resulting in a stable crosslinked amino-terminated SAM, as shown in Figure 1.7a and Figure 1.7b. Next, the amino tailgroups were converted to diazo initiators in a diazotization process, as shown in Figure 1.7c. Finally, as shown in Figure 1.7d, the polymerization was started by adding styrene monomer and catalyst in solution. After photo polymerization, electron-irradiated SAM areas yielded polystyrene (PS) brushes with a minimum thickness of 10 nm.⁵⁸ In a follow-up study, by combining a crosslinked NBPT SAM and various monomers, researchers grew homogeneous polymer brushes with thicknesses ranging from 10-300 nm precisely, which respond to pH changes and can be used for building microsensors.⁵⁹

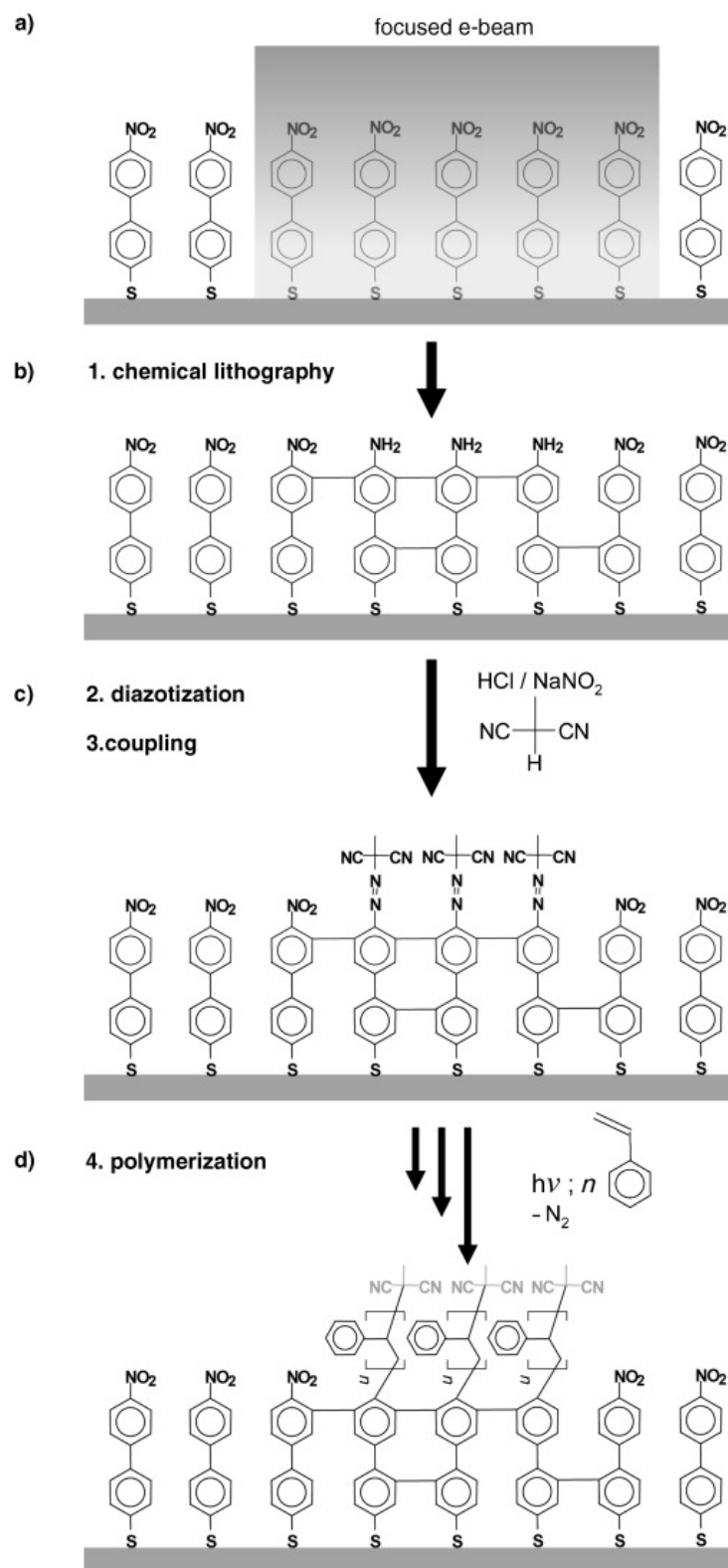


Figure 1.7. Schematic representation of polymer brush fabrication. Reprinted with permission from reference 58, copyright 2007 Wiley.

1.2.5 Carbon Nanomembranes (CNMs)

In 2005, Götzhäuser and coworkers fabricated the first carbon nanomembranes (CNMs) from crosslinked aromatic SAMs.⁶⁰ As shown in Figure 1.8b, after crosslinked aromatic SAMs were formed on a gold surface, a transfer medium, PMMA, was coated on top of the SAM. Then, the gold surface was etched as a sacrificial substrate to release the crosslinked films. Finally, CNMs were transferred onto other substrates, such as metal grids, Si, and graphene, followed by dissolution of the PMMA, as shown in Figure 1.8c and 1.8d.

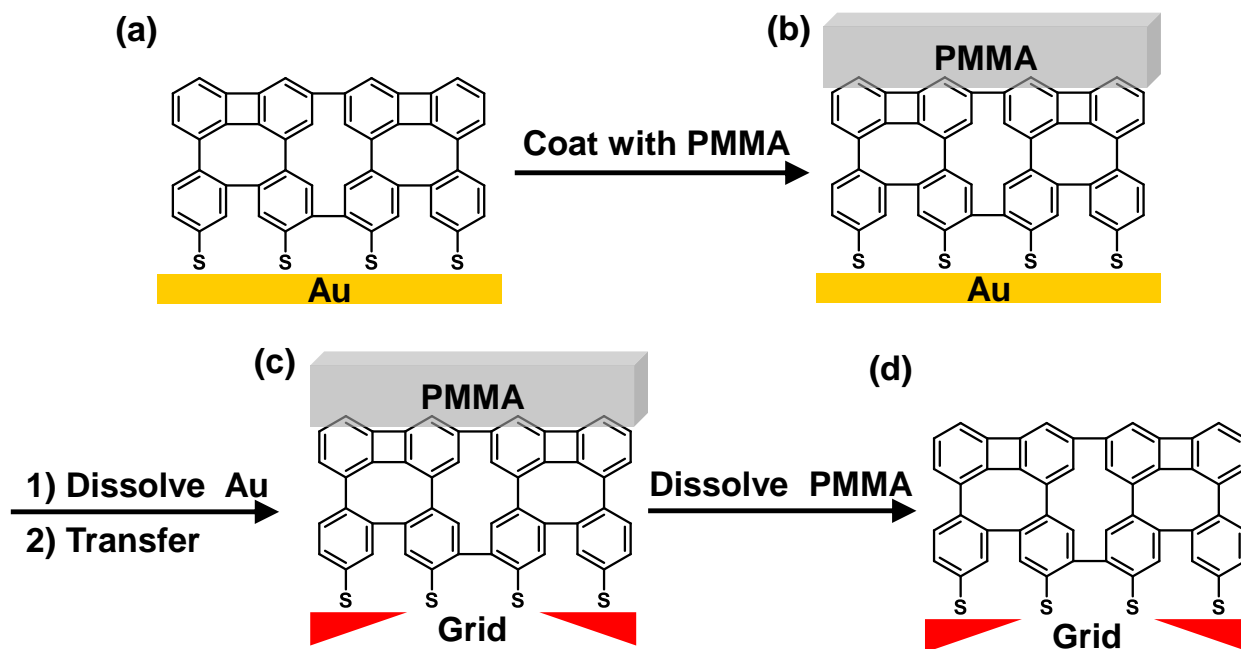


Figure 1.8. Schematic representation of the transfer of CNMs onto other surfaces such as metal grids. Adapted from reference 25, copyright 2012 Elsevier.

Since CNMs are converted from aromatic SAMs, their physical properties, such as thickness, rigidity, and porosity, can be tailored by using different SAM precursors.⁶¹ Figure 1.9 shows helium-ion microscopy (HIM) images of CNMs obtained from six different SAMs after being transferred onto TEM grids. From Figure 1.9a to 1.9c, the thickness of the pristine SAMs

increases from 0.6 nm to 2.4 nm, resulting in the final thickness of the CNMs to increase accordingly. Moreover, while the use of BPT SAM leads to hole-free CNMs, bulkier molecules form less-ordered SAMs and create more porous CNMs (Figure 1.9e and 1.9f) due to lower packing densities and intermolecular stacking.²¹ Additionally, it is simple to pattern CNMs with uniform nanoholes as nanosieves using e-beam lithography.⁶²

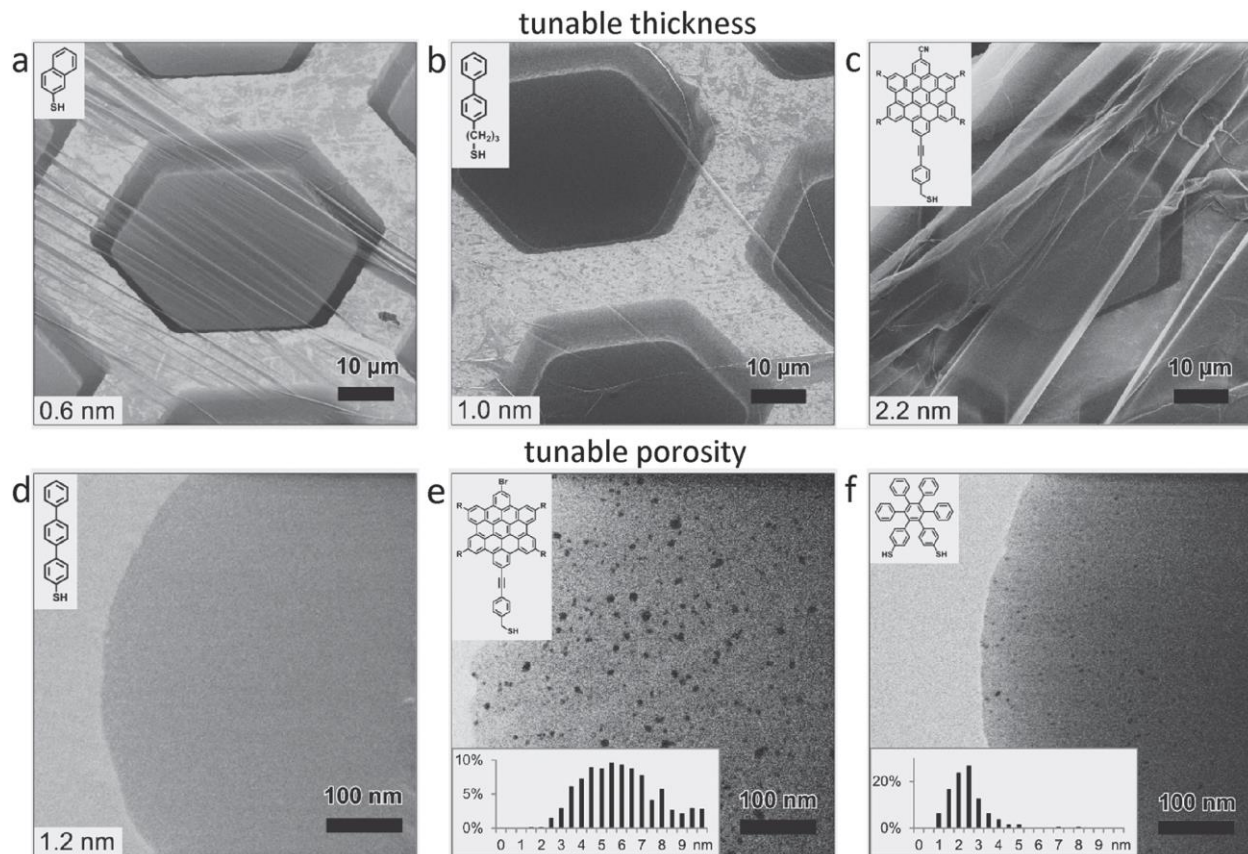


Figure 1.9. HIM images of CNMs converted from various pristine SAMs and then transferred onto TEM grids. The upper left insets show the pristine SAMs. Adapted from reference 21, copyright 2013 American Chemical Society.

Furthermore, CNMs are easily chemically functionalized by using SAM precursors with different functional groups, as used for coupling biomolecules and polymers.²⁵ After amino-terminated CNMs are released from gold, the thiol group on the opposite site of the CNM can couple with Au nanoparticles or other functional groups such as maleimide to form a Janus

nanomembrane.⁶³⁻⁶⁴ After years of rapid development, CNMs prepared from crosslinked aromatic SAMs have various applications in many fields such as graphene manufacturing,⁶⁵ nanofiltration,⁶⁶ and microdetectors.⁶⁷⁻⁶⁸

In 2013, Turchanin and coworkers grew single-layer graphene on Cu by annealing CNMs at above 800 °C for 2 h, as shown in Figure 1.10a.⁶⁹ The authors continued this research and fabricated patterned graphene from CNMs by using e-beam lithography.⁷⁰ From XPS spectra shown in Figure 1.10b, a doublet was observed at a binding energy of 161.2 eV (blue line), which was attributed to copper sulfides, and a doublet due to bound thiolate (red line) was found to completely disappear after annealing. Interestingly, the S 2p signal in the XPS spectra completely disappeared after transferring graphene to a Si-wafer, which indicated S-C bond cleavage and that sulfur atoms were left on the Cu substrate. After annealing BPT CNM into graphene, the Young's modulus was found to increase from 10 GPa to 48 GPa, indicating a significant increase in the mechanical strength.⁷¹

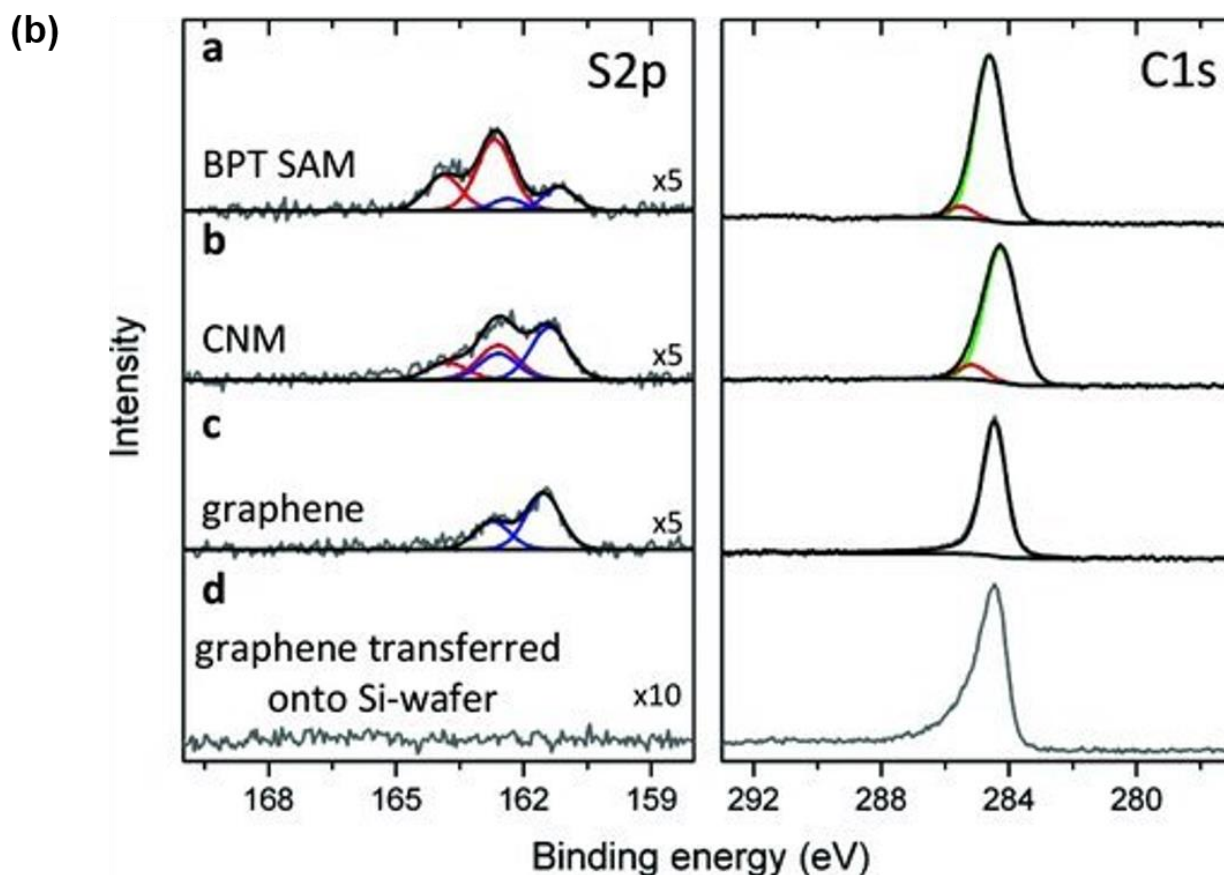
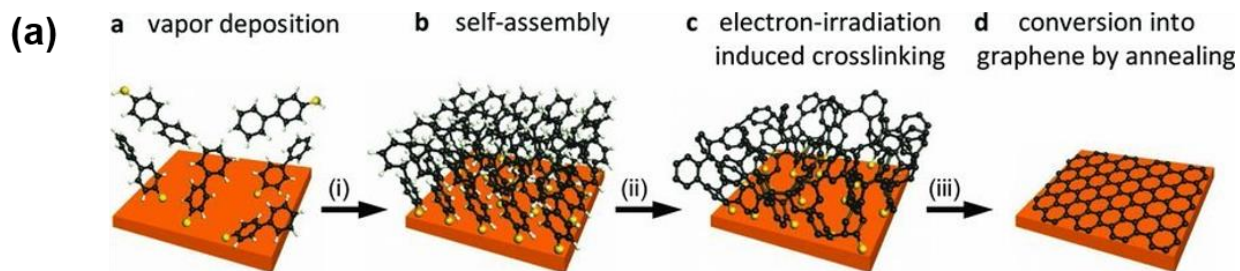


Figure 1.10. Conversion of BPT SAMs into graphene on copper substrates: (a) Schematic representation, (b) XPS spectra for the products in each step. Adapted from reference 69, copyright 2013 Wiley.

For separation, thin membranes, which combine high permeability and high selectivity, are desirable in the water treatment industry.⁷² CNMs and graphene can be fabricated into layers as thin as 1 nm, with a nanoporous structure and excellent mechanical strength, which make them excellent candidates for nanofiltration.⁷³⁻⁷⁴ Furthermore, researchers have used amino-terminated

CNMs to stack graphene to fabricate CNM/graphene field-effect transistors (FETs), as an alternative for graphene functionalization for biosensors and gas sensors.⁶⁷⁻⁶⁸

1.3. Olefinic- and Acetylenic-Based Alkanethiols

Beside crosslinked aromatic thiol-based SAMs, crosslinked SAMs from olefinic- and acetylenic-based alkanethiols have been well studied by scientists. Additionally, polydiacetylene materials are a type of conducting polymer with special optical properties that have extensive applications in photonics, nanoelectronics, and biosensors.⁷⁵ When polydiacetylene materials couple with chemical and biological stimuli, their characteristic absorption peak shows a redshift. Therefore, they have a sensitive chromic response to microorganisms, virus, and proteins, which is attractive for biosensing applications.⁷⁶

1.3.1 Formation

Crosslinked SAMs containing polydiacetylene were first reported by Batchelder et al. in 1994.⁷⁷ The authors deposited polymeric monolayers from diacetylene-containing disulfide onto Au (111) surfaces, as shown in Figure 1.11. Similar to diacetylenes in the solid-state, the chain polymerization of diacetylene thiolates (DATs) on surfaces follows some spatial conditions: the distance of the adjacent thiolates is 4.7-5.2 Å, and the distance between the C1 carbon of one diacetylene group to the C4 carbon of the adjacent diacetylene group (black arrow in Figure 1.11) is 3.4-4.0 Å.⁷⁸⁻⁷⁹ In contrast, diacetylenes undergo both 1,2- and 1,4-polymerization in solution.

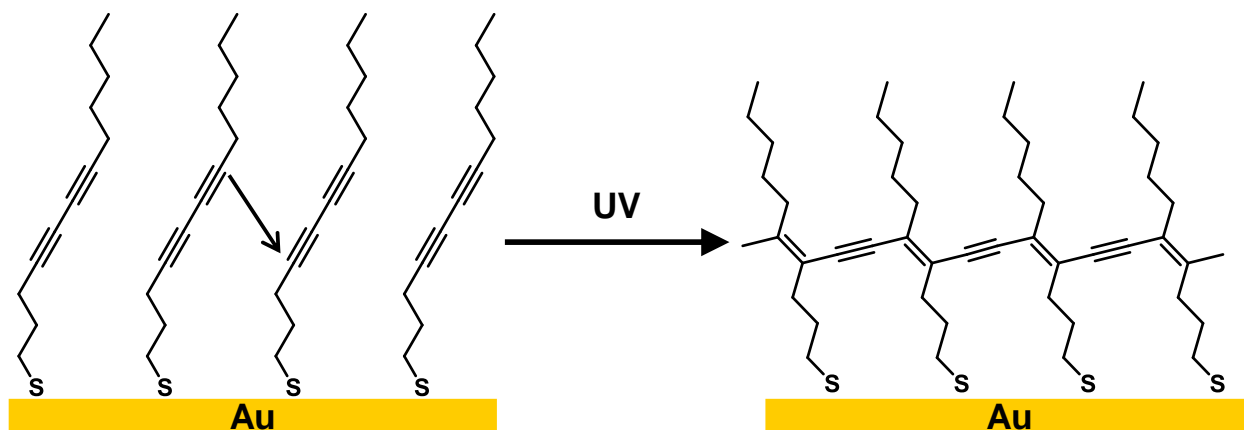


Figure 1.11. Schematic representation of the polymerization process of DATs on Au. Adapted from reference 78, copyright 1999 American Chemical Society.

The mechanism for 1,4-photopolymerization of diacetylenes is illustrated in Figure 1.12.⁷⁹ First, the initiation is started by UV irradiation of DAT monomers, which generates a diradical monomer, as shown in Figure 1.12b. After that, addition reaction occurs at both ends of the diradical monomer, as shown in Figure 1.12c. Finally, chain propagation at both sides is followed by termination of reactive radicals, as suggested by the blue circles in Figure 1.12e. The polydiacetylene backbone contains alternating double and triple bonds, which are represented in a resonance structure of three cumulative double bonds, as shown in Figure 1.12e.

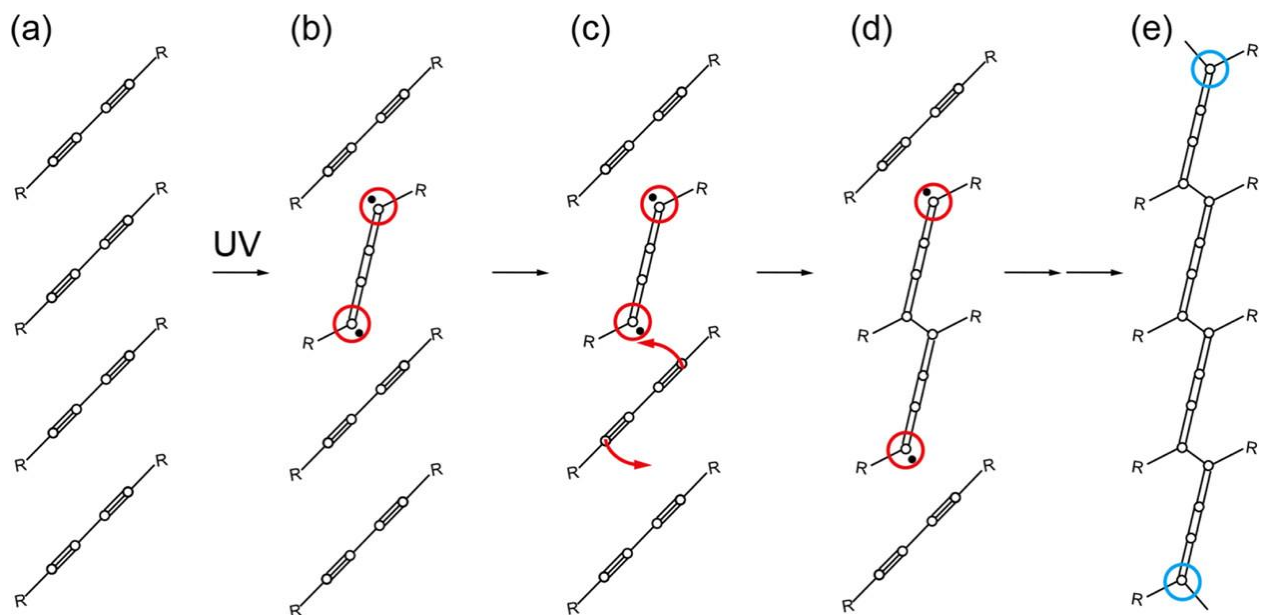


Figure 1.12. Mechanism for 1,4-photopolymerization of diacetylenes. (a) Array of diacetylene molecules. (b) An excited diradical monomer (red circles). (c) Coupling of the neighboring monomer (red arrows). (d) Diradical dimer. (e) Chain propagation reaction toward both sides until termination of reactive radicals (blue circles). Reprinted with permission from reference 79, copyright 2019 American Chemical Society.

In a following study, Cai et al. investigated the influence of ultraviolet (UV) exposure time on the crosslinked product.⁷⁸ They used resonance Raman spectroscopy to monitor the polydiacetylene backbone in crosslinked SAMs as a function of UV exposure time, which showed that the effective conjugation length in crosslinked DAT SAMs reached a maximum at 7 min before decreasing. This might be due to the increase in the hybridization strain in the polydiacetylene backbone as well as in the methylene chains with prolonged UV exposure. Bateas and coworkers studied the properties of crosslinked dodeca-4,6-diyne-1-thiol (C3-DATs).⁸⁰ Figure 1.13a shows the ATR-FTIR spectra obtained for C3-DATs and C3-poly-DATs on Au (111) surfaces. In both spectra for C3-DATs and C3-poly-DATs, the peaks at $\sim 2923\text{ cm}^{-1}$ and $\sim 2854\text{ cm}^{-1}$ are attributed to a methylene asymmetric and symmetric stretching band, respectively. After polymerization, a decrease in both peak intensities is observed, without the peak position shifting,

which is due to the decrease in the tilt angle of the alkyl chains. As shown in Figure 1.13b, two new peaks at $\sim 1875\text{ cm}^{-1}$ and $\sim 2450\text{ cm}^{-1}$ for C3-poly-DATs are observed in the Raman spectra. These two peaks can be attributed to the new double and triple bonds formed in the product films, which further confirms the polymerization of the DAT SAMs.

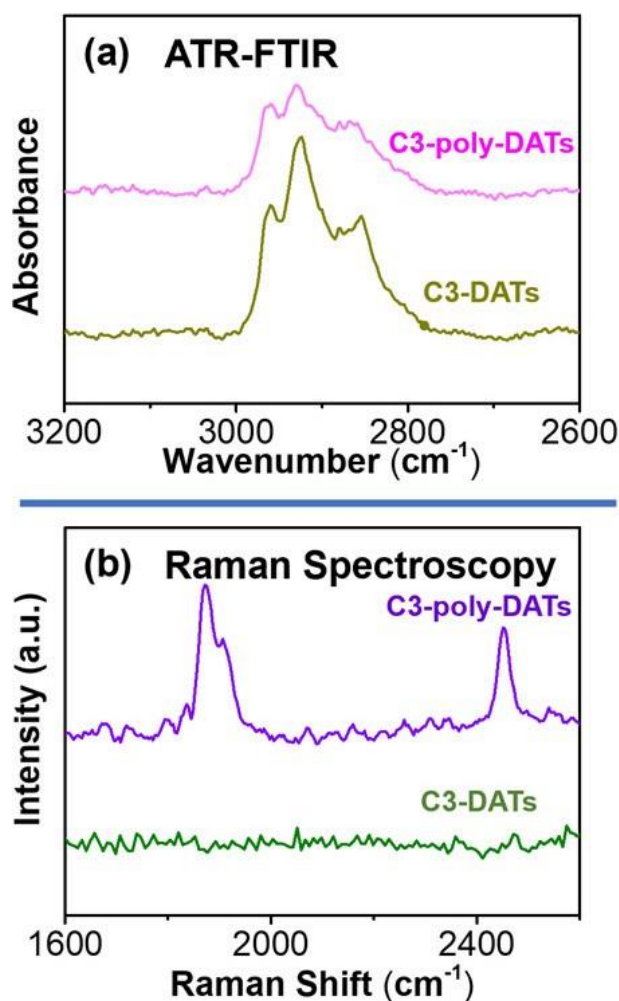


Figure 1.13. (a) ATR-FTIR and (b) Raman spectra for C3-DATs and C3-poly-DATs on Au (111) surfaces. Adapted from reference 80, copyright 2020 American Chemical Society.

In separated study, Menzel et al. studied the effect of the diacetylene functional group position on crosslinked DAT SAMs.⁸¹ They discovered that moving the diacetylene moiety closer to the thiol headgroup increases the hybridization strain in the alkyl chain, which reduces the

conversion of polymerization. In addition, with carboxylic acid-terminated DATs on Au (111), researchers were able to convert carboxylic acid into acid chloride, followed by coupling with other DATs to fabricate double and multilayer polydiacetylene coatings.⁸² By using this method, scientists utilized carboxylic acid-terminated DATs as scaffolds to build polydiacetylene thin films layer-by-layer, up to a thickness of 6 layers. The authors subsequently synthesized DAT SAMs on Au (111) with terminal methyl, hydroxyl, and carboxyl acid functional groups.⁸³ Compared to normal alkanethiol SAMs or pristine DAT SAMs on Au surfaces, all crosslinked DAT SAMs showed excellent stability toward repeated electrochemical cycling, high temperatures of up to 200 °C, and exposure to hot base solutions.⁸³

Another type of crosslinked SAM derived from olefinic-based alkanethiols is mercaptomethyl styrene (MMS), which was discovered by Schlenoff and coworkers in 1996, shown in Figure 1.14.⁸⁴ In this case, polymerization of the adsorbates was initiated by immersing the substrate in an azo initiator solution at 58 °C or by irradiating with a green laser. Time-resolved SERS spectra showed a peak at 1625 cm⁻¹ that disappears after crosslinking, which was attributed to the double bonds of the pristine SAM.

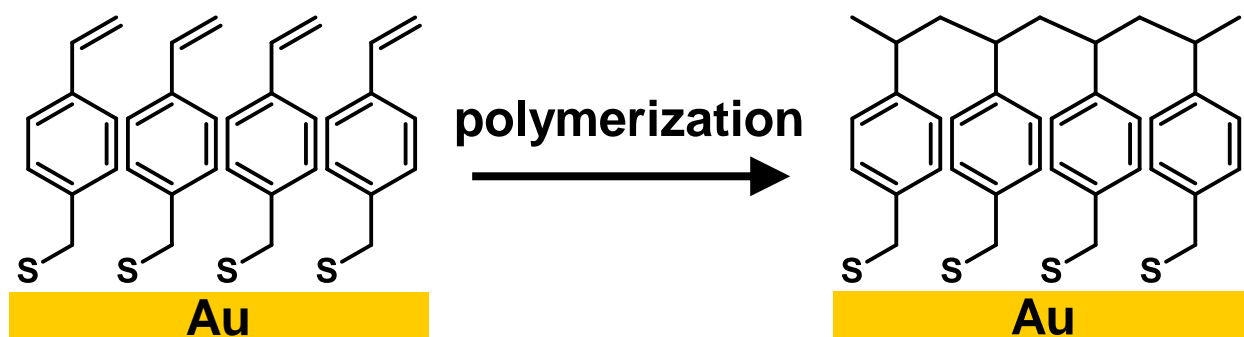


Figure 1.14. Schematic representation of the polymerization of mercaptomethyl styrene on Au. Adapted from reference 84, copyright 1996 American Chemical Society.

1.3.2 Photolithography

Although polydiacetylene materials have shown excellent properties in biosensors, crosslinked DAT SAMs have not been used in particular sensing applications because of their small thickness.⁷⁶ Crosslinked DAT SAMs provide an ideal model to study the structure of diacetylenes on surfaces. Additionally, they have many applications in photolithography, SAM-coated nanoparticles, and single-layer polydiacetylene fabrication. Photolithography is one of the most widely used techniques in semiconductor fabrication, which transfers patterns by exposing photoresist-coated surfaces to UV through a photomask.³⁸ In 1995, Crooks and coworkers applied UV irradiation to a DAT SAM-coated Au (111) to fabricate patterned polydiacetylene thin films.⁸⁵ The uncrosslinked portion of the DAT SAM was stripped using electrochemical desorption, followed by KCN/KOH solution etching. STM depth profiles indicated that a clear negative pattern was formed on the Au (111), which was approximately 7-8 nm in depth. These results validated the use of DAT SAMs as ultra-thin photoresists, which crosslink under UV and protect the underneath surfaces.

1.3.3 SAM-Coated Nanoparticles

In addition to application as a negative resist in photolithography, crosslinked DAT SAMs are valuable in SAM-coated nanoparticles in biomedical applications. In 2014, Jiang and coworkers coated gold nanoparticles with SAMs containing diacetylene to test their stability in different complex media, as shown in Figure 1.15.⁸⁶ The carboxybetaine functional group is one of the zwitterions that are used for antifouling coatings.⁸⁷ The authors designed and synthesized carboxybetaine-terminated alkanethiol with photocrosslinkable diacetylene in the alkyl chain spacer, and then crosslinked it on gold nanoparticles using UV irradiation to enhance the antifouling property. The crosslinked SAM-coated gold nanoparticles showed high resistance to

protein fouling from blood serum and decreased cell uptake. Additionally, they were stable at low/high pH and a high temperature of 80 °C.

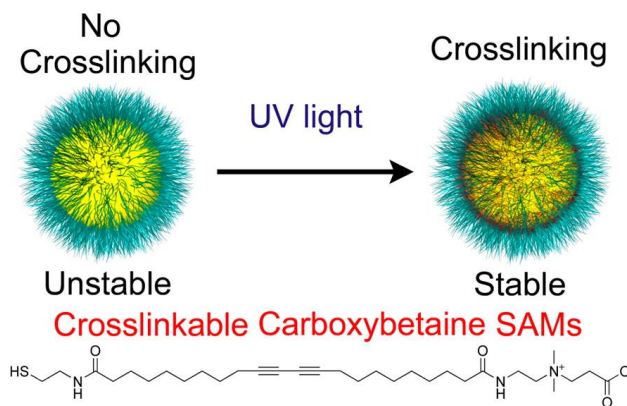


Figure 1.15. A schematic showing cross-linked gold nanoparticles with CBSH-X. Reprinted with permission from reference 86, copyright 2014 American Chemical Society.

1.3.4 Single-Layer Polydiacetylene Fabrication

Recently, Yu et al. invented a new strategy to fabricate single-layer polydiacetylene thin films using a SAM-coated gold electrode as a template, shown in Figure 1.16.⁸⁸ The authors deposited a functionalized gold electrode with dodecanethiol (DT), followed by the assembly of pentacos-10,12-diyneic acid (PCDA) via an electrode potential, which formed a well-ordered second monolayer on the DT. After photo-polymerization by UV, the polymerized monolayer of polydiacetylene was desorbed by application of an opposite electrode potential, which worked repeatedly to produce 2D polydiacetylene thin films.

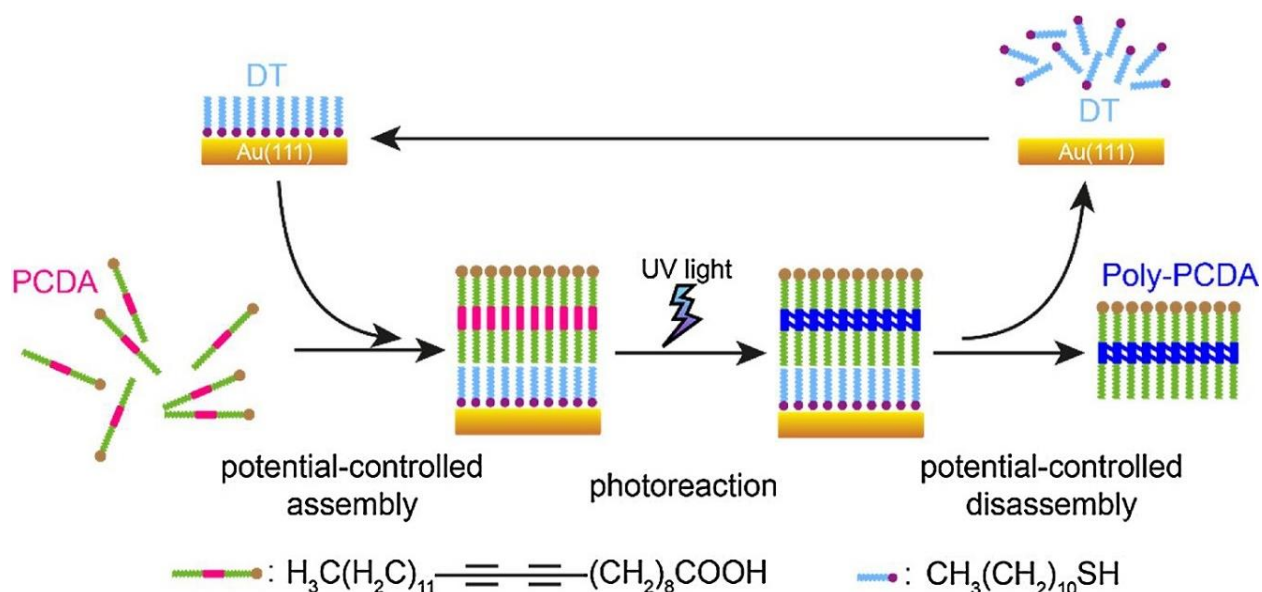


Figure 1.16. Schematic representation of the fabrication of single-layer polydiacetylene through coassembled PCDA and DT double layers. Reprinted with permission from reference 88, copyright 2017 Elsevier.

1.4. Other Aliphatic alkanethiols

In contrast to the crosslinking of aromatic thiol-based SAMs, aliphatic thiol-based SAMs undergo decomposition and disordering upon electron irradiation.⁸⁹⁻⁹² Interestingly, in the case of 4-cyclohexylcyclohexanethiols (CCHT), a cyclic aliphatic thiol-based SAM on Au (111), the irradiation-induced crosslinking process was found to be dominant over defragmentation and desorption.⁹³

1.4.1 Formation

Until now, the only study of irradiation-induced crosslinking of cyclic aliphatic thiol-based SAMs was reported by Zharnikov and coworkers in 2012.⁹³ The authors found that both SAMs generated from *trans*- and *cis*-conformations of 4-cyclohexylcyclohexanethiols (CCHT) crosslinked upon exposure to ionizing radiation, as shown in Figure 1.17. This contrasts with the

linear aliphatic thiol-based SAMs, which were severely damaged when exposed to quite low irradiation doses (5-8 mC/cm²).

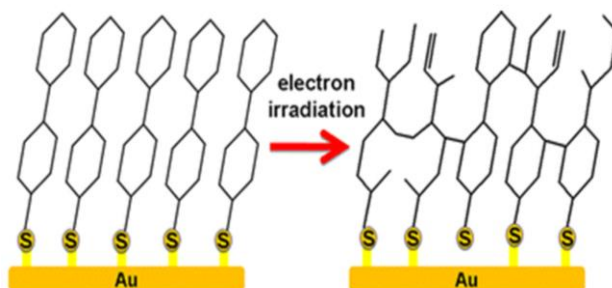


Figure 1.17. The formation of a crosslinked SAM of CCHT via electron irradiation. Reprinted with permission from reference 93, copyright 2012 American Chemical Society.

Under electron irradiation conditions, the C-H bonds are cleaved to generate radical moieties, which are relatively stable because of the nature of the cyclic skeletons of CCHT before crosslinking to other absorbates to form a 2D molecular network. Compared to the linear aliphatic thiol SAMs, the presence of cyclic rings is the key for the dominance of crosslinking over fragmentation and desorption processes. For cases where the C-C bonds belonging to the cyclic rings are cleaved, both fragments are still attached to the molecule matrix, which, then, subsequently form cross-linked bonds with neighboring molecules. Hence, the desorption of fragments is suppressed. The newly formed 2D network by crosslinking also hinders the cleavage of the headgroup-substrate S-Au bonds.

1.4.2 Electron-Beam Lithography

Similar to aromatic SAMs, crosslinked CCHT SAMs have been used as negative resists in e-beam lithography.⁹³ Figure 1.18 shows the SEM images of gold surfaces patterned using SAMs as resists: a) *cis*-CCHT, b) *trans*-CCHT, and c) dodecanethiol (DDT). While the crosslinked SAMs composed of *cis*- and *trans*-CCHT were found to protect the irradiated areas and the nonirradiated

areas were efficiently etched, the irradiation-induced damage to the DDT-based SAMs allowed preferred etching of the irradiated areas.

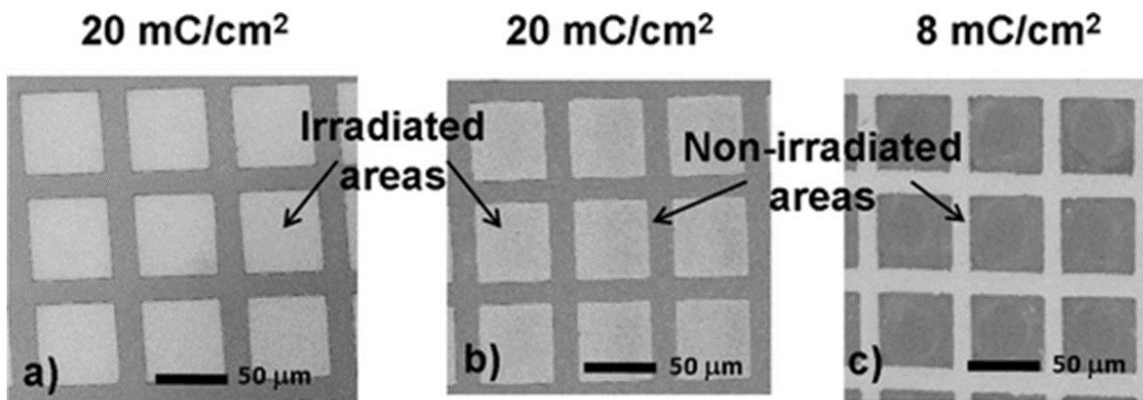


Figure 1.18. The SEM images Au surfaces patterned using SAMs as resists: a) *cis*-CCHT, b) *trans*-CCHT, and c) DDT. Reprinted with permission from reference 93, copyright 2012 American Chemical Society.

1.5. Silane-Based Alkanethiols

Another important type of crosslinked SAMs are silane-based alkanethiols, which can be used in surface-initiated polymerization (SIP),⁹⁴ surface passivation,⁹⁵⁻⁹⁶ and anti-corrosion coating.⁹⁷⁻⁹⁸ The crosslinked silane network forms a dense film to prevent oxygen or moisture diffusing into interfaces, which provides for long-term surface passivation. Additionally, the high thermostability of the crosslinked SAMs helps one to grow polymer brushes at high temperature in applications involving SIP.⁹⁴

1.5.1 Formation

As a pristine molecule for crosslinked silane-based alkanethiols, (3-mercaptopropyl) trimethoxysilane (MPTMS) has been well studied and widely adopted in the aforementioned applications. Taking MPTMS SAM as an example, as shown in Figure 1.19, the formation of a crosslinked MPTMS SAM can be concluded in 3 steps: (1) MPTMS molecules are

deposited onto a gold surface in anhydrous conditions to avoid self-polymerization; (2) hydrolysis of the silane converts the methoxy group (-OCH₃) connected to Si to hydroxyl groups (-OH) in the presence of water; (3) at the same time, intermolecular condensation leads to the Si-O-Si structure forming a crosslinked polysiloxane network.⁹⁹⁻¹⁰⁰ It should be noted that the trimethoxy silane group is less reactive to water than the trichlorosilane group, making it easier to control the polymerization of the silane on a surface.¹⁵ In this stage, with silanol groups present on the surface, one can generate thick self-polymeric films,⁹⁵ or enable grafting onto other silanes with specific functional groups.⁹⁴

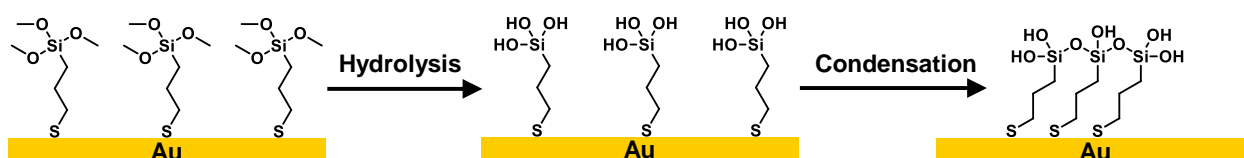


Figure 1.19. Schematic representation of crosslinked MPTMS SAM formation on Au. Adapted from reference 99, copyright 2016 American Chemical Society.

1.5.2 Surface-Initiated Polymerization

In 1994, Aramaki and coworkers coated hydroxyl-terminated alkanethiols onto a copper surface, followed by deposition of alkyltrichlorosilane.¹⁰¹ The hydroxyl groups coupled with alkyl trichlorosilane resulted in a film with a crosslinked polysiloxane network. In 2011, Baker and coworkers used silane-based alkanethiols to fabricate crosslinked ATRP initiators to grow polymer brushes on gold, as shown in Figure 1.20.⁹⁴ After the crosslinked MPTMS SAM was formed on Au to provide a hydroxylated surface, another silane terminated with initiator was grafted onto the MPTMS SAM, which formed a second layer of crosslinked interchain polysiloxane. After adding methyl methacrylate (MMA) monomer and catalyst, the system was heated up from 50 °C to 100 °C to initiate polymerization of PMMA from Au surfaces.

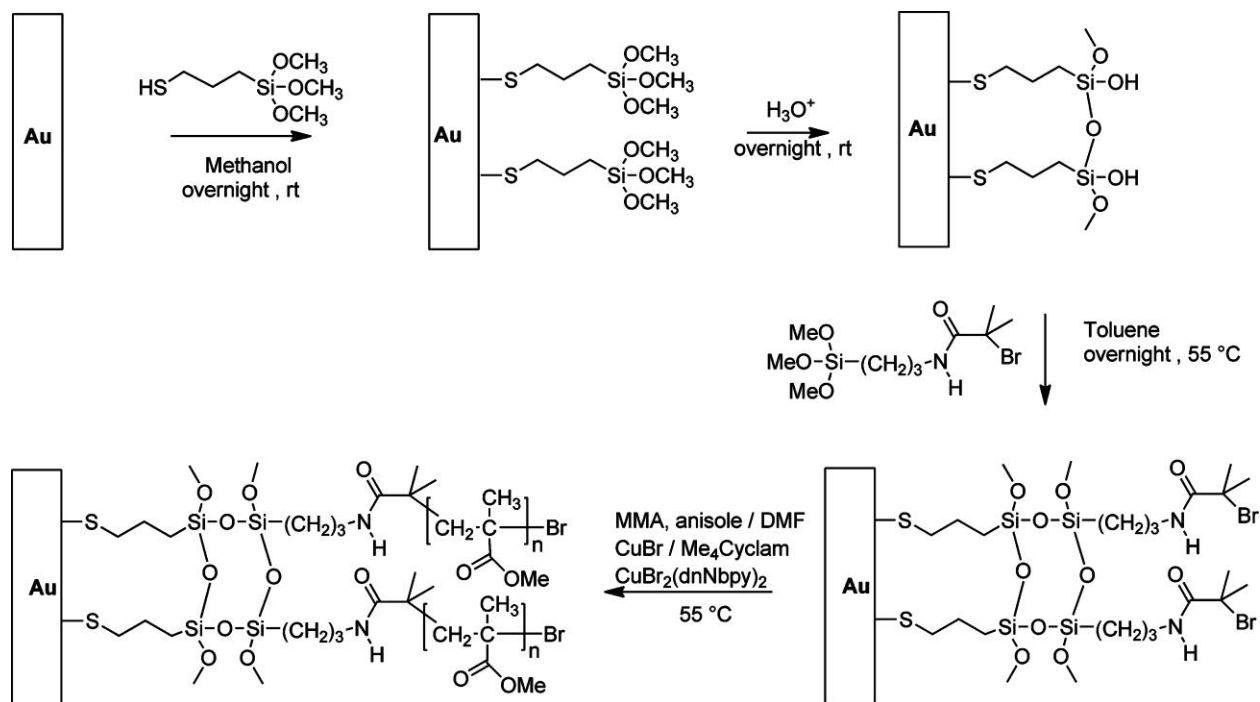


Figure 1.20. Surface-initiated polymerization of PMMA from crosslinked ATRP initiators on Au. Reprinted with permission from reference 94, copyright 2011 American Chemical Society.

The authors found that normal alkanethiols with ATRP initiator on gold led to the growth of thinner polymers compared to silane SAMs with ATRP initiator on a SiO_2 substrate, due to the poor thermostability of uncrosslinked initiators. In contrast to a crosslinked polysiloxane primer layer, polymer brushes grown from ATRP initiators on Au reached the same thickness as on a SiO_2 substrate, as shown in Figure 1.21. Thanks to the highly stable Si-O bond of crosslinked silane-based SAMs, the novel ATRP initiator allowed SIP at higher temperatures of up to $100\text{ }^\circ\text{C}$, which provides polymer growth from less reactive monomers such as styrene and vinyl pyridine.

Compared to the aromatic thiol-based SAMs discussed in Section 1.2.3, homogeneous SIP from crosslinked silane-based alkanethiols is cost-efficient because it does not need an expensive e-beam lithography system for the crosslinking process. However, it is difficult to pattern silane-

based SAMs since it has been reported that silanes are not compatible with microcontact printing techniques.¹⁵

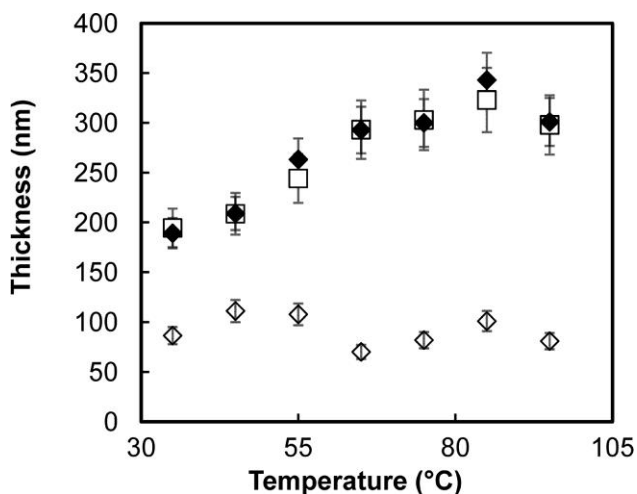


Figure 1.21. Temperature-dependent surface-initiated polymerization of MMA from various initiators; \diamond PMMA grown from a standard initiator; \blacklozenge PMMA grown from the crosslinked initiator; and \square PMMA grown from a silane initiator on SiO_2 . Reprinted with permission from reference 94, copyright 2011 American Chemical Society.

1.5.3 Surface Passivation

GaAs is a promising III-V semiconductor material that is widely used in devices such as photovoltaics (PV), light-emitting diodes (LED), photonics and radio frequency (RF) transistors, thanks to its high electron mobility and direct bandgap.¹⁰²⁻¹⁰³ To date, GaAs solar cells have shown record-breaking conversion efficiencies, ~29% for single-junction cells.¹⁰⁴ However, GaAs can become oxidized in the ambient environment and the oxide layer formed on GaAs can significantly decrease the solar cell efficiency.¹⁰⁵ Hence, surface passivation of GaAs devices to prevent oxidation and corrosion is the key for enhancing the durability and performance of GaAs devices. Because sulfur species can bind to both Ga and As atoms to passivate unsaturated binding sites and form a thin protective layer on a GaAs surface, scientists have attempted to use several sulfur compounds to passivate a GaAs surface such as $(\text{NH}_4)_2\text{S}$, Na_2S , and normal alkanethiols.¹⁰⁶⁻¹⁰⁷

However, when GaAs is treated with the first two inorganic salts, toxic H₂S is produced. Moreover, passivation layers on the GaAs surface formed by all three kinds of compounds are less than 2 nm thick, which means that oxygen can still diffuse into the protective film to oxidize the GaAs surface after 2 days.¹⁰⁸

In 1997, Kauffman and coworkers discovered that MPTMS SAM was a good candidate for GaAs surface passivation.⁹⁶ After years of development, MPTMS has been widely used in GaAs devices such as solar cells and GaAs-based sensors, and the process used for surface passivation has become efficient and mature.⁹⁵ As shown in Figure 1.22c, after hydrolysis in solutions of more concentrated MPTMS and NH₄OH, the MPTMS monolayer formed on GaAs is crosslinked with other MPTMS molecules in the solution phase, which forms a 3D polysiloxane network. Finally, a relatively thick polymeric layer on the GaAs surface is generated, with the thickness for the resulting films ranging from 15 nm to 33 nm, which is controlled by varying the concentration of the MPTMS and NH₄OH solutions.⁹⁵ The results show that GaAs devices with MPTMS coatings show long-term stability in air or aqueous environments for at least 10 days, without sacrificing their original performance.

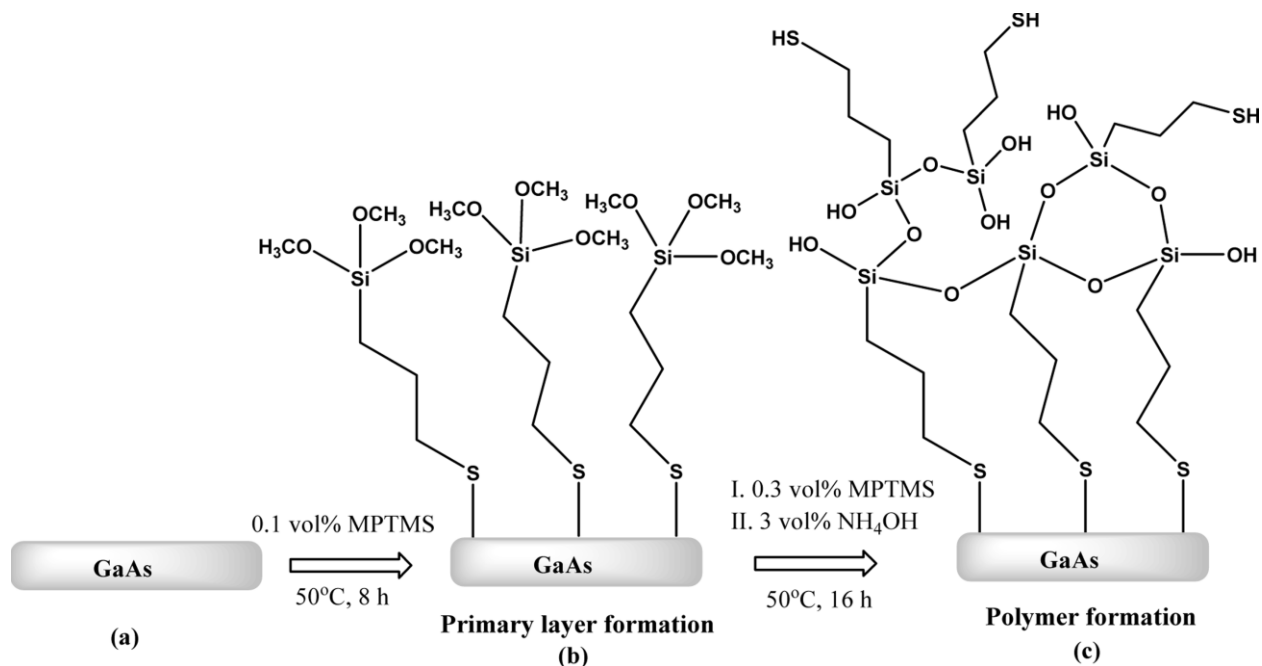


Figure 1.22. Schematic representation of a MPTMS coating on the surface of GaAs: (a) cleaned and etched GaAs sample, (b) primary layer formation, and (c) polymer formation. Reprinted with permission from reference 99, copyright 2016 American Chemical Society.

Moreover, in 2002, Seitz and coworkers achieved polymerization of MPTMS in a solution sol-gel process for GaAs surface passivation.¹⁰⁸ In the follow-up research, this process was further developed to be used as an anti-corrosion coating for copper by Sui et al.⁹⁸ Unlike the method introduced above, a polysiloxane network was formed by the polymerization of MPTMS in solution before being coated onto the copper surface.

1.6. Crosslinked SAMs realized by hydrogen bonding

In addition to crosslinking with covalent bonding, another important type of crosslinked SAMs are SAMs with noncovalent interaction such as hydrogen bonding. Generally, the hydrogen bonding within these crosslinked SAMs arises from the amide functional group or carboxylic acid group in the tailgroups. In 1994, Rablot and coworkers synthesized semifluorinated amidethiol, which was the first reported crosslinked SAM with hydrogen bonding, as shown in Figure 1.23a.¹⁰⁹

In a follow-up study, Whitesides and coworkers continued this research and synthesized series of amidethiol SAMs, which were terminated with different functional groups, such as CH₃, OH, CF₃, COOH, etc., as shown in Figure 1.23b.¹¹⁰ In 1997, Sastry et al. prepared a 4-carboxythiophenol SAM, with the carboxylic acid moieties forming a hydrogen-bonding network at low pH, as shown in Figure 1.23c.¹¹¹ In 2005, Kim et al. synthesized SAMs with a urea moiety on gold, which formed a hydrogen-bonding network, as shown in Figure 1.23d.¹¹²

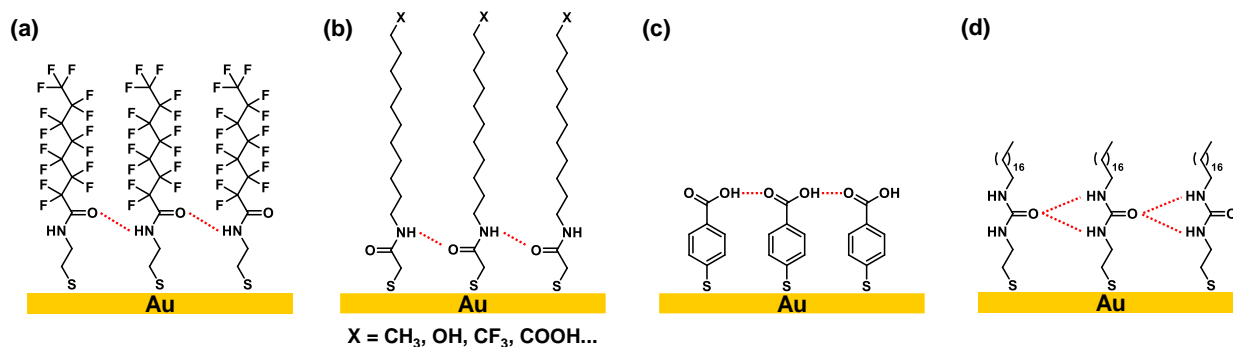


Figure 1.23. Structures of 4 different crosslinked SAMs realized by hydrogen bonding.¹⁰⁹⁻¹¹²

When SAMs containing carboxylic acid, amide, and urea groups are absorbed on gold, hydrogen-bonding networks are formed spontaneously. In the case of the SAM containing a urea moiety in Figure 1.23d, infrared reflection-absorption (IRRA) spectra obtained for the SAM on gold show almost no amide I band, which appears at 1621 cm⁻¹ in the spectra obtained for the bulk molecules.¹¹² This result proved that hydrogen-bonding exists in the SAM network, which is composed of N-H and C=O bonds parallel to the surface, since only vibrations aligned with the surface normal appear in the IRRA spectra due to the metal-surface selection rule. In 2016, Thomas et al. used scanning tunneling microscopy (STM) to map the hydrogen bonding networks formed in SAMs with an amide group.¹¹³ The submolecular-resolution STM images showed a linear pattern of molecule orientation (tilts) affected by hydrogen bonding, which further confirmed the existence of hydrogen bonding in the SAM network.

In the follow-up research, Liedberg and coworkers studied the thermal stability of SAMs influenced by hydrogen bonding, as measured by temperature-programmed desorption (TPD).¹¹⁴ They noted that SAMs with amide moieties show better thermostability compared to their normal alkanethiols analogs, with a temperature difference of 25 K for the thermodesorption, due to the hydrogen bonding. Moreover, Sastry et al. studied the effect of a 4-carboxythiophenol SAM on the selective binding of Cd and Pb cations at a surface using a Quartz Crystal Microbalance (QCM).¹¹¹ As shown in Figure 1.24, at low pH, the carboxylic acid groups at the interface are protonated and form a hydrogen-bonding network. They deprotonate and bind to cations in the form of $\text{Cd}(\text{OH})^+$ or $\text{Pb}(\text{OH})^+$, through an ion-exchange process. In addition, Rotello and coworkers investigated the position of the amide group in the alkyl chain in SAM-coated gold nanoparticles.¹¹⁵ Their results showed that when the amide group is near the SAM interface, intermonolayer hydrogen bonding leads to the aggregation of nanoparticles.

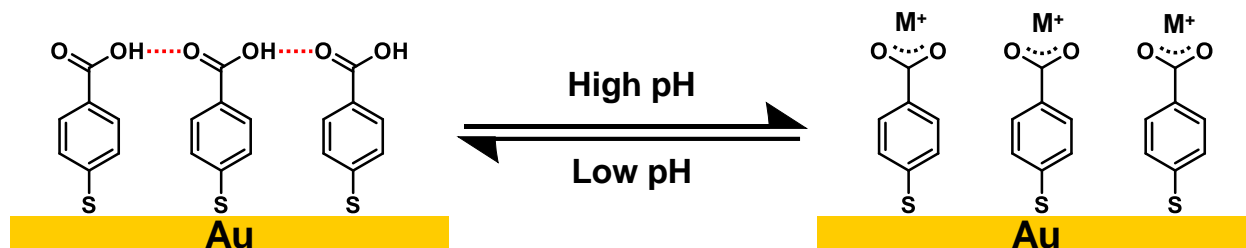


Figure 1.24. Schematic representation of 4-carboxythiophenol SAM on Au at low pH, and ion adsorption ($\text{M}^+ = \text{Cd}(\text{OH})^+$ or $\text{Pb}(\text{OH})^+$) at high pH. Adapted from reference 111, copyright 1997 American Chemical Society.

1.7. Boronic Acid-Based Alkanethiols

In 1994, Whiteside and coworkers utilized boronic acid-based alkanethiols to fabricate a crosslinked boronic anhydride surface.¹¹⁶ Although this research was focused on boronic acid-based SAMs,¹¹⁷ subsequent research for boronic acid-based SAMs for crosslinking is limited.

Additionally, there exists only limited research about the application of this kind of crosslinked SAM system.

A crosslinked boronic anhydride surface was first fabricated by the condensation of 11-mercaptoundecanyl-1-boronic acid, $\text{HS}(\text{CH}_2)_n\text{B}(\text{OH})_2$ in dry hydrocarbon solvents, such as isooctane, or under vacuum, as shown in Figure 1.25.¹¹⁶ This reaction is reversible, and the crosslinked film can be converted back into a pristine monolayer in aqueous ethanol. The author also found that in dry hydrocarbon solvents, $\text{HS}(\text{CH}_2)_n\text{B}(\text{OH})_2$ molecules in the solution phase reversibly turn into trimers that adsorb onto gold and form a hydrophobic boroxine bilayer. The resulting hydrophobic bilayer can be converted into a hydrophilic monolayer again in aqueous ethanol. Similar to hydroxyl-terminated SAMs, both the $\text{HS}(\text{CH}_2)_n\text{B}(\text{OH})_2$ SAM and its crosslinked film can couple with alkyltrichlorosilanes irreversibly, turning into a borosilicate network.

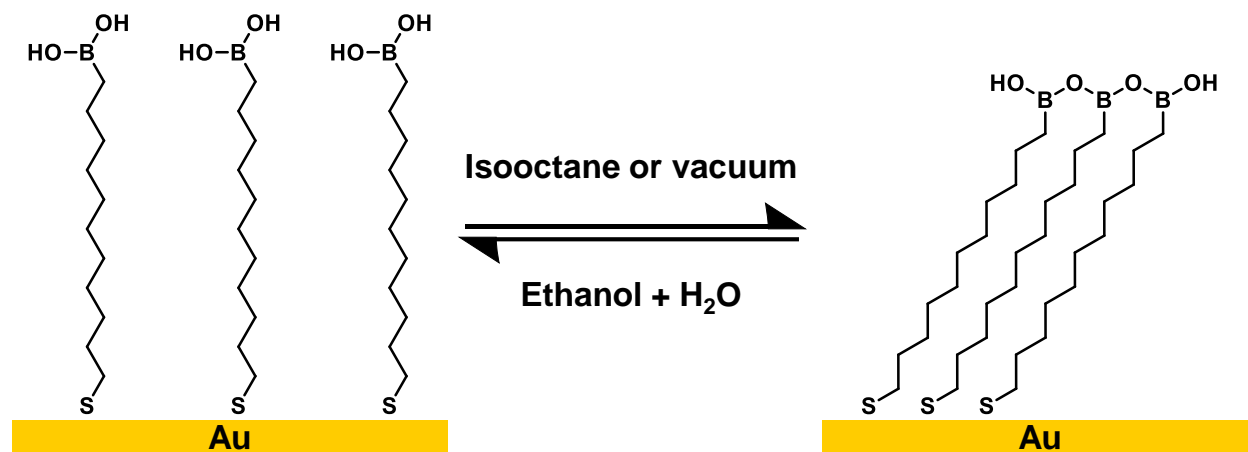


Figure 1.25. Schematic representation of a crosslinked boronic anhydride surface. Adapted from reference 116, copyright 1994 American Chemical Society.

The thermodesorption result shows that the crosslinked boronic anhydride SAM is 5 times more stable compared to the structurally analogous 11-hydroxyundecane-1-thiol at 147 °C.

However, it is difficult to tune the thickness or crosslinked area of crosslinked boronic acid-based SAMs. Moreover, the formation of crosslinked boronic anhydride surface is reversible. These drawbacks hinder the application of crosslinked boronic acid-based SAMs compared to other crosslinked systems such as aromatic thiol-based SAMs.

1.8 Summary

This review examines a variety of crosslinked SAMs: (1) aromatic thiol-based SAMs, (2) olefinic- and acetylenic-based alkanethiols, (3) other aliphatic alkanethiols, (4) silane-based alkanethiols, (5) boronic acid-based alkanethiols, and (6) crosslinked SAMs realized by hydrogen bonding. Their formation including the conditions for crosslinking, the structures of the crosslinked product, and interfacial properties were discussed. Furthermore, we highlighted the applications of such crosslinked SAMs in materials science, such as the fabrication of carbon nanomembranes, lithography, protective coatings, surface functionalization, and surface-initiated polymerization. In addition, this review offers insight into the structure-property relationships of crosslinked SAMs, as well as inspiring researchers toward the development of new types of SAMs with enhanced stabilities.

Chapter 2: Mimicking Polymer Surfaces Using Cyclohexyl- and Perfluorocyclohexyl-Terminated Self-Assembled Monolayers

*Chapter previously published as:

Yu, T.; Marquez, M. D.; Zenasni, O.; Lee, T. R. Mimicking the Surface of Polymers Using Cyclohexyl-Terminated Organic Thin Films. *ACS Appl. Nano Mater.* **2019**, 2, 5809–5816.

2.1. Introduction

Polymer coatings are widely used as protective layers in industrial settings for devices working under a wide range of conditions.¹¹⁸ The flexibility, ease of application, and their lightweight properties render polymer coatings attractive for use as a protective layer on various types of surfaces to protect against corrosion and/or mechanical damage.¹¹⁹ The most commonly used polymers for coatings in industry are polyethylene (PE) and polytetrafluoroethylene (PTFE). Since its discovery in 1941,¹²⁰ PTFE has been used in diverse applications due to its excellent properties, which include low surface friction,¹¹⁹ high chemical and thermal stability,¹²¹ high hydrophobicity and oleophobicity,¹²² these characteristics have allowed PTFE to become the candidate of choice in certain coating applications.¹²³ Regarding the microstructure of PTFE, the polymer chains adopt two types of morphologies that coexist: crystalline and amorphous.¹²⁴⁻¹²⁵ In the crystalline region of PTFE, the helical chains align themselves parallel to each other, while in the amorphous region, their arrangement is random.¹²⁶⁻¹²⁷ Crystalline PTFE undergoes rapid and complicated phase transitions near room temperature.¹²⁸⁻¹²⁹ Compared to rigid materials, such as inorganic crystals, polymers behave more like viscous liquids than solids due to the relatively weak van der Waals interactions between the polymer chains.¹³⁰ This characteristic is particularly true

for PTFE, as PTFE exhibits significant wear under sliding conditions and cold-flow behavior under stress.^{119,131}

To construct nanoscale PE and PTFE thin films, an understanding of the microstructure of polymeric interfaces becomes essential in coating applications. Among the numerous analytical techniques available, the measurement of contact angles is an inexpensive tool for investigating the interfacial properties of organic thin films.¹³²⁻¹³³ In a common coating method, small particles of the polymer are sprayed onto an uncoated surface followed by sintering to form a polymer film.¹³⁴ However, it is difficult to control the homogeneity of polymer surfaces on the nanoscale. In addition to being rough, polymer surfaces are sensitive to surface reconstruction under changing conditions.¹³⁵ When a liquid is in contact with a polymer surface, the liquid can intercalate between the polymer chains and cause reconstruction of the surface, also known as swelling.¹³⁶ Polymers that swell under the influence of a contacting liquid exhibit a decrease in the contact angle and an increase in the hysteresis value.¹³⁷⁻¹³⁸ Notably, the study of structure-property relationships of polymeric surfaces, particularly for nanotribology purposes, continues to receive attention. The aforementioned shortcomings and the continuing miniaturization of devices are driving the need to develop an ideal model to better understand polymer interfaces, without surface reconstruction, and subsequently the development of improved nanoscale low friction polymer coatings.¹³⁹⁻¹⁴¹

Since Nuzzo and Allara published their work on the monolayer assembly of organic adsorbates on gold substrates,¹ self-assembled monolayers (SAMs) have been used in a variety of fields, including corrosion prevention,¹⁴² electronic applications,¹⁴³ microelectromechanical systems (MEMS) devices,¹⁰ biomaterial coatings,¹⁴⁴ and biosensors.¹⁴⁵ Researchers have also used SAMs as model systems to investigate structure-property relationships due to the ability to

synthetically alter the adsorbate to impart selected packing densities or expose specific terminal functionalities.¹⁴⁶ For example, the Wysocki group utilized ion-surface collisions to characterize organic thin films derived from alkyl- and fluoroalkyl-terminated SAMs on gold.¹⁴⁷ Moreover, the ability to tailor the terminal functionality of an adsorbate allowed for the use of fluorinated SAMs (FSAMs) to generate functionalized surfaces with low wettability and coefficients of friction.¹⁴⁸⁻¹⁵¹ In related work, Barriet and co-workers used cyclopropyl-terminated SAMs to mimic the structural and interfacial properties (i.e., wettability) of polyethylene (PE)-based films.¹⁵² The resemblance in the wettability data of cyclopropyl-terminated SAMs and PE-based surfaces provided insight into the relationship between the interfacial properties and nanostructure of polymer interfaces.

In the present study, we designed cyclohexyl- and perfluorocyclohexyl-terminated monolayer films on gold to serve as mimics to the surfaces of the commercially relevant polymers PE and PTFE, respectively. These films were generated from the cyclohexyl-terminated alkanethiols (**HCyHnSH**; n = 10 and 11) and their fluorocarbon analogs $C_6F_{11}(CH_2)_nSH$ (n = 10 and 11; **FCyHnSH**) (see Figure 2.1). This study is based on the premise that **HCyHnSH**-based films would expose an interface comprised of CH_2 groups, which can mimic the surface/backbone of PE films; conversely, we anticipated that **FCyHnSH**-based films would expose an interface comprised of CF_2 groups, which can mimic the surface/backbone of PTFE films (see Scheme 2.1).

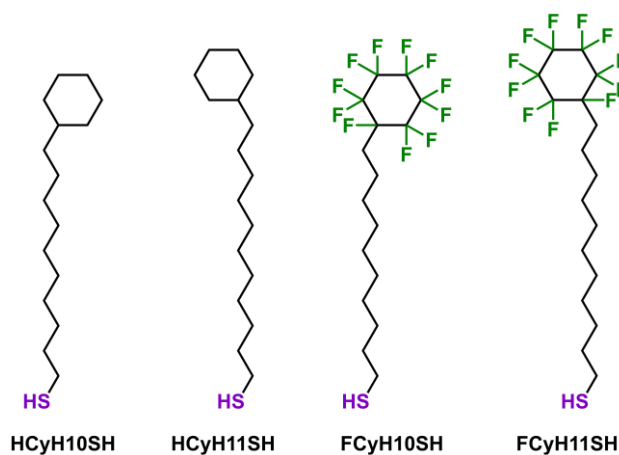
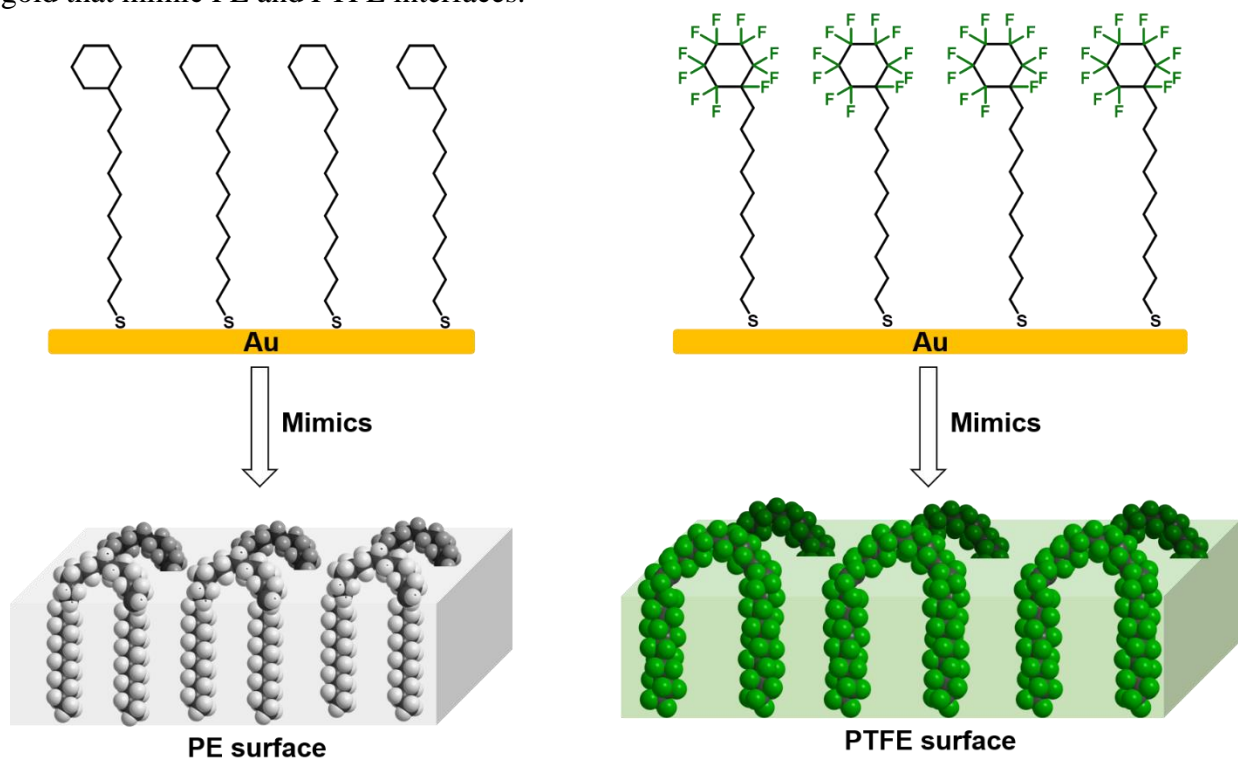


Figure 2.1. Molecular structures of the cyclohexyl-terminated thiols used in this study.

Scheme 2.1. Illustration of the investigated SAMs, **HCyHnSH** (left) and **FCyHnSH** (right), on gold that mimic PE and PTFE interfaces.



Studies of these films will allow us to evaluate the interfacial properties of solely CH₂ and CF₂ termini, which closely resemble polymeric backbones, without the facile surface reconstruction found in polymer-based films. Importantly, the **FCyHnSH** SAMs offer a rare

system in which the van der Waals forces of CF₂-based interfaces can be unambiguously evaluated. Prior studies of fluorinated SAMs and related thin films have been limited to systems in which the interface is comprised in whole or in part by CF₃ moieties, which are quite distinct from PTFE-based surfaces.^{148,150,153-154} Additionally, we envisioned that the permanent dipole at the FC-HC junction in **FCyHnSH** SAMs would be buried underneath the bulky perfluorocyclohexyl group, which would eliminate its effects on the interfacial energy of the SAM,^{148,153-154} rendering this system similar to the surface of PTFE. Furthermore, the cyclohexane terminus suffers from little ring strain and is more flexible than our previously studied cyclopropyl system,¹⁵² which allows all carbon atoms in the cyclohexyl system to adopt sp³ hybridization as in linear PE chains. Similarly, and given the synthetic challenges associated with the perfluorocyclopropyl group, we chose the perfluorocyclohexyl tailgroup to generate CF₂ interfaces. As a whole, these considerations compelled us to pursue SAMs with cyclohexyl termini to model and study PE and PTFE surfaces.

In this study, ellipsometry (to evaluate the thickness of the films), X-ray photoelectron spectroscopy (XPS, for elemental analysis), and polarization modulation reflection-absorption infrared spectroscopy (PM-IRRAS, to evaluate the orientation and conformational order of the films) were used to characterize the investigated SAMs formed from the cyclohexyl-terminated adsorbates and octadecanethiol (**H18SH**), which served as a reference standard. The interfacial wettability of the SAMs, PE, and PTFE films were characterized using contact angle measurements.

2.2. Experimental Procedures

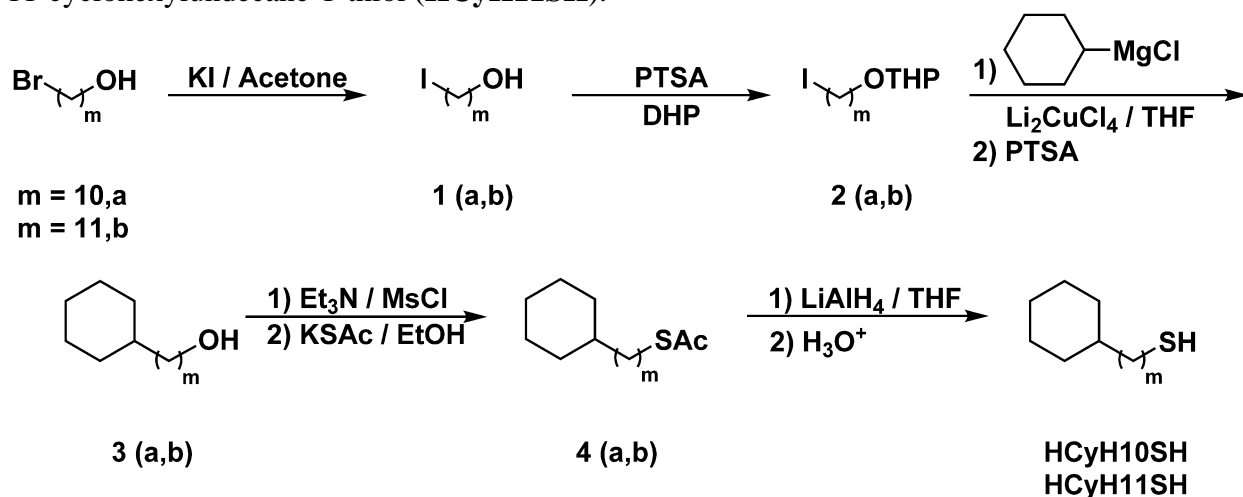
2.2.1. Materials and Methods

Tetrahydrofuran (THF – Avantor Performance Materials), dichloromethane (DCM – Macron Chemicals), and diethyl ether (Et₂O – J.T. Baker), along with toluene from Sigma Aldrich, were dried by distilling over calcium hydride (Sigma Aldrich). The other solvents, methanol (MeOH), hexanes, and acetone (from Avantor Performance Materials); ethyl acetate (Sigma Aldrich); and ethanol (EtOH – Aaper Alcohol and Chemical Co.), were either used as received or degassed by purging with nitrogen gas. Cyclohexylmagnesium chloride, methanesulfonyl chloride (MsCl), 2,2'-azobis(2-methylpropionitrile) (AIBN), lithium aluminum hydride (LiAlH₄), borane tetrahydrofuran complex (BH₃-THF), triethylamine (Et₃N), *p*-toluenesulfonic acid (PTSA), and 3,4-dihydro-2H-pyran (DHP) were all purchased from Sigma Aldrich and used as received. 9-Decen-1-ol (TCI America); iodoperfluorocyclohexane (TCI America); 10-undecen-1-ol (both from Oakwood Chemical) and potassium thioacetate (KSAc – Sigma Aldrich) were used as received. The lithium copper chloride (Li₂CuCl₄) solution was prepared from lithium chloride (LiCl) and copper (II) chloride (CuCl₂), which were each obtained from Acros Chemicals. Hydrochloric acid (HCl); sulfuric acid (H₂SO₄ – both from J.T. Baker); hydroiodic acid (HI) and zinc dust (Fischer); potassium iodide (KI – EMD Chemicals); glacial acetic acid (AcOH) and ammonium chloride (NH₄Cl – both from Mallinckrodt Chemicals), were all used as received. The adsorbate 1-octadecanethiol (**H18SH**) was purchased from Sigma-Aldrich. Chloroform-*d* was purchased from Cambridge Isotope Laboratories and used to collect all NMR spectra. Silica gel for column chromatography was obtained from Sorbent Technologies.

2.2.2. Synthesis of the Adsorbates

10-Cyclohexyldecane-1-thiol (**HCyH10SH**) and 11-cyclohexyl-undecane-1-thiol (**HCyH11SH**) were prepared following the synthetic route outlined in Scheme 2.2 below. 10-(Perfluorocyclohexyl)decane-1-thiol (**FCyH10SH**) and 11-(perfluorocyclohexyl)-undecane-1-thiol (**FCyH11SH**) were synthesized following the procedure depicted in Scheme 2.3 (vide infra).

Scheme 2.2. Synthetic route for the preparation of 10-cyclohexyldecane-1-thiol (**HCyH10SH**) and 11-cyclohexylundecane-1-thiol (**HCyH11SH**).



10-Iododecan-1-ol (1a). 10-Bromodecan-1-ol (1.00 g; 4.22 mmol) was dissolved in 100 mL of acetone, and potassium iodide (7.01 g; 42.2 mmol) was added to the mixture. The reaction was refluxed for 24 h. After cooling to rt, excess potassium iodide was filtered, and acetone was removed by rotary evaporation. The reaction mixture was redissolved in Et_2O (200 mL). The organic phase was washed with water (100 mL), followed by brine (100 mL), and then dried over MgSO_4 . After filtration, the solvent was removed by rotary evaporation and dried under vacuum to afford 10-iododecan-1-ol in 93% yield. ^1H NMR (400 MHz, CDCl_3): δ 3.64 (t, $J = 6.64$ Hz, 2H), 3.19 (t, $J = 7.10$ Hz, 2H), 1.81 (q, $J = 7.21$ Hz, 2H), 1.54–1.59 (m, 2H), 1.24–1.40 (m, 12H).

11-Iodoundecan-1-ol (1b) in 93% yield. $^1\text{H NMR}$ (400 MHz, CDCl_3): δ 3.64 (t, $J = 6.64$ Hz, 2H), 3.19 (t, $J = 7.10$ Hz, 2H), 1.81 (q, $J = 7.21$ Hz, 2H), 1.54–1.59 (m, 2H), 1.24–1.42 (m, 14H).

2-((10-iododecyl)oxy)tetrahydro-2H-pyran (2a). 10-iododecan-1-ol (1.10 g; 3.87 mmol) and dihydropyran (0.488 g; 5.81 mmol) were sequentially added to 100 mL of dichloromethane containing PTSA (0.074 g; 0.387 mmol). The reaction mixture was stirred at rt for 4 h. The mixture was then diluted with hexanes (200 mL) and washed twice with brine (2×100 mL) to remove the PTSA. The organic phase was dried over MgSO_4 , and the solvent removed by rotary evaporation to give *2-((10-iododecyl)oxy)tetrahydro-2H-pyran, 2a*, which was then dried under vacuum and carried to the next step without further purification. $^1\text{H NMR}$ (400 MHz, CDCl_3): δ 4.56 (m, 1H), 3.85–3.90 (m, 1H), 3.70–3.75 (m, 1H), 3.48–3.51 (m, 1H), 3.36–3.40 (m, 1H), 3.19 (t, $J = 7.10$ Hz, 2H), 1.78–1.88 (m, 4H), 1.51–1.60 (m, 4H), 1.21–1.27 (m, 14H).

2-((11-iodoundecyl)oxy)tetrahydro-2H-pyran (2b) $^1\text{H NMR}$ (400 MHz, CDCl_3): δ 4.56 (m, 1H), 3.84–3.89 (m, 1H), 3.70–3.75 (m, 1H), 3.48–3.51 (m, 1H), 3.36–3.40 (m, 1H), 3.18 (t, $J = 7.05$ Hz, 2H), 1.78–1.88 (m, 4H), 1.51–1.60 (m, 4H), 1.21–1.27 (m, 16H).

10-Cyclohexyldecane-1-ol (3a). In a 2-neck round-bottomed flask equipped with an addition funnel, iodide **2a** was dissolved in 100 mL of dry THF under nitrogen. To that solution, 3.9 mL of a 0.10 M solution of Li_2CuCl_4 (0.39 mmol) in THF were added. The mixture was then cooled to -78 °C, and a 2.0 M solution of cyclohexylmagnesium chloride solution in THF (4.8 mL; 9.7 mmol) was added dropwise over 15 min. The reaction was then warmed to rt and stirred under nitrogen for 12 h. The reaction was quenched with 25 mL of saturated NH_4Cl , followed by 25 mL of water. The mixture was extracted with Et_2O (3×100 mL), and the combined organic layers were washed with brine (1×100 mL) and dried over MgSO_4 . The solvent was removed with a

rotary evaporator, and the crude product used without further purification. The crude product was dissolved in 100 mL of ethanol containing PTSA (0.074 g; 0.387 mmol) and stirred at 55 °C for 3 h. After this interval, the ethanol was removed by rotary evaporation, and the residue redissolved in Et₂O (200 mL), washed with half-saturated brine (3 × 100 mL), and dried over MgSO₄. The solvent was evaporated to dryness by rotary evaporation. The crude alcohol was purified by silica gel chromatography using hexanes/ethyl acetate (80/20) as the eluent to give 10-cyclohexyldecan-1-ol in 85% yield. ¹H NMR (500 MHz, CDCl₃): δ 3.64 (t, *J* = 6.64 Hz, 2H), 1.60–1.72 (m, 4H), 1.54–1.59 (m, 3H), 1.10–1.38 (m, 20H), 0.81–0.90 (m, 2H).

11-Cyclohexylundecan-1-ol (3b) in 85% yield. ¹H NMR (500 MHz, CDCl₃): δ 3.64 (t, *J* = 6.64 Hz, 2H), 1.60–1.72 (m, 4H), 1.52–1.59 (m, 3H), 1.09–1.35 (m, 22H), 0.80–0.91 (m, 2H).

S-(10-Cyclohexyldecyl) ethanethioate (4a). 10-Cyclohexyldecan-1-ol (0.600 g; 2.50 mmol) was dissolved in anhydrous THF under nitrogen, and the solution was cooled to 0 °C in an ice bath. Triethylamine (1.00 mL; 7.50 mmol) was added slowly, and the resulting mixture was stirred for 30 min at 0 °C. After that, MsCl (0.74 mL; 10 mmol) was added dropwise. The reaction was warmed to rt and stirred for 6 h and subsequently quenched with 50 mL of water. The product was extracted with Et₂O (3 × 100 mL), and the combined organic phases were washed with 1M HCl (1 × 100 mL), water (1 × 100 mL), and brine (1 × 100 mL). The organic layer was dried over anhydrous MgSO₄, followed by removal of the solvent by rotary evaporation. The crude product was dried under high vacuum overnight then dissolved in 100 mL of absolute ethanol (previously degassed) under a flow of nitrogen. A portion of KSAc (0.502 g; 4.40 mmol) was then added to the solution, and the mixture was refluxed for 6 h. After cooling the reaction to rt, water was added (100 mL), and the product was extracted with Et₂O (3 × 100 mL). The organic phases were combined and washed with water (1 × 100 mL), brine (1 × 100 mL), and then dried over

MgSO₄. Removal of the solvent was done by rotary evaporation. The crude product was purified by silica gel chromatography using hexanes/ethyl acetate (95/5) as the eluent to give S-(10-cyclohexyldecyl) ethanethioate in 90% yield. ¹H NMR (500 MHz, CDCl₃): δ 2.86 (t, *J* = 7.45, 2H), 2.32 (s, 3H), 1.50–1.73(m, 7H), 1.08–1.40 (m, 20H), 0.81–0.90 (m, 2H).

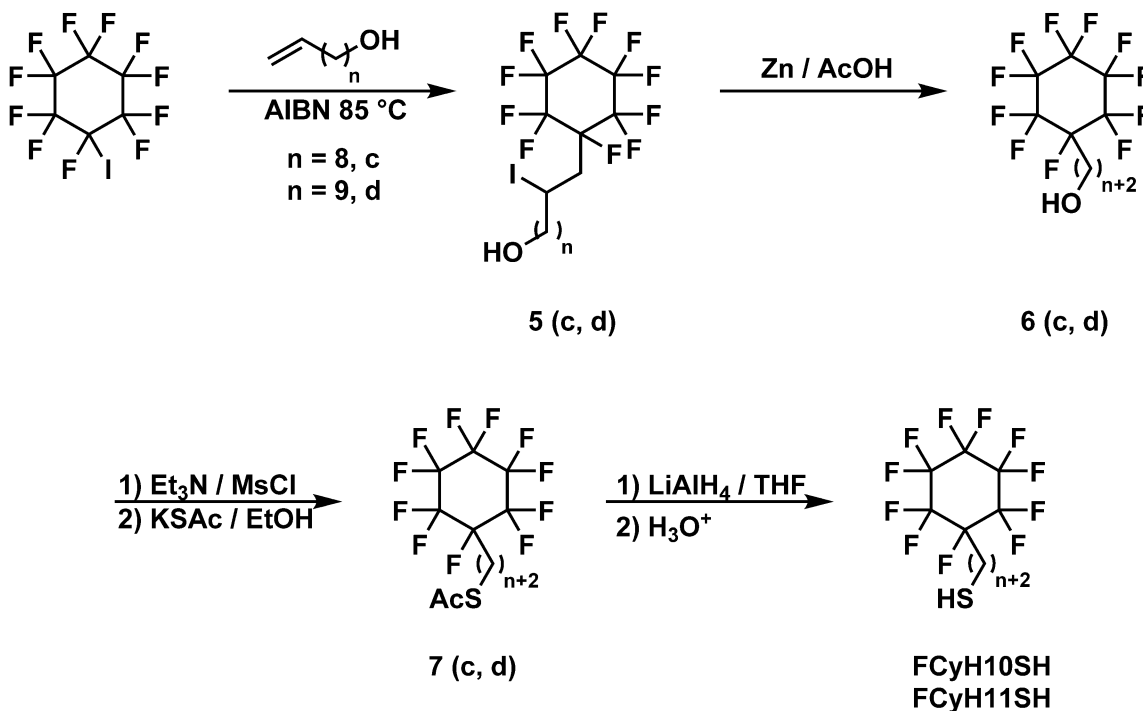
S-(11-Cyclohexylundecyl) ethanethioate (**4b**) in 92% yield. ¹H NMR (500 MHz, CDCl₃): δ 2.86 (t, *J* = 7.35, 2H), 2.32 (s, 3H), 1.50–1.73 (m, 7H), 1.08–1.38 (m, 22H), 0.80–0.90 (m, 2H).

10-Cyclohexyldecane-1-thiol (**HCyH10SH**). LiAlH₄ (0.0760 g; 2.01 mmol) was placed into a dry round-bottom flask. Then, dry THF (10 mL) was added to the flask at 0 °C to create a slurry. The thioacetate (0.200 g; 0.671 mmol) was dissolved in dry THF (50 mL) and added dropwise to the LiAlH₄ slurry. The reaction was then stirred at rt for 6 h under nitrogen and then quenched at 0 °C using water (25 mL, previously degassed); the resulting solution was then acidified with 1M H₂SO₄ solution (previously degassed). This mixture was extracted with Et₂O (3 × 100 mL). The combined organic phases were washed with water (1 × 100 mL) and brine (1 × 100 mL), dried over MgSO₄, and evaporated to dryness by rotary evaporation. The crude thiol was purified by column chromatography on silica gel (hexanes) to give 10-cyclohexyldecane-1-thiol (**HCyH10SH**) as a colorless oil in 88% yield. ¹H NMR (600 MHz, CDCl₃): δ 2.51 (q, *J* = 7.33 Hz, 2H), 1.57–1.74 (m, 7H), 1.31 (t, *J* = 7.56 Hz, 1H), 1.12–1.40 (m, 20H), 0.81–0.87 (m, 2H). ¹³C NMR (151 MHz, CDCl₃): δ 37.7, 37.6, 34.0, 33.4, 30.0, 29.8, 29.7, 29.6, 29.6, 29.5, 29.0, 28.4, 26.9, 26.7, 26.4, 24.6. HR-GC-MS, *m/z*: 256.2217 (C₁₆H₃₁SH⁺), 255.2146 (M⁺-H), 254.2064 (M⁺-2H), 253.1991 (M⁺-3H).

11-Cyclohexylundecane-1-thiol (**HCyH11SH**). Colorless oil in 85% yield. ¹H NMR (600 MHz, CDCl₃): δ 2.50 (q, *J* = 7.56 Hz, 2H), 1.55–1.72 (m, 7H), 1.31 (t, *J* = 7.56 Hz, 1H), 1.11–1.38 (m, 22H), 0.81–0.87 (m, 2H). ¹³C NMR (151 MHz, CDCl₃): δ 37.7, 37.5, 34.0, 33.4, 30.0,

29.7, 29.6, 29.5, 29.6, 29.0, 28.4, 26.9, 26.7, 26.4, 24.6. HR-GC-MS, m/z : 270.2368 ($C_{17}H_{33}SH^+$), 269.2307 (M^+-H), 268.2224 (M^+-2H), 267.2149 (M^+-3H).

Scheme 2.3. Synthetic Route for the Preparation of 10-(Perfluorocyclohexyl)decane-1-thiol (**FCyH10SH**) and 11-(Perfluorocyclohexyl)undecane-1-thiol (**FCyH11SH**)



9-Iodo-10-(perfluorocyclohexyl)decan-1-ol (5c). Iodoperfluorocyclohexane (2.00 g; 4.90 mmol), AIBN (0.080 g; 0.490 mmol), and 9-decen-1-ol (0.688 g; 4.41 mmol) were added to a 100-mL pear-shaped Schlenk flask. The system was degassed using three cycles of a standard freeze-pump-thaw procedure. After warming to rt, the reaction mixture was heated to 85 °C for 8 h. After cooling the reaction to rt, the crude mixture was purified by column chromatography over silica gel using hexanes/ethyl acetate (80/20) as the eluent system to give **5c** in 90% yield. 1H NMR (500 MHz, $CDCl_3$): δ 4.41 (m, $J = 4.20$ Hz, 1H), 3.65 (t, $J = 6.41$ Hz, 2H), 2.89–3.10 (m, 2H), 1.71–1.87 (m, 2H), 1.52–1.60 (m, 4H), 1.20–1.43 (m, 10H).

10-Iodo-11-(perfluorocyclohexyl)undecan-1-ol (5d) in 90% yield. ¹H NMR (500 MHz, CDCl₃): δ 4.41 (m, *J* = 4.35 Hz, 1H), 3.65 (t, *J* = 6.41 Hz, 2H), 2.88–3.10 (m, 2H), 1.70–1.87 (m, 2H), 1.53–1.61 (m, 4H), 1.20–1.42 (m, 12H).

10-(Perfluorocyclohexyl)decan-1-ol (6c). **5c** (2.50 g; 4.43 mmol) and zinc dust (2.30 g; 35.4 mmol) were suspended in 70 mL of glacial acetic acid under the flow of argon at rt. The reaction mixture was stirred for 40 h in the dark and then filtered through a bed of Celite. The Celite pad was then washed with 200 mL of Et₂O. The filtrate was washed with water (3 × 100 mL), saturated aqueous NaHCO₃ (1 × 100 mL), and brine (1 × 100 mL). The organic layer was then dried over MgSO₄, and the solvent was removed by rotary evaporation. The crude alcohol was purified by column chromatography over silica gel using hexanes/ethyl acetate (80/20) as the eluent system to give **6c** in 65% yield. ¹H NMR (500 MHz, CDCl₃): δ 3.64 (t, *J* = 6.30 Hz, 2H), 2.11–2.19 (m, 2H), 1.54–1.66 (m, 4H), 1.27–1.39 (m, 12H).

11-(Perfluorocyclohexyl)undecan-1-ol (6d) in 67% yield. ¹H NMR (500 MHz, CDCl₃): δ 3.64 (t, *J* = 6.55 Hz, 2H), 2.11–2.19 (m, 2H), 1.54–1.66 (m, 4H), 1.24–1.40 (m, 14H).

S-(10-(Perfluorocyclohexyl)decyl) ethanethioate (7c). Alcohol **6c** (1.20 g; 2.65 mmol) was dissolved in anhydrous THF under nitrogen, and the solution was cooled to 0 °C in an ice bath. Triethylamine (0.803 g; 7.95 mmol) was added slowly to the resulting mixture and stirred for 30 min at 0 °C. After that, MsCl (1.21 g; 10.6 mmol) was added dropwise. The reaction was warmed to rt, stirred for 6 h, and subsequently quenched with 50 mL of water. The product was extracted with Et₂O (3 × 100 mL), and the combined organic phases were washed with 1M HCl (1 × 100 mL), water (1 × 100 mL), and brine (1 × 100 mL). The organic layer was dried over anhydrous MgSO₄, followed by removal of the solvent by rotary evaporation. The crude mesylate was dried under high vacuum overnight and redissolved in 100 mL of absolute ethanol (previously

degassed) under a flow of nitrogen. A portion of KSAc (0.582 g; 5.11 mmol) was then added to the solution, and the mixture was refluxed for 6 h. After cooling the reaction to rt, water was added (100 mL), and the product was extracted with Et₂O (3 × 100 mL). The organic phases were combined and washed with water (1 × 100 mL) and brine (1 × 100 mL), and then dried over MgSO₄. The solvent was removed by rotary evaporation. The crude product was purified by silica gel chromatography using hexanes/ethyl acetate (95/5) as the eluent to give **7c** in 96% yield. ¹H NMR (500 MHz, CDCl₃): δ 2.86 (t, *J* = 7.56 Hz, 2H), 2.32 (s, 3H), 2.12–2.18 (m, 2H), 1.53–1.65 (m, 4H), 1.25–1.39 (m, 12H).

S-(11-(Perfluorocyclohexyl)undecyl) ethanethioate (**7d**) in 95% yield. ¹H NMR (500 MHz, CDCl₃): δ 2.86 (t, *J* = 7.21 Hz, 2H), 2.32 (s, 3H), 2.12–2.18 (m, 2H), 1.53–1.65 (m, 4H), 1.27–1.38 (m, 14H).

10-(Perfluorocyclohexyl)decane-1-thiol (**FCyH10SH**). LiAlH₄ (0.046 g; 1.2 mmol) was placed into a dry round-bottom flask followed by the addition of dry THF (10 mL, previously degassed) at 0 °C. The thioacetate (0.200 g; 0.403 mmol) was dissolved in dry THF (50 mL, previously degassed) and added dropwise to the LiAlH₄ slurry. The reaction was then stirred at 0 °C for 6 h under the flow of nitrogen. The reaction was quenched at 0 °C using water (25 mL, previously degassed), and the resulting solution was then acidified with 1M H₂SO₄ solution (previously degassed). The mixture was then extracted with Et₂O (3 × 100 mL). The combined organic phases were washed with water (1 × 100 mL) and brine (1 × 100 mL), dried over MgSO₄, and evaporated to dryness by rotary evaporation. The crude thiol was purified by column chromatography on silica gel (hexanes) to give **FCyH10SH** as a colorless oil in 55% yield. ¹H NMR (500 MHz, CDCl₃): δ 2.50 (t, *J* = 7.56 Hz, 2H), 2.11–2.18 (m, 2H), 1.57–1.65 (m, 4H), 1.30 (t, *J* = 7.54 Hz, 1H), 1.28–1.38 (m, 12H). ¹³C NMR (151 MHz, CDCl₃): δ 105.5–112.3, 91.6 (d,

$J = 201.1$ Hz), 34.0, 29.8, 29.4, 29.3, 29.1, 29.0, 28.3, 25.7 (d, $J = 20.7$ Hz), 24.6, 21.3. ^{19}F NMR (376 MHz, CDCl_3): δ -118.4 (d, $J = 296.4$ Hz, 2F), -122.6 (d, $J = 282.3$ Hz, 2F), -124.2 (d, $J = 285.0$ Hz, 1F), -132.9 (d, $J = 295.9$ Hz, 2F), -139.5 (d, $J = 283.9$ Hz, 2F), -142.3 (d, $J = 282.8$ Hz, 1F) -185.8 (s, 1F). HR-GC-MS, m/z : 454.1169 ($\text{C}_{16}\text{H}_{20}\text{F}_{11}\text{SH}^+$), 453.1109 ($\text{M}^+\text{-H}$), 452.1026 ($\text{M}^+\text{-2H}$).

11-(Perfluorocyclohexyl)undecane-1-thiol (FCyHIISH) as a colorless oil in 56% yield. ^1H NMR (500 MHz, CDCl_3): δ 2.52 (t, $J = 7.48$ Hz, 2H), 2.10 (m, 2H), 1.55–1.67 (m, 4H), 1.31 (t, $J = 7.56$ Hz, 1H), 1.25–1.42(m, 14H). ^{13}C NMR (151 MHz, CDCl_3): δ 105.5–112.3, 91.6 (d, $J = 201.1$ Hz), 34.0, 29.8, 29.4, 29.3, 29.1, 29.0, 28.3, 25.7 (d, $J = 20.7$ Hz), 24.6, 21.3. ^{19}F NMR (376 MHz, CDCl_3): δ -118.2 (d, $J = 385.8$ Hz, 2F), -122.5 (d, $J = 344.1$ Hz, 2F), -124.1 (d, $J = 158.2$ Hz, 1F), -132.9 (d, $J = 300.7$ Hz, 2F), -139.5 (d, $J = 299.1$ Hz, 2F), -142.3 (d, $J = 421.6$ Hz, 1F), -185.8 (s, 1F). HR-GC-MS, m/z : 468.1336 ($\text{C}_{17}\text{H}_{22}\text{F}_{11}\text{SH}^+$), 467.1274 ($\text{M}^+\text{-H}$), 466.1188 ($\text{M}^+\text{-2H}$) 465.1118 ($\text{M}^+\text{-3H}$).

2.2.3. Preparation and Characterization of the SAMs

Gold shot (99.999%) was purchased from Kamis Incorporated. Chromium rods (99.9%) were purchased from R. D. Mathis Company, and polished single-crystal Si(100) wafers were purchased from Silicon Wafer Enterprises. The gold substrates were prepared by thermal evaporation onto Si(100) wafers under vacuum at a pressure $\leq 6 \times 10^{-5}$ torr. Chromium (100 Å) was initially deposited at rate of $0.5 \text{ \AA} / \text{s}$ to aid the adhesion of the Au layer, then 1000 Å of Au was deposited at rate of $0.5 \text{ \AA} / \text{s}$. Immediately after vapor deposition, the substrates were cleaned with ultra-pure nitrogen gas. Solutions of the thiols at 1 mM concentration in absolute ethanol (previously degassed) were prepared in 40 mL vials that had been previously cleaned with piranha

solution and rinsed thoroughly with deionized water, followed by absolute ethanol. Two cut Au slides (2 cm × 1 cm) were then immersed into each of the thiol solutions and allowed to equilibrate for 48 h at rt in the dark. Before characterization, all films were rinsed with THF followed by absolute ethanol, and dried with ultra-pure nitrogen gas.

Thickness measurements were collected on a Rudolph Auto EL III ellipsometer equipped with a He-Ne laser (632.8 nm) at an incident angle set to 70° and the refractive index was set to 1.45. The reported thickness values are an average of 18 measurements (9 measurements per slide).

X-Ray photoelectron spectroscopy (XPS) measurements were performed using a PHI 5700 X-Ray photoelectron spectrometer with a monochromatic Al K α X-ray source ($h\nu = 1486.7$ eV) incident at 90° relative to the axis of the hemispherical energy analyzer. The takeoff angle from the surface was set at 45° with a pass energy of 23.5 eV. The Au 4f_{7/2} peak at 84.0 eV was used as a reference peak, with each spectrum set to align with that reference.

PM-IRRAS spectra were collected using a Nicolet Nexus 670 Fourier transform spectrometer equipped with a mercury-cadmium-telluride (MCT) detector and a Hinds Instrument PEM-90 photoelastic modulator. The collected spectra were from surfaces mounted at an incident angle of 80° for the p-polarized light with respect to the surface normal. For each sample, we collected 1024 scans at a resolution of 2 cm⁻¹.

Contact angle data were obtained using a compact high-resolution CMOS camera (DCC1645C) and 12X zoom lens (MVL12X12Z) working with a Matrix Technologies micro-Electrapette 25 dispensing liquids from a disposable pipette tip. Contacting liquids were of the highest purity available at the time of their purchase and were dispensed at a speed of 1 μ L/s to obtain advancing contact angles (θ_a) and withdrawn at the same speed to obtain receding contact angles (θ_r). The specific method used to collect the contact angle data was the dynamic sessile

drop procedure (where the liquid dispensing pipette remains in contact with the drop), with images taken during the dispensing and withdrawal of the contacting liquid, maintaining the pipette tip centered on the drop. The reported contact angle data represent the average of at least 12 measurements from 3 different locations for each SAM-coated slide. Adobe® Photoshop® was used to measure the angles on each side of the dispensed droplets. The following polar protic, polar aprotic, and nonpolar aprotic contacting liquids were used: water (W – Millipore water with a resistivity of 18.2 MΩ·cm), formamide (FM – Sigma Aldrich), methyl formamide (MF – Sigma Aldrich), dimethylformamide (DMF – Sigma Aldrich), acetonitrile (ACN – Sigma Aldrich), squalane (SQ – Sigma Aldrich) and hexadecane (HD – Aldrich).

Films of two polymers -- polyethylene (HDPE; linear, 2 mil thick film from Blueridge Films, Inc) and polytetrafluoroethylene (PTFE; Ultra Pure Virgin PTFE film, 2 mil thickness from Scientific Commodities) -- were flattened on polished metal surfaces by pressing with a mechanical press at 10,000 psi to produce thin sheets of PE and PTFE.

2.3. Results and Discussion

2.3.1. Ellipsometric Thickness Measurements.

Table 2.1 displays the average ellipsometric thickness measurements of the investigated SAMs on gold. The average thickness of the **H18SH** SAM was 22 Å, which is consistent with the value in the literature.² Data for the **H18SH** adsorbate serve as a reference standard to ensure the quality and reliability of the evaporated Au substrates used in the study.

Table 2.1. Ellipsometric thicknesses of the **H18SH**, **HCyHnSH**, and **FCyHnSH** SAMs

Adsorbate	Thickness (Å)
H18SH	22 ± 1
HCyH10SH	15 ± 1

HCyH11SH	14 ± 1
FCyH10SH	13 ± 1
FCyH11SH	12 ± 1

Separately, the ellipsometric thickness values for the **HCyHnSH** SAMs having 10 and 11 methylene groups are within the experimental error, ~14-15 Å. The same trend was also observed for the **FCyHnSH** SAMs, where molecules bearing 10 backbone methylene units have a thickness of ~13 Å and those with 11 hydrocarbons have a thickness of ~12 Å. The high similarity of the monolayer thicknesses, regardless of the size of the underlying hydrocarbon spacer, might be due to the hydrocarbon chains adopting a trans-extended conformation to maximize inter-chain van der Waals forces, which leads to similar packing densities in the fluorocarbon or hydrocarbon films.² Yet, we notice that the **HCyHnSH** SAMs showed a slightly greater thickness than the **FCyHnSH** SAMs, Table 2.1. The observed slightly lower thickness for the **FCyHnSH** SAMs might arise from a lower number of molecules per unit area in the fluorinated SAMs as compared to the hydrocarbon analogs. The van der Waals diameter of fluorine is 1.47 Å, which is larger than hydrogen (1.20 Å), leading to bulkier termini in the **FCyHnSH** SAMs.¹⁵⁵⁻¹⁵⁷ Another plausible reason for such a reduction might arise from the fluorinated films being more tilted than their hydrocarbon counterparts, which can also be attributed to the larger chain termini in the fluorinated films. Additionally, the reduction in thickness of the **FCyHnSH** SAMs might also be attributed to a reduction in the refractive index of fluorocarbons (1.33) compared to hydrocarbons (1.45); note, a refractive index of 1.45 was used for all of the SAMs to calculate thickness.¹⁵⁸⁻¹⁵⁹ Further analysis of the packing densities and conformational order of the chains in these films is detailed below in the XPS and PM-IRRAS sections, respectively.

2.3.2. Analysis of the Chemical Composition of the Films Using XPS.

In analyses of organic thin films, XPS is a commonly used technique for determining (1) the chemical composition of organic films, (2) the oxidation state of elements, (3) the nature of the bonding of adsorbates on surfaces, and (4) the relative chain packing densities of organic films.¹⁶⁰⁻

¹⁶¹ Figure 2.2 shows the XPS spectra of the binding regions of the Au 4f, S 2p, C 1s, and F 1s core electrons, respectively. The precise binding energies of the peaks in the spectra are provided in Table 2.2.

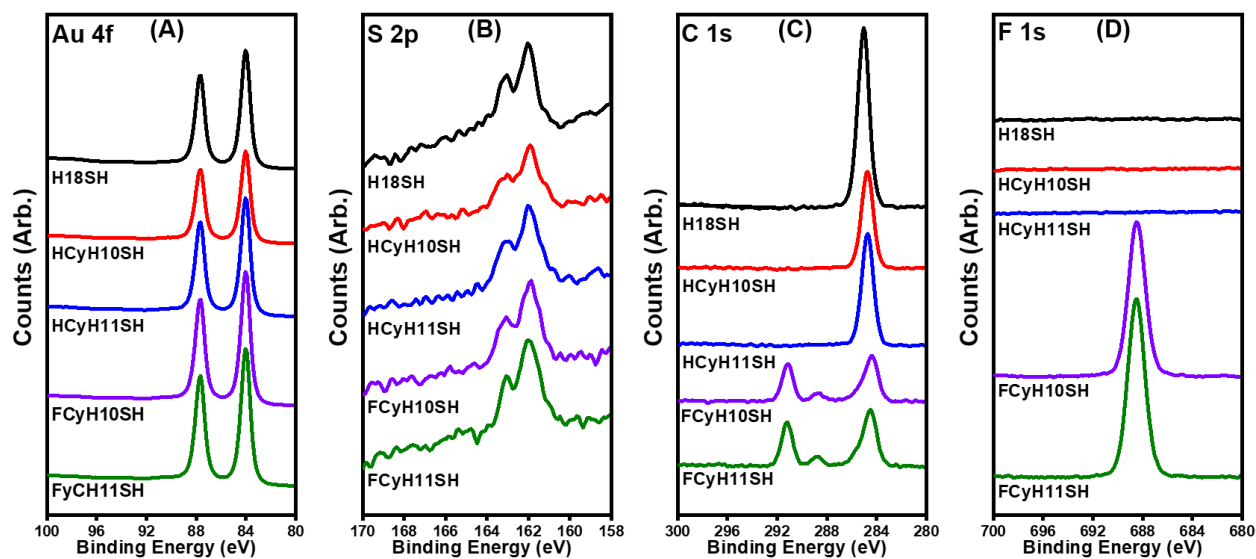


Figure 2.2. XPS spectra of the (A) Au 4f, (B) S 2p, (C) C 1s, and (D) F 1s binding regions of the SAMs.

Figure 2.2A shows the expected peaks for Au 4f in all of the SAMs. Spectra of the S 2p region, shown in Figure 2.2B, can be used to evaluate the binding of the thiol-based adsorbates to the Au surface.^{37,162-163} The spectra in Figure 2.2B exhibit a characteristic peak with spin-orbit splitting, which manifests as a doublet and is attributed to S 2p_{3/2} (~162.0 eV) and S 2p_{1/2} (163.0 eV). The peak appeared for all of the SAMs analyzed in the study and is consistent with the presence of bound thiolate.³⁷ Moreover, the absence of peaks at ~164 eV or 166 eV and higher

binding energy suggests the absence of unbound or highly oxidized sulfur species, respectively, in the investigated SAMs. Figure 2.2C shows the XPS spectra for the C 1s region; the peak positions are given in Table 2.2. For the **H18SH** reference SAM, one peak with a binding energy of 285.0 eV was apparent, which we attribute to all of the carbons with attenuation of the carbon directly attached to sulfur.³⁷ The XPS spectra of the **HCyHnSH** SAMs exhibited one peak at 284.7 eV, which indicates all of the C 1s electrons arise from the carbons of the cyclohexyl ring, the tertiary carbon attached to the alkyl chain, and the carbons of the alkyl chain. In contrast, the C 1s spectra of the **FCyHnSH** SAMs revealed two large peaks that can be attributed to the CH₂ and CF₂ units at ~284.4 eV and ~291.1 eV, respectively, with a small broad peak in between (~288.6 eV). We believe that the broad peak at ~288.6 eV corresponds to the CF carbon of the perfluorinated cyclohexyl ring attached to the alkyl chain, which is expected to have a lower binding energy than the more highly fluorinated CF₂ carbons.¹⁶⁴ As for the F 1s region, the **FCyHnSH** SAMs both exhibited a sharp peak at 688.4 eV, while the other SAMs showed no peaks in the F 1s region, which is consistent with the chemical structures of the adsorbates.

Table 2.2. XPS Binding Energies (eV) and Relative Chain Packing Densities of the investigated SAMs.

Adsorbate	C 1s (CH ₂) (eV)	C 1s (CF) (eV)	C 1s (CF ₂) (eV)	Relative Packing Density (%)	S 2p _{1/2} (eV)	S 2p _{3/2} (eV)	F 1s (eV)
H18SH	285.0	-	-	100	162.0	163.0	-
HCyH10SH	284.7	-	-	72 ± 5	161.9	163.0	-
HCyH11SH	284.7	-	-	71 ± 8	162.0	162.9	-
FCyH10SH	284.4	288.6	291.1	64 ± 6	161.8	163.0	688.4
FCyH10SH	284.5	288.7	291.1	63 ± 6	161.8	163.0	688.4

A quantitative analysis of the relative packing density can also be obtained from the XPS spectra. To evaluate the relative chain packing densities in the SAMs, we utilized the integrated

intensities of the S 2p and Au 4f core electrons from the XPS spectra to calculate the S/Au ratio.¹⁶⁵ In our analysis, the **H18SH** SAM was used as a reference for a system with 100% chain packing density. Further, since the attenuation of electrons by hydrocarbons and fluorocarbons is indistinguishable, the packing density of all SAMs was calculated in the same manner.¹⁶⁶ Table 2.2 shows the relative chain packing densities of all of the investigated SAMs.

Note that for cyclohexyl SAMs within the same series (i.e., for SAMs derived from **HCyHnSH** or **FCyHnSH**), all adsorbates adopted similar packing densities regardless of the length of the methylene spacer. For example, the packing densities of the **HCyH10SH** and **HCyH11SH** SAMs were 72% and 71%, respectively, while the **FCyH10SH** and **FCyH11SH** SAMs exhibited packing densities of 64% and 63%, respectively. Moreover, the data also show that the packing densities of the **HCyHnSH** SAMs were greater than those of the **FCyHnSH** SAMs. Such discrepancies are consistent with the progressive increase in the size of the chain termini in the **H18SH**, **HCyHnSH**, and **FCyHnSH** SAMs. Compared to the **H18SH** monolayers, the **HCyHnSH** SAMs have larger terminal groups, which reduces the relative packing densities of the chains to ~72%. This effect is further augmented in the **FCyHnSH** SAMs, where the perfluorocyclohexyl termini leads to a reduction in the relative packing densities of these films to ~64%. This latter decrease is plausibly due to the increase in the van der Waals (vdW) volume of the chain termini after the replacement of hydrogen atoms (vdW radius of 1.20 Å) with fluorine atoms (vdW radius of 1.47 Å),⁴² which makes perfluorinated cyclohexyl tailgroups more sterically bulky (and more rigid) than their hydrocarbon analogs.

The C 1s binding energy region can also be used to provide a qualitative assessment of the relative packing density for a series of structurally similar SAMs.¹⁶⁷ The values of the binding energy of the C 1s core electrons generated from the CH₂ units corroborates the above-mentioned

analysis of changes in the relative packing densities as a function of terminal group size. The binding energies of the C 1s electrons originating from the CH₂ decrease with an increase in the size of the chain termini. For example, the binding energy of C 1s electrons decreased from 285.0 for the **H18SH** SAM to 284.7 eV for the **HCyHnSH** SAMs. Similarly, the aliphatic C 1s binding energy for the **FCyHnSH** SAMs decreased further to ~284.4 eV. This phenomenon arises due to a final state effect, where positive charges generated from the photoelectron emission are easily screened in films with lower packing densities (i.e., weaker insulators) than in densely packed films, which gives rise to an increase in the energy required to eject electrons from the latter films.¹⁶¹ For the SAMs within a series (i.e., **HCyH10SH** and **HCyH11SH** vs. **FCyH10SH** and **FCyH11SH**), there was no observable difference in the binding energies, indicating the chain length of the spacer has no effect on the packing density of the films. In summary, evaluation of the C 1s binding energies of these films shows that the packing densities decrease in the following order: **H18SH** > **HCyHnSH** > **FCyHnSH**, which is consistent with the observed S/Au ratios.

2.3.3. Assessment of Chain Conformational Order Using PM-IRRAS.

IR spectroscopy of surfaces has proven to be a valuable tool for probing the relative conformational order and orientation of molecules within a SAM.¹⁶⁸ In particular, the position of the methylene antisymmetric stretching band ($\nu_{\text{as}}^{\text{CH}_2}$) of the hydrocarbon backbone can be used to evaluate the conformational order (i.e., crystalline nature).¹⁶⁹ Figure 2.3 shows the PM-IRRAS spectra for the C–H stretching region of the current set of SAMs.

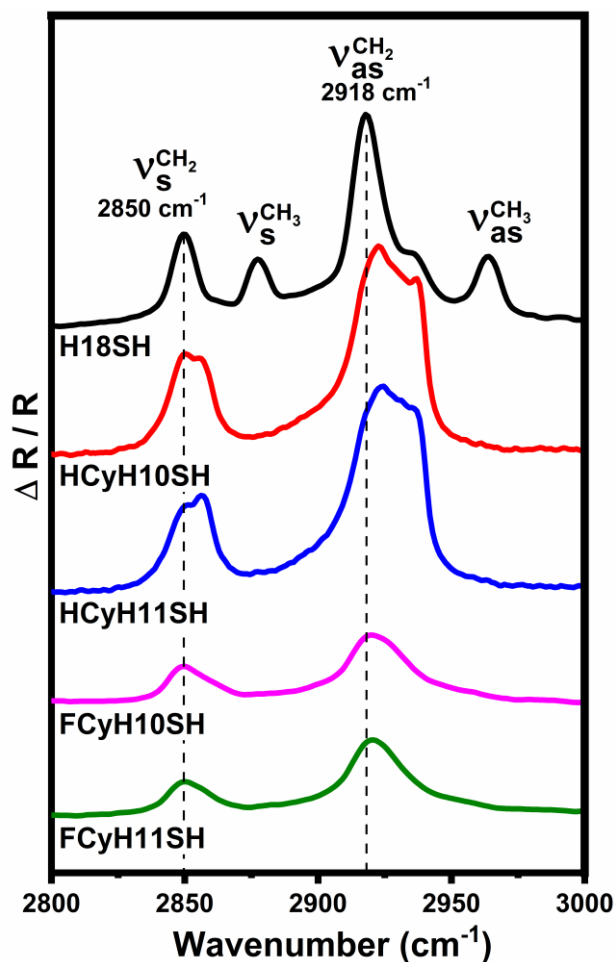


Figure 2.3. PM-IRRAS spectra showing the C–H stretching region of the **H18SH**, **HCyHnSH**, and **FCyHnSH** SAMs.

Table 2.3 presents the precise peak assignments (cm^{-1}) in the PM-IRRAS spectra of the current set of SAMs. For well-ordered alkanethiol monolayers, such as the **H18SH** SAM, the $\nu_{\text{as}}^{\text{CH}_2}$ stretch has been assigned at 2918 cm^{-1} , which indicates a trans-extended crystalline conformation.¹⁶⁹ However, these bands tend to blue shift in the case of poorly-ordered (liquid-like) SAMs.¹⁷⁰ For the purpose of peak assignment, deconvoluted spectra of the **HCyHnSH** SAMs are provided in the Figure 2.4.

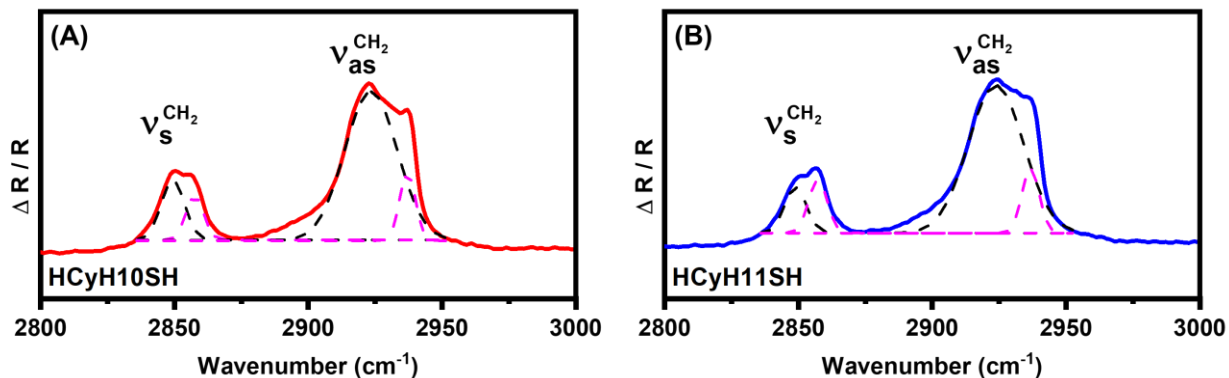


Figure 2.4. Deconvolution of the peaks in PM-IRRAS spectra of (A) **HCyH10SH** and (B) **HCyH11SH**.

For the **HCyHnSH** series, we observed a consistent positioning of the $\nu_{\text{as}}^{\text{CH}_2}$ stretch (2923-2924 cm^{-1}), regardless of chain length, for both the **HCyH10SH** and **HCyH11SH** SAMs, which is in agreement to analogously structured phosphonic acid SAMs on metal oxide surfaces.¹⁷¹ In addition, we observed broadening of both $\nu_{\text{s}}^{\text{CH}_2}$ and $\nu_{\text{as}}^{\text{CH}_2}$ peaks in the spectra, which might be due to an overlap between the peaks of the methylene units of the alkyl chain and those in the cyclohexane ring. Furthermore, the PM-IRRAS spectra of the **FCyH10SH** and **FCyH11SH** SAMs also displayed similar characteristics despite the difference in the hydrocarbon chain length. The $\nu_{\text{as}}^{\text{CH}_2}$ of the **FCyHnSH** SAMs was located at $\sim 2920 \text{ cm}^{-1}$, which indicates that the methylene chains of the fluorinated SAMs are slightly more ordered than their hydrocarbon analogs.

Table 2.3. Peak Assignments (cm^{-1}) for the PM-IRRAS Spectra of the **H18SH**, **HCyHnSH**, and **FCyHnSH** SAMs

Adsorbate	$\nu_{\text{s}}^{\text{CH}_2}$ (cm^{-1})	$\nu_{\text{s}}^{\text{CH}_3}$ (cm^{-1})	$\nu_{\text{as}}^{\text{CH}_2}$ (cm^{-1})	$\nu_{\text{as}}^{\text{CH}_3}$ (cm^{-1})
H18SH	2850	2877	2918	2964
HCyH10SH	2850 (2858 ring)	-	2924 (2937 ring)	-
HCyH11SH	2851 (2857 ring)	-	2923 (2937 ring)	-
FCyH10SH	2849	-	2920	-
FCyH11SH	2850	-	2921	-

2.3.4. Contact Angle Measurements.

The interfacial properties of the investigated SAMs and their polymer counterparts (PE and PTFE) were probed using a variety of contacting liquids ranging from polar protic (water, W, $\gamma_{LV} = 72.0$ mN/m; formamide, FA, $\gamma_{LV} = 58.2$ mN/m; and methyl formamide, MF, $\gamma_{LV} = 38.0$ mN/m), to polar aprotic (dimethyl formamide, DMF, $\gamma_{LV} = 37.1$ mN/m; and acetonitrile, ACN $\gamma_{LV} = 29.3$ mN/m), and non-polar aprotic (squalane, SQ, $\gamma_{LV} = 28.9$ mN/m; and hexadecane, HD $\gamma_{LV} = 27.5$ mN/m) liquids.¹⁷²⁻¹⁷³ Table 2.4 lists the advancing contact angles (ACAs) and the hysteresis values (difference between advancing and receding contact angles) for all probe liquids employed on the **H18SH**, **HCyHnSH**, **FCyHnSH**, **PE**, and **PTFE** surfaces.

Figure 2.5 compares the ACA values obtained for all the liquids on the investigated SAMs and the two polymer surfaces. The wettability data of the **H18SH** SAMs, PE, and PTFE agree with previously reported values.^{122,151,169} Furthermore, the wettability data for these liquids on both the **FCyHnSH** and **HCyHnSH** series showed no clear evidence for an "odd-even" effect. Overall, the wettability data for all SAMs resemble those of the polymers they were designed to mimic. For example, the ACA of water on the **HCyHnSH** SAMs, 106-107°, was similar to the ACA of water on PE, 108°. Similarly, water exhibited comparable contact angle values on the **FCyHnSH** SAMs, 119-120°, as on the PTFE surface, 118°. Importantly, the PE surface swelled quickly upon contact with MF, DMF, ACN, SQ, and HD, indicating that these liquids intercalate into the PE surface, leading to reorganization of the polymer chains. To compare the ACAs of PE with those of the **HCyHnSH** SAMs, all contact angle data taken on the **PE** surfaces were collected within 5 seconds of coming into contact with the above-mentioned liquids. In contrast, we observed no significant changes in the contact angles on the **PTFE** as a function of time of contact with the liquids, which is consistent with previous wettability studies of **PTFE**.¹³⁷ Similarly, the

contact angles for all liquids on the **HCyHnSH** and **FCyHnSH** SAMs were constant over time, suggesting no surface reorganization.

Table 2.4. Advancing Contact Angles (θ_a , °) of the Investigated SAMs and Polymers Using Various Probe Liquids

	W	FA	MF	DMF	ACN	SQ	HD
H18SH	117 (5)	99 (7)	80 (7)	74 (6)	68 (8)	58 (8)	47 (7)
HCyH10SH	106 (6)	85 (7)	67 (8)	61 (6)	52 (7)	16 (-)	< 10 (-)
HCyH11SH	107 (6)	86 (7)	68 (7)	60 (4)	51 (7)	15 (-)	< 10 (-)
PE	108 (10)	85 (10)	58 (12)	51 (8)	48 (9)	20 (-)	< 10 (-)
FCyH10SH	120 (7)	103 (7)	82 (10)	73 (6)	61 (4)	64 (9)	57 (8)
FCyH11SH	119 (8)	104 (7)	80 (10)	72 (5)	63 (4)	66 (10)	59 (7)
PTFE	118 (14)	102 (22)	81 (15)	76 (12)	67 (12)	60 (21)	46 (23)

Entries marked (-) reflect receding contact angles $< 10^\circ$ (commonly defined as fully wettable). Values of hysteresis ($\theta_a - \theta_r$, °) are given in parentheses.

All of the surfaces examined showed an increasing trend in wettability (i.e., decrease in contact angle) as the surface tension of the liquid decreased, save for one exception involving acetonitrile and squalene on the **FCyHnSH** SAMs (vide infra). Water, with the highest surface tension ($\gamma_{LV} = 71.97$ mN/m), showed the highest contact angle on all the surfaces followed by formamide, methylformamide, dimethylformamide, acetonitrile, squalane, and hexadecane. As the intermolecular forces within the liquid decrease (i.e., hydrogen bonding and van der Waals forces), self-association of the contacting liquid also decreases, leading to increased interactions with the interface (i.e., a lower contact angle and thus a more wettable surface).¹⁷⁴ Accordingly, among the polar contacting liquids, water interacts the least with these surfaces due to its high surface tension ($\gamma_{LV} = 71.97$ mN/m) and the absence of hydrogen bonding with the surface and the

absence of oriented dipoles near the interface.^{147,152-153,157} Note that the ACA values of water on the fluorinated surfaces were higher than those on the hydrocarbon ones, which supports our earlier hypothesis that the size of the perfluorinated cyclohexyl ring would sufficiently screen and thereby mitigate any effects due to FC-HC dipole at the ring-alkyl chain junction.

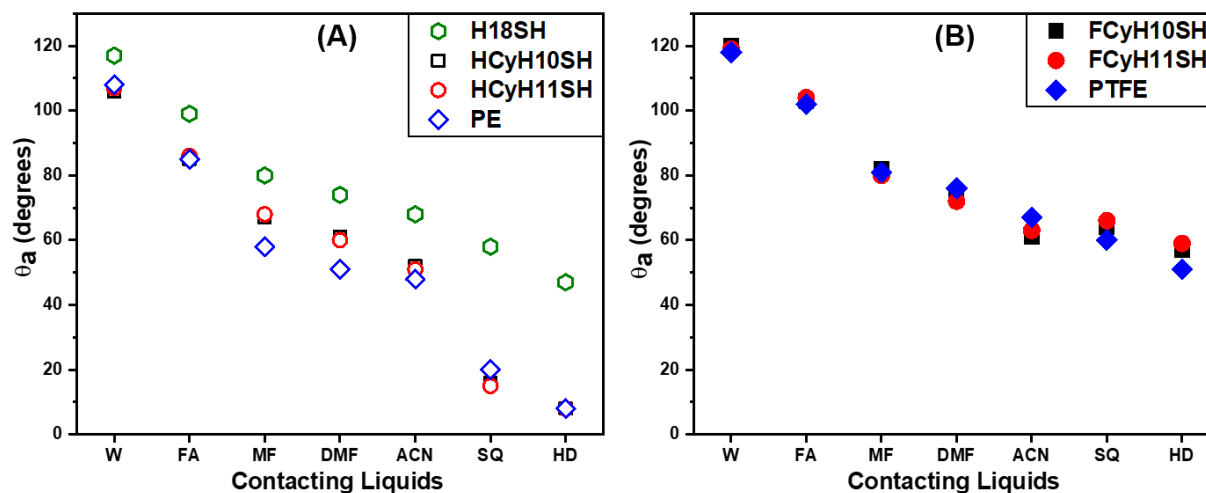


Figure 2.5. Comparison of the advancing contact angles of various probe liquids for: (A) the **HCyHnSH** SAMs and **PE**; (B) the **FCyHnSH** SAMs and **PTFE**. W = water; F = formamide; MF = methylformamide; DMF = dimethylformamide; ACN = acetonitrile; SQ = squalane; HD = hexadecane. HD fully wets the **HCyHnSH** SAMs and **PE**. The **H18SH** SAM is included as a reference. *Error bars that are not visible fall within the symbols.*

Both squalane and hexadecane are non-polar liquids with similar surface tensions (28.9 mN/m for squalane and 27.5 mN/m for hexadecane), which interact with all the investigated surfaces exclusively through dispersive (van der Waals) interactions. And although acetonitrile is polar, its surface tension (ACN $\gamma_{LV} = 29.3$ mN/m) is comparable to those of the nonpolar liquids. This rather small difference in liquid surface tension might be responsible for the minor discrepancy noted above (i.e., the **FCyHnSH** SAMs were less wettable by squalane than by acetonitrile). We note, however, that for the investigated PTFE sample, the wettability trends followed the expected trajectory.

Separately, the **HCyHnSH** SAMs and PE surfaces were more wettable by all contacting liquids than the reference **H18SH** SAM. The observed differences in the wettability are a result of the interfacial features of the films. In the **HCyHnSH** and **PE** surfaces there is an increase in atomic contact per unit area compared to the **H18SH** SAM.^{165,175} The chain termini in the **H18SH** SAM are separated by a distance of ~ 5.0 Å.¹⁵⁸ However, the distance between the CH₂ units of the cyclohexyl rings and the PE chain is the same as the length of a C-C bond, ~ 1.54 Å,¹⁷⁶ which can plausibly give rise to stronger vdW interactions between the interface and the nonpolar contacting liquids.^{165,175}

The wettability data presented in Figure 2.5 shows that the current set of SAMs offers a suitable model for evaluating the interfacial properties of the PE and PTFE polymers. Both pure PE and PTFE are semi-crystalline polymers at room temperature, where their crystalline regions are composed of planes of parallel linear chains.^{126,177} However, the sliding movement between the different planes and reorientation of the polymer chains make the direct analysis of these polymer interfaces a challenging task. Separately, the observed agreement between the wettability data of the **FCyHnSH** and **HCyHnSH** SAMs with their corresponding polymer films indicate that these surfaces have a similar density of interfacial atomic contacts. Furthermore, the hysteresis values, shown in Table 2.4, indicate that the investigated SAMs have lower hysteresis values than the polymer surfaces, which might be the result of surface roughness and surface reconstruction. We note that the investigated SAMs surfaces have lower surface roughness/heterogeneity compared to the two polymers, which is consistent with the absence of surface reconstruction in the SAM films.

2.4. Conclusions

Adsorbates for generating cyclohexyl-terminated SAMs (**HCyHnSH**) and perfluorocyclohexyl-terminated SAMs (**FCyHnSH**) were synthesized and used to form monolayers on gold that serve as interfacial polymer mimics on metal substrates. The monolayer films were characterized using ellipsometry, XPS, PM-IRRAS, and contact angle measurements. Analysis by XPS indicated that the **FCyHnSH** SAMs exhibited lower packing densities than their hydrocarbon analogs, and both types of SAMs exhibited lower packing densities than the **H18SH** films, which correlated with the steric bulk of the chain termini in these SAMs. The PM-IRRAS spectra showed that the chain backbones of both **FCyHnSH** and **HCyHnSH** SAMs were less conformationally ordered than normal hydrocarbon analogs. Furthermore, the **HCyHnSH** SAMs exhibited wettabilities similar to PE, while their fluorocarbon analogs exhibited wettabilities similar to **PTFE** for a wide range of contacting liquids with no evidence of surface reconstruction in the SAMs. Therefore, SAMs on gold derived from cyclohexyl-terminated thiols can thus serve as robust models to study the interfacial properties and reactivities of polymer surfaces.

Chapter 3: SAMs on Gold Derived from Adsorbates Having Cyclohexyl and Phenyl Tailgroups Mixed with their Phase-Incompatible Perfluorinated Analogs

3.1. Introduction

Incorporating fluorine atoms into the molecular structure of an adsorbate renders this class of molecules excellent candidates for nanocoatings, specifically in the form of fluorinated self-assembled monolayers (FSAMs), due to their highly hydrophobic and oleophobic nature.^{9,157} After decades of development, self-assembled monolayers (SAMs) have been widely employed for surface modification in various industrial fields, such as anti-corrosion in GaAs electronic devices,^{95,99,108} anti-fouling in biosensors,¹⁷⁸⁻¹⁷⁹ and anti-adhesion in microelectromechanical systems (MEMS).^{10-11,180} Modification of surfaces with SAMs, such as those derived from alkanethiols, with differing chemical species (i.e., a fully hydrocarbon alkanethiol and a fluorinated alkanethiol), have attracted the attention of scientist and engineers in order to tune interfacial properties. However, due to the phase-incompatibility of fluorinated and non-fluorinated adsorbates, discrepancies between the composition of the SAM and deposition solutions are often seen.¹⁸¹ Moreover, there are three major challenges that have been encountered in attempts to generate mixed, phase-incompatible SAMs: (1) preferential adsorption of one type of adsorbate over the other; (2) phase separation on the surface (i.e., the formation of molecular domains formed on the nanometer scale); and (3) changes to the composition of the surface over time due to adsorbate exchange.¹⁸²⁻¹⁸⁵ For example, a previous study of mixed SAMs on Au(111) derived from the mixture of hexadecane-1-thiol and heptafluorohexadecane-1-thiol, saw preferential adsorption of the fluorinated adsorbate due to its poor solubility and the hydrophobic

nature of the fluorinated adsorbate, facilitating its transition from the solution phase onto the gold surface.¹⁸⁶⁻¹⁸⁸

Previous literature has extensively examined the effect of combining incompatible functional groups, such as the mixed surface of methyl and hydroxymethyl groups,¹⁸² methyl and amino groups,¹⁸⁹ and methyl and oligo (ethylene glycol) groups.¹⁹⁰ However the number of studies exploring the effect of bulky functional groups is limited, especially for fluorinated groups.¹⁹¹⁻¹⁹² To study the effect of bulky perfluorinated tailgroups in mixed phase-incompatible SAMs, we investigated mixed SAMs generated from two classes of adsorbates on Au(111) bearing either a cyclohexyl or phenyl tailgroup of the form $C_6H_{11}(CH_2)_{11}SH$ (**HCyH11SH**) and $C_6H_5(CH_2)_{12}SH$ (**PhH12SH**), respectively). The adsorbates were mixed with their perfluorinated analogs, $C_6F_{11}(CH_2)_{11}SH$ (**FCyH11SH**) and $C_6F_5CF_2(CH_2)_{11}SH$ (**FPhFH11SH**), respectively, to generate the mixed surfaces on gold; the molecular structures of the adsorbates are shown in Figure 3.1. The adsorbates terminated with an aromatic moiety were included in this study in order to offer insight into the structure-property relationship of mixed SAMs with different perfluorinated tailgroups. All of the adsorbates in this study have bulky tailgroups compared to simple alkyl and fluoroalkyl chains, but the phenyl and perfluorophenyl tailgroups are less sterically bulky than the cyclohexane and perfluorocyclohexane rings because of the planar structure of phenyl ring. Furthermore, π -interactions between phenyl rings, as well as π -interactions between phenyl and perfluorophenyl rings, might reduce the phase separation of our mixed SAMs.¹⁹³⁻¹⁹⁵

The two series of mixed monolayers were characterized using ellipsometry, X-ray photoelectron spectroscopy (XPS), polarization-modulation infrared reflection-absorption spectroscopy (PM-IRRAS), and contact angle measurements.

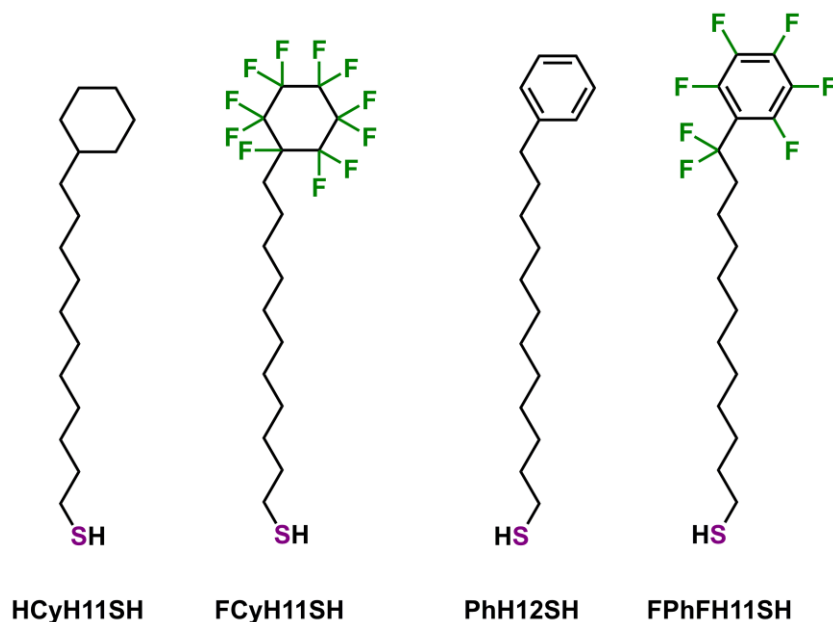


Figure 3.1. Molecular structures of the adsorbates used to generate mixed SAMs on gold.

3.2. Experimental Procedures

3.2.1. Materials and Methods

In this study, the adsorbate 11-cyclohexylundecane-1-thiol (**HCyH11SH**),⁹ 11-(perfluorocyclohexyl)undecane-1-thiol (**FCyH11SH**),⁹ and 12-phenyldodecanethiol (**PhH12SH**)¹⁹⁵ was prepared following the synthetic route outlined in the indicated literature references.

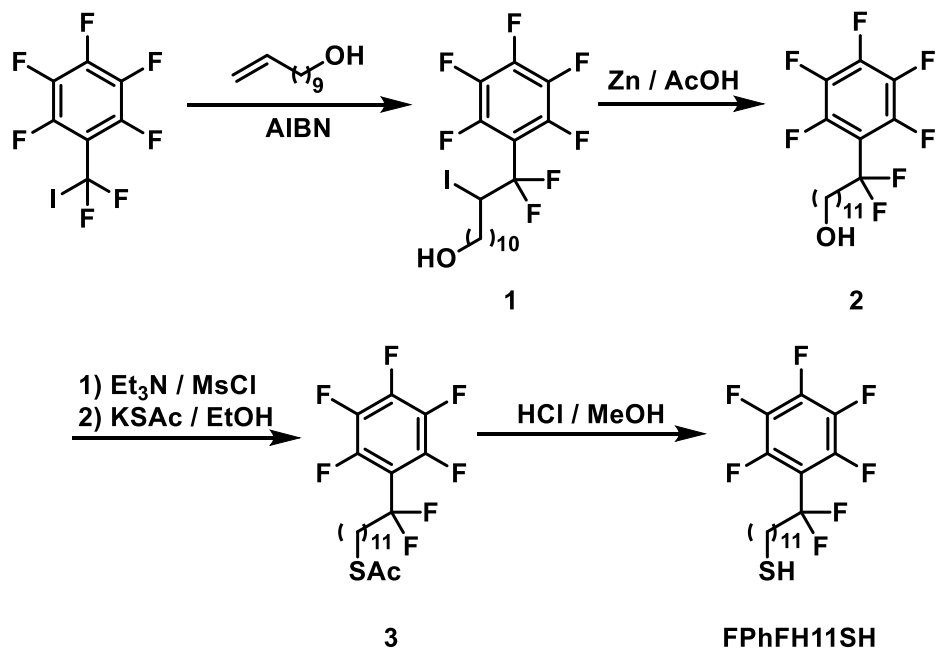
Tetrahydrofuran (THF – Avantor Performance Materials), dichloromethane (DCM – Macron Chemicals), and diethyl ether (Et₂O – J. T. Baker) were dried by distilling over calcium hydride (Sigma Aldrich). Hexanes and acetone (both from Avantor Performance Materials), ethyl acetate (Sigma Aldrich), and ethanol (EtOH – Aaper Alcohol and Chemical Co.) were either used as received or degassed by purging with nitrogen. Methanesulfonyl chloride (MsCl), 2,2'-azobis(2-methylpropionitrile) (AIBN), lithium aluminum hydride (LiAlH₄), borane tetrahydrofuran complex (BH₃-THF), triethylamine (Et₃N), *p*-toluenesulfonic acid (PTSA), and

3,4-dihydro-2H-pyran (DHP) were all purchased from Sigma Aldrich and used as received. 1-(Difluoroiodomethyl)-2,3,4,5,6-pentafluorobenzene (Synquest Labs), 10-undecen-1-ol (Oakwood Chemical), and potassium thioacetate (KSAc – Sigma Aldrich) were used as received. Hydrochloric acid (HCl, 37% – Macron Fine Chemicals), zinc dust (Fischer), sodium iodide (KI – EMD Chemicals), glacial acetic acid (AcOH) and ammonium chloride (NH₄Cl – both from Mallinckrodt Chemicals) were all used as received. Chloroform-*d* was purchased from Cambridge Isotope Laboratories and used to collect all NMR spectra. Silica gel for column chromatography was obtained from Sorbent Technologies.

3.2.2. Adsorbate Synthesis.

12,12-Difluoro-12-(perfluorophenyl)dodecane-1-thiol (**FPHFH11SH**) was prepared following the synthetic route outlined below in Scheme 3.1 below.

Scheme 3.1. Preparation of 12,12-Difluoro-12-(perfluorophenyl)dodecane-1-thiol (**FPHFH11SH**).



12,12-Difluoro-10-iodo-12-(perfluorophenyl)dodecan-1-ol (1) 1-(difluoroiodomethyl)-2,3,4,5,6-pentafluorobenzene (5.03 g; 14.6 mmol), AIBN (0.239 g; 1.46 mmol), and 10-undecen-1-ol (2.24 g; 13.2 mmol) were added to a 100-mL pear-shaped Schlenk flask. The system was degassed using three cycles of a standard freeze-pump-thaw procedure. After warming to rt, the reaction mixture was heated to 75 °C for 8 h. After cooling the reaction to rt, the crude mixture was purified by column chromatography over silica gel using hexanes/ethyl acetate (80/20) as the eluent system to give **2** as clear oil in 44% yield. ¹H NMR (500 MHz, CDCl₃): δ 4.06 (m, 1H), 3.66 (t, *J* = 6.41 Hz, 2H), 2.74–3.00 (m, 2H), 2.27–2.32 (m, 2H), 1.84–2.09 (m, 4H), δ 1.72 (m, 1H), 1.25–1.38 (m, 10H).

12,12-Difluoro-12-(perfluorophenyl)dodecan-1-ol (2) **2** (6.32 g; 12.3 mmol) and zinc dust (12.0 g; 185 mmol) were added to 100 mL of glacial acetic acid at rt. The reaction mixture was stirred for 40 h in the dark and then filtered through a bed of Celite. The Celite pad was then washed with 200 mL of Et₂O. The filtrate was washed with water (3 × 100 mL), saturated aqueous NaHCO₃ (1 × 100 mL), and brine (1 × 100 mL). The organic layer was then dried over MgSO₄, and the solvent was removed by rotary evaporation. The crude alcohol was purified by column chromatography over silica gel using hexanes/ethyl acetate (80/20) as the eluent system to give **3** in 60% yield. ¹H NMR (500 MHz, CDCl₃): δ 3.65 (t, *J* = 6.40 Hz, 2H), 2.17–2.25 (m, 2H), 1.58–1.62 (q, *J* = 7.56 Hz, 2H), 1.44–1.49 (m, 2H), 1.32–1.38 (m, 4H), 1.26–1.38 (m, 11H).

S-(12,12-Difluoro-12-(perfluorophenyl)dodecyl) ethanethioate (3) Alcohol **2** (4.57 g; 17.5 mmol) was dissolved in anhydrous THF under nitrogen, and the solution was cooled to 0 °C in an ice bath. Triethylamine (7.2 mL g; 52.5 mmol) was added slowly to the resulting mixture and stirred for 30 min at 0 °C. After that, MsCl (4.1 mL; 52.5 mmol) was added dropwise. The reaction was warmed to rt, stirred for 6 h, and subsequently quenched with 200 mL of water. The

product was extracted with Et₂O (3 × 100 mL), and the combined organic phases were washed with 1M HCl (1 × 100 mL), water (1 × 100 mL), and brine (1 × 100 mL). The organic layer was dried over anhydrous MgSO₄, followed by removal of the solvent by rotary evaporation. The crude mesylate was dried under high vacuum overnight and dissolved in 100 mL of absolute ethanol. A portion of KSAc (3.97 g; 34.8 mmol) was then added to the solution, and the mixture was refluxed for 6 h. After cooling the reaction to rt, the solvent was removed by rotary evaporation and 200 mL Et₂O was added to the mixture. The organic phase was washed with water (1 × 100 mL) and brine (1 × 100 mL), and then dried over MgSO₄. The solvent was removed by rotary evaporation. The crude product was purified by silica gel chromatography using hexanes as the eluent to give **3** as yellow oil in 96% yield. ¹H NMR (500 MHz, CDCl₃): δ 2.85 (t, *J* = 7.56 Hz, 2H), 2.32 (s, 3H), 2.17–2.25 (m, 2H), 1.58–1.62 (m, 2H), 1.44–1.49 (m, 2H), 1.32–1.38 (m, 4H), 1.26–1.38 (m, 10H).

12,12-Difluoro-12-(perfluorophenyl)dodecane-1-thiol (FPHFH11SH) The thioacetate **3** (0.60 g; 15.0 mmol) was dissolved in 100 mL of absolute ethanol. To the solution, 0.40 mL HCl (37%) was added, and the stirred mixture was heated under reflux at 80 °C for 12 h. The reaction mixture was evaporated to dryness by rotary evaporation. The crude thiol was purified by column chromatography on silica gel (hexanes) to give **FPHFH11SH** as light-yellow oil in 78% yield. ¹H NMR (500 MHz, CDCl₃): δ 2.50 (t, *J* = 7.56 Hz, 2H), 2.17–2.25 (m, 2H), 1.58–1.62 (m, 2H), 1.44–1.49 (m, 2H), 1.32–1.38 (m, 4H), 1.26–1.38 (m, 11H). ¹³C NMR (151 MHz, CDCl₃): δ 145.5, 143.7, 142.9, 141.2, 138.8, 137.2, 120.9, 34.1, 29.8, 29.5, 29.4, 29.3, 29.1, 29.0, 28.6, 28.4, 24.7, 22.1. ¹⁹F NMR (376 MHz, CDCl₃): δ -90.1 (s, 2F), -120.2 (s, 2F), -150.8 (s, 1F), -160.5 (s, 2F) HR-GC-MS, *m/z*: 404.1418 (C₁₈H₂₂F₇SH⁺), 403.1325 (M⁺-H).

3.2.3. Preparation and Characterization of the SAMs

Gold shot (99.999%) was purchased from Kamis Incorporated. Chromium rods (99.9%) were purchased from R. D. Mathis Company, and polished single-crystal Si(100) wafers were purchased from Silicon Wafer Enterprises. The gold substrates were prepared by thermal evaporation onto Si(100) wafers under vacuum at a pressure $\leq 6 \times 10^{-5}$ torr. Chromium (100 Å) was initially deposited at rate of 0.5 Å / s to aid the adhesion of the Au layer, then 1000 Å of Au was deposited at rate of 0.5 Å / s. Immediately after vapor deposition, the substrates were cleaned with ultra-pure nitrogen gas. Solutions of the 1 mM thiols in different ratios in absolute ethanol (previously degassed) were prepared in 40 mL vials. Two cut Au slides (2 cm \times 1 cm) were then immersed into each of the thiol solutions and allowed to equilibrate for 48 h at rt in the dark. Before characterization, all films were rinsed with THF followed by absolute ethanol and dried with ultra-pure nitrogen flow.

Thickness measurements were collected on an alpha-SE ellipsometer from J.A.Woollam with an incident angle set to 70°. The refractive index was set to 1.45, which is consistent with the value used in the previous literature for organic monolayers. The thickness value of one sample were derived from the averages of 6 measurements (3 measurements per slide).

X-Ray photoelectron spectroscopy (XPS) measurements were performed using a PHI 5700 X-Ray photoelectron spectrometer with a monochromatic Al K α X-ray source ($h\nu = 1486.7$ eV) incident at 90° relative to the axis of the hemispherical energy analyzer. The takeoff angle from the surface was set at 45° with a pass energy of 23.5 eV. The Au 4f_{7/2} peak at 84.0 eV was used as a reference peak, with each spectrum calibrated to the reference.¹⁹⁶ A standard SAM derived from octadecanethiol (ODT) was also characterized and used as a reference.

PM-IRRAS spectra were collected using a Nicolet Nexus 670 Fourier transform spectrometer equipped with a mercury-cadmium-telluride (MCT) detector and a Hinds Instrument PEM-90 photoelastic modulator. The collected spectra were from surfaces mounted at an incident angle of 80° for the p-polarized light with respect to the surface normal. For each sample, we collected 1024 scans at a resolution of 2 cm⁻¹.

Contact angle data were obtained using a compact high-resolution CMOS camera (DCC1645C) and 12X zoom lens (MVL12X12Z) working with a Matrix Technologies micro-Electrapette 25 dispensing liquids from a disposable pipette tip. Contacting liquids were dispensed at a speed of 1 μL/s to obtain advancing contact angles (θ_a). The specific method used to collect the contact angle data was the dynamic sessile drop procedure (where the liquid dispensing pipette remains in contact with the drop), with images taken during the dispensing of the contacting liquid, maintaining the pipette tip centered on the drop. The reported contact angle data represent the average of at least 12 measurements from 3 different locations for each SAM-coated slide. Adobe® Photoshop® was used to measure the angles on each side of the dispensed droplets. The following two contacting liquids were used: water (Millipore water with a resistivity of 18.2 MΩ·cm) and diiodomethane (CH₂I₂ – Sigma-Aldrich).

3.3. Results and Discussion

The nomenclature of the mixed SAMs is defined according to the mole fraction of the fluorinated adsorbate in solution. For example, the sample **FCyH11SH** (0.00) represents a SAM composed of 100% **HCyH11SH**, while **FPhFH11SH** (0.00) represents a SAM composed of 100% **PhH12SH**. A detailed overview of the composition of the SAMs are given in Table 3.1.

Table 3.1. Adsorbate Mole Fraction in Solution Used to Generate the Mixed SAMs

Mole Fraction of Fluorinated Adsorbate in Solution	Sample			
	FCyH11SH	HCyH11SH	FPhFH11SH	PhH12SH
0.00	0.00	1.00	0.00	1.00
0.25	0.25	0.75	0.25	0.75
0.50	0.50	0.50	0.50	0.50
0.75	0.75	0.25	0.75	0.25
1.00	1.00	0.00	1.00	0.00

3.3.1. Ellipsometric Thickness Measurements.

After the mixed SAMs were deposited on Au(111) for 48 h, the average thicknesses of the thin films were measured by ellipsometry. Table 3.2 lists the average ellipsometric thickness of the mixed SAMs on Au(111). For **HCyH11SH** / **FCyH11SH** mixed SAMs, the single component SAMs generated from the adsorbates with the perfluorinated tailgroups exhibited lower thicknesses than their hydrocarbon analogs: 12 Å for the **FCyH11SH** (1.00) SAM vs 14 Å for **FCyH11SH** (0.00) (e.g. **HCyH11SH**), respectively. The thinner thicknesses of the FSAMs was attributed to the lower packing densities, due to the larger van der Waals (vdW) radius of the fluorine atoms (1.47 Å) compared to hydrogen atoms (1.20 Å)¹⁵⁶ in addition to the sterically bulkier perfluorinated tailgroups compared to the hydrocarbon tailgroups. Moreover, impacted by the bulkier tailgroups of cyclohexane compared to the planar phenyl ring, the **HCyH11SH** / **FCyH11SH** mixed SAMs show lower thickness than the **PhH12SH** / **FPhFH11SH** mixed SAMs.

In the mixed SAMs, introduction of the fluorinated adsorbate into the deposition solution led to a decrease in the film thickness. However, based on the film thickness data alone, it is difficult to determine the phase behavior on the surface. Further insight into the composition of the films will be discussed in detail in the XPS section.

Table 3.2. Ellipsometric Thicknesses of the Investigated Mixed SAMs

Sample	Thickness (Å)	Sample	Thickness (Å)
FCyH11SH (0.00)	14 ± 1	FPhFH11SH (0.00)	18 ± 1
FCyH11SH (0.25)	14 ± 1	FPhFH11SH (0.25)	18 ± 1
FCyH11SH (0.50)	14 ± 1	FPhFH11SH (0.50)	18 ± 1
FCyH11SH (0.75)	14 ± 1	FPhFH11SH (0.75)	17 ± 1
FCyH11SH (1.00)	12 ± 1	FPhFH11SH (1.00)	17 ± 1

3.3.2. XPS Composition Analysis and Packing of the SAMs.

In the analysis of organic thin films, XPS is a commonly used technique for determining the surface composition and the relative packing densities of thiol-based SAMs.^{161,197-198} Figure 3.2 shows the XPS spectra of the S 2p, C 1s, and F 1s binding energy regions of the mixed SAMs derived from **HCyH11SH** and **FCyH11SH**. The S 2p spectra gives insight into the chemical nature of the sulfur species on the surface. Bound thiolates exhibit a doublet attributed to the S 2p_{3/2} photoelectron at 163.0 eV and the S 2p_{1/2} photoelectron at 162.0 eV in a 1 to 2 ratio for the 2p_{1/2} to 2p_{3/2} photoelectrons, which appeared for all the SAMs in the study.^{37,163} Moreover, the absence of peaks at ~164 eV or ~166 eV suggests no unbound thiol or highly oxidized sulfur species, respectively, in all the investigated SAMs.¹⁶³ For the **HCyH11SH** and **FCyH11SH** mixed SAMs series the S 2p spectra exhibits the characteristic doublet representative of a bound thiolate at ~163.0 eV and ~162.0 eV in every sample, suggesting that both alkanethiols chemically bind to the Au(111) surface.

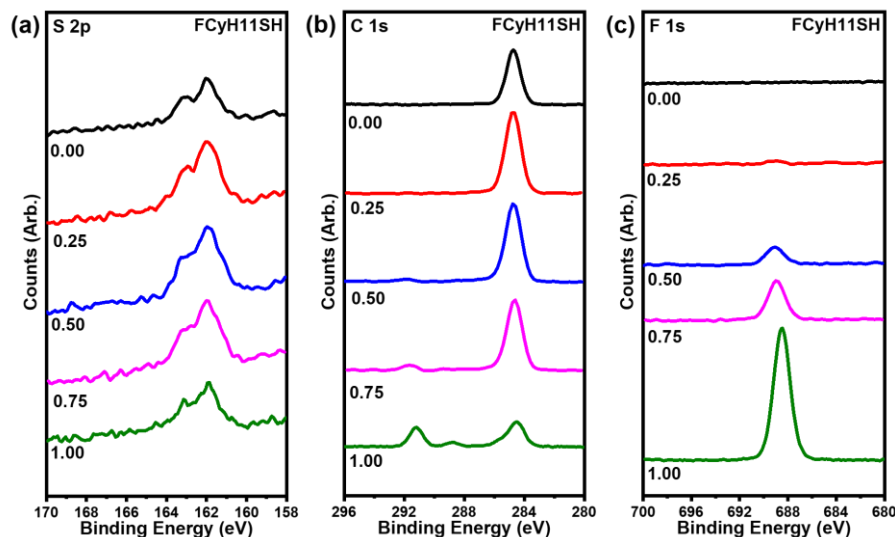


Figure 3.2. XPS spectra of the (a) S 2p, (b) C 1s, and (c) F 1s binding regions of the mixed SAMs derived from **HCyH11SH** and **FCyH11SH**.

In Figure 3.2a, the C 1s spectra of the **HCyH11SH** SAMs show only one peak at 284.7 eV, which indicates the carbons of the cyclohexyl ring, the tertiary carbon, and the carbons of the alkyl chain have a similar binding energy. The C 1s spectra of the **FCyH11SH** (1.00) SAM, shown in Figure 3.2b, exhibits two large peaks at 291.1 eV and 284.5 eV and a smaller peak at ~288.6 eV, which are attributed to the CF_2 of the perfluorinated cyclohexane ring, CH_2 of the hydrocarbon chain, and CF connected to the alkyl chain, respectively.⁹ The fluorine atoms in the perfluorocyclohexane-terminated adsorbate produced a peak in the F 1s region at 688.4 eV, shown in Figure 3.2c. Apparent in the spectra, a gradual increase in the intensity of the peak is observed in the samples as the concentration of the fluorinated adsorbate increases in the deposition solution.

The S 2p spectra of **PhH12SH** / **FPhFH11SH** mixed SAMs in Figure 3.3a exhibit a characteristic doublet attributed to bound thiolate at ~162.0 eV and ~163.0 eV. For the **PhH12SH** SAM (e.g., **FPhFH11SH** (0.00)), a single peak at 284.7 eV in the C 1s spectrum was observed in Figure 3.3b. On the other hand, the C 1s spectrum of the **FPhFH11SH** SAM (e.g., **FPhFH11SH**

(1.00)) exhibited three peaks at 290.5 eV, 288.3 eV, and 284.6 eV, which were attributed to electrons arising from the CF₂, CF of the perfluorophenyl ring, and CH₂ of the hydrocarbon chain, respectively. Similar to the **FCyH11SH** SAM, the F1s region shown in Figure 3.3c shows a peak at 688.4 eV which gradually increases as the concentration of the fluorinated adsorbate increases in the deposition solution.

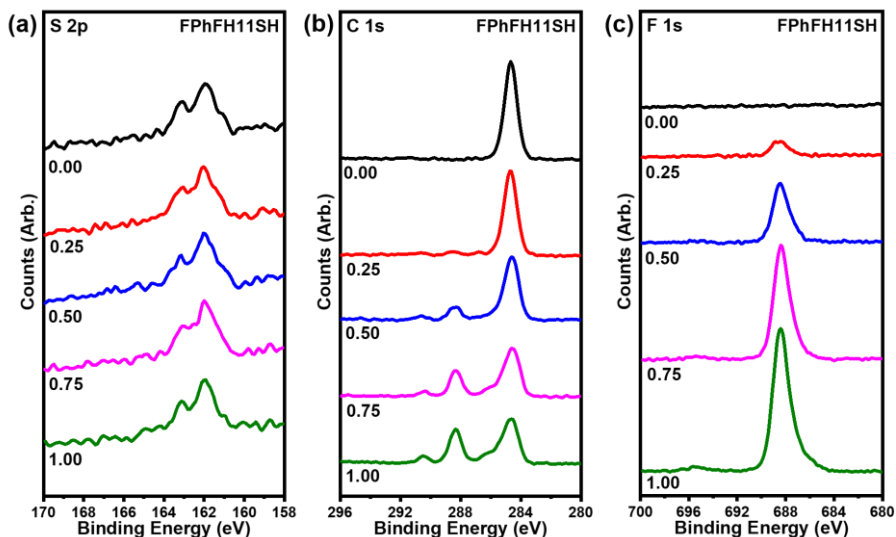


Figure 3.3. XPS spectra of the (a) S 2p, (b) C 1s, and (c) F 1s binding regions of the mixed SAMs derived from **PhH12SH** and **FPhFH11SH**.

In addition, the relative packing density was calculated by monitoring the integrated intensity of the S 2p and Au 4f signals, specifically the S / Au ratios.¹⁶⁵ In our analysis, an octadecanethiol (ODT) SAM on Au was used as the reference, in which all binding sites on the Au surface are occupied and the packing density is 100%. Moreover, it is important to note that the electron attenuation lengths of hydrocarbons and fluorocarbons are indistinguishable, and the packing densities of the investigated thin films on Au can be calculated in the same manner.¹⁶⁶ Table 3.3 shows the relative packing densities of the investigated mixed SAMs. For the **HCyH11SH** / **FCyH11SH** mixed SAMs, the packing densities of the mixed SAMs decreased as

the mole fraction of the fluorinated adsorbate was increased in solution, which is not significant in the **PhH12SH / FPhFH11SH** mixed SAMs. Overall, the **PhH12SH / FPhFH11SH** mixed SAMs show higher packing densities than the **HCyH11SH / FCyH11SH** mixed SAMs, likely due to the different size of the chain termini. Additionally, in 2016 Lee and coworkers introduced bidentate adsorbates that exploits the "chelate effect" to generate homogeneously mixed monolayers on Au(111).¹⁸⁶ However, impacted by the large footprint of the bidentate head group, the packing densities (i.e., number of molecules per unit area) of the bidentate SAMs suffer a 40% reduction compared to their monodentate analogs.¹⁹⁷ In our case, by using monodentate adsorbates instead of bidentate, the relative packing of all the investigated mixed SAMs remain 66% and above. Especially for the **PhH12SH / FPhFH11SH** mixed SAMs in different ratios, they all reach 82% and above in packing densities, which provides densely packed films for homogeneously mixed surfaces

Table 3.3. Relative Packing Densities (%)^a of the Mixed SAMs as Determined by XPS

Mole fraction of FSAM in solution	FCyH11SH	FPhFH11SH
0.00	74 ± 5	88 ± 5
0.25	72 ± 5	83 ± 5
0.50	71 ± 5	87 ± 6
0.75	71 ± 5	88 ± 6
1.00	66 ± 5	82 ± 6

^aTo compare the relative packing densities, the S/Au ratios of the investigated SAMs were compared to the reference octadecanethiol (ODT) SAM.

To determine the composition of the mixed SAMs, the fluorocarbon (specifically the CF₂) and fluorine signals were used to evaluate the relative concentration of the fluorinated adsorbate on the surface of the mixed SAMs. For the **HCyH11SH / FCyH11SH** series, the relative ratios of the integrated intensity (peak area) of the CF₂ / Au and F / Au were calculated and shown in

Figure 3.4. It should be noted that the **FCyH11SH** (1.00) SAM was used as a reference and set to a ratio of 1.00. Figure 3.4a shows that the CF_2 / Au ratios from **FCyH11SH** (0.25), **FCyH11SH** (0.50), and **FCyH11SH** (0.75) only reached 0.02, 0.11, and 0.21, respectively. Similarly, the F / Au ratios, Figure 3.4b, for **FCyH11SH** (0.25), **FCyH11SH** (0.50), and **FCyH11SH** (0.75) were 0.02, 0.11 and 0.21, respectively. The results indicate that these films were mainly composed of **HCyH11SH** adsorbates with a small amount of **FCyH11SH**. Interestingly, our data shows significant preferential adsorption of the hydrocarbon adsorbate, **HCyH11SH**, over the fluorinated adsorbate, **FCyH11SH**, compared to the aforementioned alkanethiol system where the opposite trend is observed.¹⁸⁶ The observed preferential adsorption of the hydrocarbon adsorbate over the fluorinated component in the **HCyH11SH** / **FCyH11SH** series suggest that there are other factors at play other than solubility of the adsorbate alone. A previous study from Yu et al. stated that both **HCyH11SH** and **FCyH11SH** SAMs exhibit low packing densities compared to normal alkanethiols due to their bulky termini.⁹ Additionally, the SAM generated from **FCyH11SH** was found to be more rigid and less densely packed than its hydrocarbon analog, impacted by the larger van der Waals (vdW) volume of the fluorine atoms.^{9,156} Therefore, despite the difference in solubility, the large and rigid chain termini of the **FCyH11SH** adsorbate likely hinders the its adsorption onto the surface. Another plausible reason for the observed preferential adsorption of the **HCyH11SH** adsorbate over **FCyH11SH** is rapid exchange between the **FCyH11SH** on the surface and the thermodynamically favored **HCyH11SH** in the solution phase.¹⁹⁹

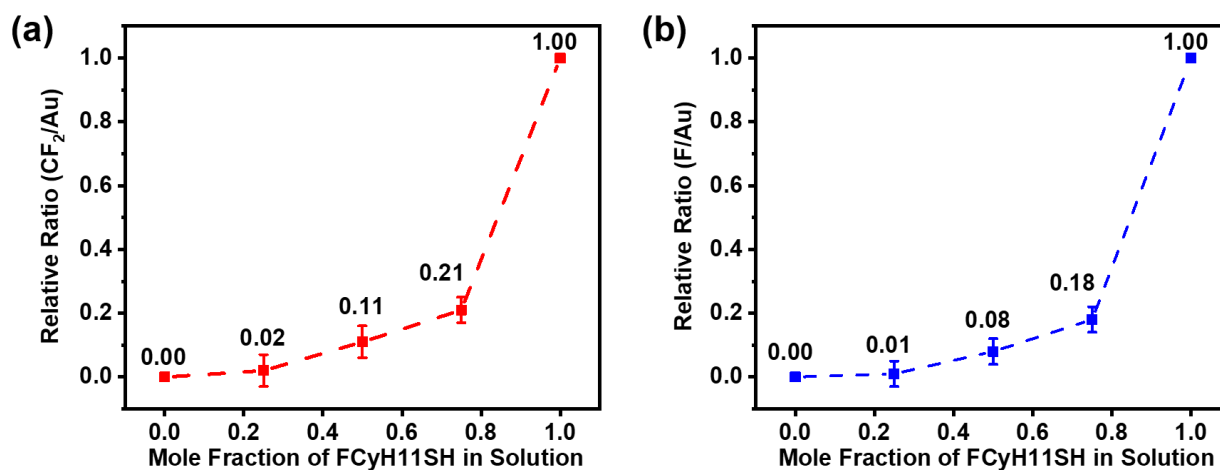


Figure 3.4. (a) CF₂ / Au ratio and (b) F/Au ratio of the mixed SAMs derived from **HCyH11SH** and **FCyH11SH**.

A similar approach was taken in the analysis of the **PhH12SH** / **FPhFH11SH**, where the relative ratios of CF / Au and F / Au from the XPS data were used to calculate the surface composition of the mixed SAMs; the CF from the aromatic ring at 288.3 eV was used in the analysis. The data in Figure 3.5a shows the CF / Au ratios of **FPhFH11SH** (0.25), **FPhFH11SH** (0.50), and **FPhFH11SH** (0.75) at 0.08, 0.36, and 0.72, respectively. Following the same trend, the F / Au ratios in Figure 3.5b show **FPhFH11SH** (0.25), **FPhFH11SH** (0.50), and **FPhFH11SH** (0.75) having ratios of 0.10, 0.37, and 0.72, respectively. The ratios of the **FPhFH11SH** (0.25) and **FPhFH11SH** (0.50) SAM indicate that the mole fraction of the **FPhFH11SH** adsorbate on the surface is lower than the mole fraction in solution with a slight preferential adsorption of the **PhH12SH** adsorbate, likely due to the difference in the steric bulk of the tailgroups. However, in the case of the **FPhFH11SH** (0.75) SAM, the mole fraction of adsorbate on the surface was the same as the mole fraction in solution, within error. Regardless of the lower surface mole ratios of the former mixed SAMs, there is a linear trend in the data suggesting that the **PhH12SH** and **FPhFH11SH** adsorbates adsorb onto the surface with similar tendencies.

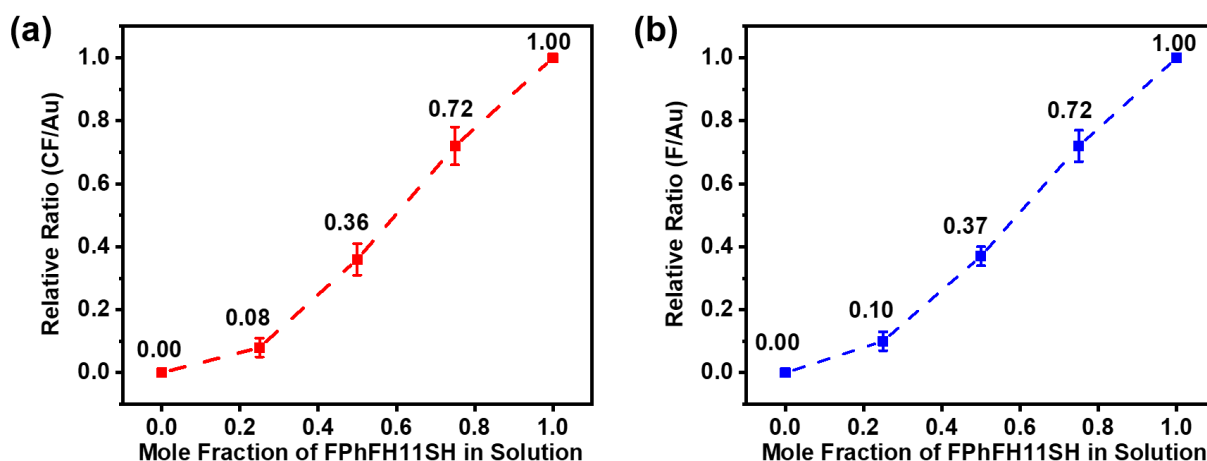


Figure 3.5. (a) CF/Au ratio and (b) F/Au ratio of the mixed SAMs derived from **PhH12SH** and **FPhFH11SH**.

The data suggests that there are two factors that may contribute to the observed phenomena: the solubility of the adsorbate in the deposition solution and molecular interactions between the tail groups. Previous study shows in the case of the mixed SAMs derived from hexadecane-1-thiol and heptadecafluorohexadecane-1-thiol, poor solubility of the fluorinated adsorbate is the key factor that contribute to preferential adsorption of it over its hydrocarbon analog.¹⁸⁶⁻¹⁸⁸ In the case of the **HCyH11SH** / **FCyH11H** mixed SAMs, although it is also noticeable that **FCyH11SH** is harder to dissolve in ethanol than **HCyH11SH**, the steric bulkiness of the **FCyH11SH** adsorbate is likely a key factor that leads to significant preferential adsorption of the less bulky hydrocarbon adsorbate. The unfavorable dispersive interactions between the fluorocarbons and hydrocarbons in the tailgroups of the adsorbates are likely an additional factor leading to the displacement of the fluorinated adsorbate from the surface. In the **PhH12SH** / **FPhFH11SH** mixed SAMs, the planar structure of the phenyl moieties coupled with π - π interactions likely leads to a film that is closely representative to the deposition solution.^{194,200} This is evidenced in the relatively higher packing densities compared to the **HCyH11SH** / **FCyH11SH** mixed SAMs. The less bulky tailgroups

compared to cyclohexane ring, and the interactions between the termini lead to homogeneously mixed SAMs derived from **PhH12SH** / **FPhFH11SH**. In addition, thanks to the special dielectric property of π system, phenyl-terminated SAMs have been applied on field-effect transistors (FETs) to tune the surface potentials and improve their performance.²⁰¹⁻²⁰² By using our **PhH12SH** / **FPhFH11SH** mixed SAMs system, it allows researchers to control the surface composition of mixed SAMs linearly.

3.3.3. Assessment of Chain Conformational Order Using PM-IRRAS.

PM-IRRAS is a surface-IR spectroscopy method that can be used to probe the relative chain conformational order of SAMs.¹⁶⁸ For well-ordered alkanethiol monolayers in which the hydrocarbon chains adopt all-trans extended crystalline conformations, such as the **ODT** SAM shown in Figure 3.6, the methylene antisymmetric stretching band ($\nu_{\text{as}}^{\text{CH}_2}$) is located at 2918 cm^{-1} .¹⁶⁹ On the other hand, disordered SAMs exhibit a blue shift in the $\nu_{\text{as}}^{\text{CH}_2}$ peak position.¹⁷⁰ Figure 3.6 shows the PM-IRRAS spectra of the mixed SAMs derived from the **HCyH11SH** / **FCyH11SH** and the **PhH12SH** / **FPhFH11SH** mixed SAMs in the C–H stretching region. All of the SAMs in the **HCyH11SH** / **FCyH11SH** series exhibit their $\nu_{\text{as}}^{\text{CH}_2}$ peak at $2923 \pm 1 \text{ cm}^{-1}$ with the single component SAMs in agreement with a previously published report.⁹ We note that the broadening of the $\nu_{\text{as}}^{\text{CH}_2}$ and $\nu_{\text{s}}^{\text{CH}_2}$ peaks is due to an overlap between the peaks of the alkyl chain and the cyclohexane ring, which are observed in all of the spectra except for **FCyH11SH** (1.00).⁹ For the **PhH12SH** / **FPhFH11SH** series, the $\nu_{\text{as}}^{\text{CH}_2}$ stretching band was observed at 2918 cm^{-1} to 2919 cm^{-1} , which is consistent with the $\nu_{\text{as}}^{\text{CH}_2}$ position observed in a previous report.¹⁹⁵

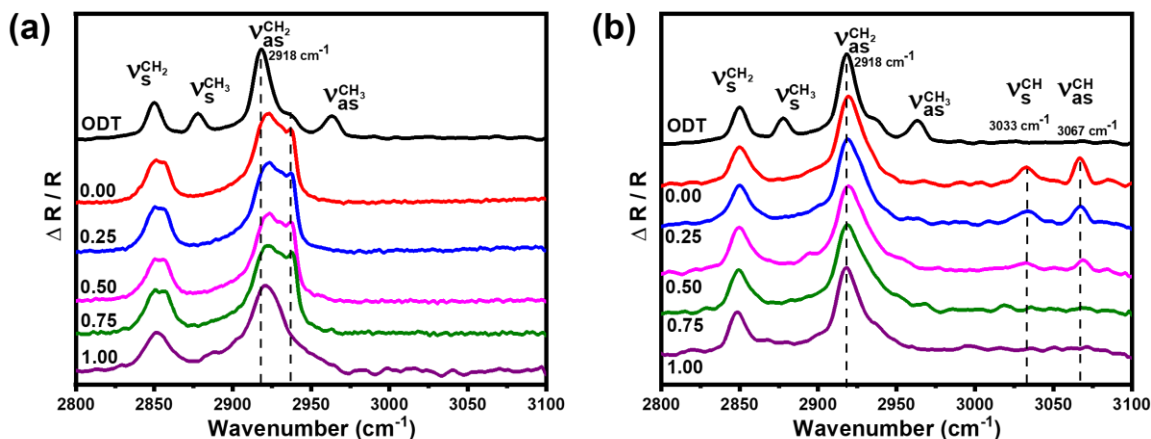


Figure 3.6. PM-IRRAS spectra of the mixed SAMs derived from (a) **HCyH11SH / FCyH11SH** and (b) **PhH12SH / FPhFH11SH**.

The PM-IRRAS spectra can also be used to obtain insight into the mixing of the adsorbates on the surface by monitoring peaks unique to one of the adsorbates. For the **HCyH11SH / FCyH11SH** series, the shoulder peak at 2937 cm^{-1} which is unique to the cyclohexane ring was used to monitor changes in the spectra. Conversely, for the **PhH12SH / FPhFH11SH** series, the peaks at 3033 cm^{-1} and 3037 cm^{-1} , which arise from the phenyl ring, were used. Apparent from the data, all of the mixed SAMs in the **HCyH11SH / FCyH11SH** series, with the exception of **FCyH11SH** (1.00), exhibit C-H stretches from the cyclohexane ring, indicating that the surface is predominately composed of the **HCyH11SH** adsorbate, in accordance with the XPS data. On the contrary, in the **PhH12SH / FPhFH11SH** series, there is a gradual decrease in the intensity of the aromatic C-H stretches in the spectra as the concentration of the fluorinated adsorbate is increased in the deposition solution. The gradual decrease observed in the spectra is indicative of surface composed of both components, in agreement with the XPS data.

3.3.4 Contact Angle Measurements.

The interfacial properties of the two mixed SAMs were characterized using contact angle measurements. The advancing contact angles (θ_a) of the mixed SAMs using water ($\gamma_{LV} = 72.0$ mN/m) and diiodomethane ($\gamma_{LV} = 50.0$ mN/m) as the contacting liquids.¹⁷² The surface energies of the mixed SAMs were also calculated using the Owens-Wendt method, which is commonly used in calculating the surface energies of organic thin films.²⁰³⁻²⁰⁶ Figure 3.7 shows the advancing contact angles and surface energies of the mixed SAMs derived from the **HCyH11SH / FCyH11SH** series. Due to the hydrophobic and oleophobic nature of the fluorine atom, the fluorinated SAM, **FCyH11SH** (1.00), had higher water and diiodomethane contact angles, (117° and 80° , respectively) than its hydrocarbon analog (106° and 52° , respectively), which is consistent with previous research.⁹ The water and diiodomethane contact angles of the mixed SAMs remain relatively the same, with the exception of the **FCyH11SH** (0.75) and **FCyH11SH** (1.00) where a significant increase in the contact angles are observed. We note that diiodomethane is more sensitive towards the change of surface composition, because the relatively low surface tension of diiodomethane makes it easier to intercalate into the films. The surface energy of the mixed **HCyH11SH / FCyH11SH** show a consistent trend from 34 mJ/m² to 28 mJ/m², within error, on the **FCyH11SH** (0.00), **FCyH11SH** (0.25), **FCyH11SH** (0.75), and **FCyH11SH** (0.75) SAMs. But from **FCyH11SH** (0.75) to **FCyH11SH** (1.00), surface energies dramatically change from 28 mJ/m² to 18 mJ/m². More importantly, the wettability and surface energies of the mixed SAMs derived from the **HCyH11SH / FCyH11SH** SAMs do not exhibit a linear relationship with the concentration of the **FCyH11SH** in the deposition solution. These wettability behaviors limit the usage of this type of mixed SAMs to tune the wettability of surfaces.

The contact angle data suggests that the interfacial properties of the SAMs resemble the hydrocarbon SAM, **HCyH11SH**, in agreement with the XPS and PM-IRRAS data.

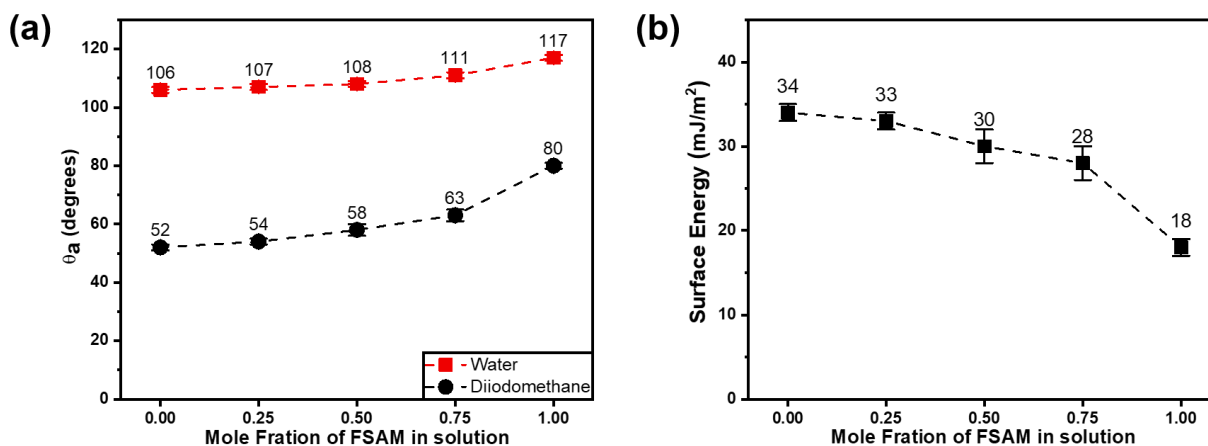


Figure 3.7. (a) Advancing contact angles of water and diiodomethane on the mixed SAMs derived from **HCyH11SH** and **FCyH11SH**, and (b) surface energies of the mixed SAMs derived from **HCyH11SH** and **FCyH11SH**. Error bars are within the symbols.

Figure 3.8 shows the advancing contact angles and surface energies of the mixed SAMs derived from the **PhH12SH** / **FPhFH11SH** series. The water contact angle data of the single component SAMs, **FPhFH11SH** (0.00) and **PhH12SH** (1.00), indicates that the underlying $\text{CF}_2\text{-CH}_2$ (FC-HC) dipole does not affect the interfacial properties of the films. Previous reports with interfacial dipoles have seen lower water contact angles on these types of surfaces than the analogous hydrocarbon SAM.¹⁴⁸ The perfluorophenyl tail group screens the FC-HC dipole leading to a water contact angle that was higher than the phenyl-terminated SAM (114° vs 90° , respectively).¹⁵⁷ A similar trend is observed with the contact angle values of diiodomethane, 76° for the **FPhFH11SH** (1.00) SAM and 44° for the **FPhFH11SH** (0.00) SAM. Furthermore, the surface energies of the SAMs, shown in Figure 3.8b, exhibit a decreasing trend as the concentration of the fluorinated adsorbate is increased. More importantly, the contact angles of both test liquids

and the surface energies exhibit a linear relationship with the composition of the solution, and is consistent with the XPS data. The data implies that the **PhH12SH** / **FPhFH11SH** SAMs can be used to tune the surface energy of surface, ranging from 38 mJ/m² to 20 mJ/m².

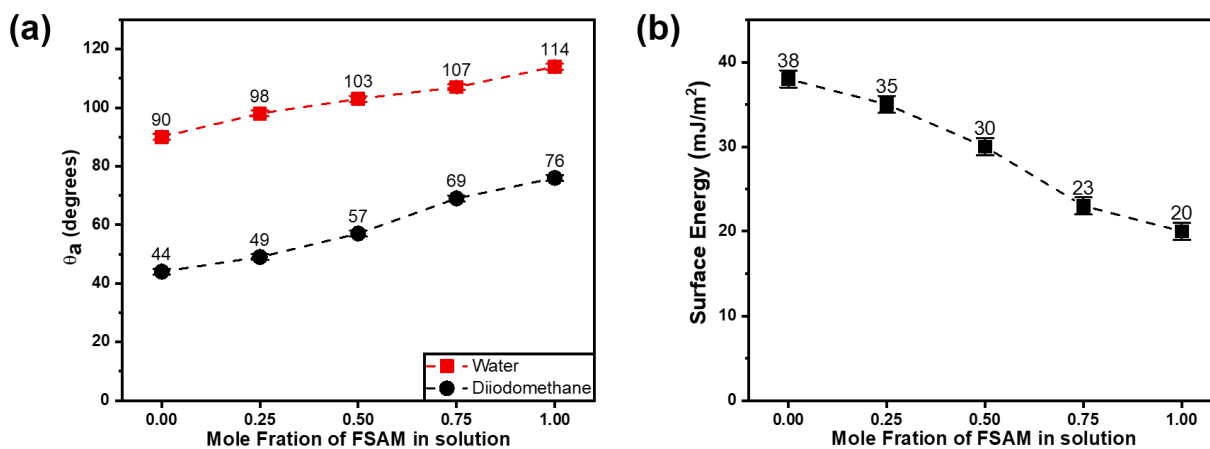


Figure 3.8. (a) Advancing contact angles of water and diiodomethane on the mixed SAMs derived from **FPhFH11SH** and **PhH12SH**, and (b) surface energies of the mixed SAMs derived from **FPhFH11SH** and **PhH12SH**. Error bars are within the symbols.

3.4. Conclusions

In this study, two types of mixed self-assembled monolayers (SAMs) derived from adsorbates terminated with either a cyclohexyl tailgroup (**HCyH11SH**) or phenyl tailgroup (**PhH12SH**) mixed with their perfluorinated analogs (**FCyH11SH** and **FPhFH11SH**, respectively) were deposited on Au(111) surfaces. The XPS results show preferential adsorption of the nonfluorinated SAM in the **HCyH11SH** / **FCyH11SH** series. In the case of the **PhH12SH** / **FPhFH11SH** mixed SAMs, a linear relationship was observed between the mole fraction of the adsorbate on the surface and the mole fraction in solution. The relative solubility, steric bulkiness, and the interaction between the two different adsorbates were determined to be major contributions to the preferential adsorption in the mixed SAMs of this class. Moreover, the mixed SAMs were also characterized using PM-IRRAS and contact angle goniometry measurements and

the surface energies of investigated surfaces were calculated using the Owens-Wendt method. In the case of the mixed SAMs derived from mixture of **PhH12SH** and **FPhFH11SH**, the contact angles of two test liquids and the surface energies show a linear relationship with respect to the mole fraction in solution, which was consistent with the composition determined from the XPS data. The results in this study suggest that the interfacial properties can be controlled with minimal loss of packing densities with the **PhH12SH** / **FPhFH11SH** mixed SAMs on metal surfaces, which is benefit to tuning the surface potential for organic thin film transistors.

Chapter 4: Surface Passivation of GaAs using Bidentate Alkanethiols

4.1. Introduction

GaAs is a novel III–V semiconductor material that has attracted increasing attention in applications such as photovoltaics (PV),²⁰⁷⁻²⁰⁸ photonics,²⁰⁹ and radio frequency (RF) transistors.²¹⁰ Compared to Si-based transistors, the higher electron mobility of GaAs ensures that GaAs radio frequency (RF) devices function at much higher frequencies, and these devices have been widely used in power amplifier (PA) components in cell phones.^{102,211} Because GaAs exhibits efficient solar absorption due to its near-ideal optical bandgap and direct-bandgap properties, GaAs solar cells currently have the highest conversion efficiency of ~29% in single-junction solar cells.^{207,212-213} In the last decade, flexible GaAs thin-film PVs have attracted significant attention in the energy industry due to their cost-effective thin film production and flexibility.²¹⁴ Additionally, flexible GaAs solar cells exhibit good resistance to strong radiation and heat, which makes GaAs solar cells excellent candidates for use in foldable solar panels on space stations and satellites and in wearable electronic devices.²¹⁵⁻²¹⁷

However, GaAs surfaces oxidize in the ambient environment and generate Ga_2O_3 and As_2O_3 , which can further react with oxygen to form As_2O_5 in half a year.²¹⁸ The latter two arsenic oxide species are volatile, forming a Ga-rich oxide layer, and Ga_2O_3 is dominant on the surface.²¹⁹ Although HCl or NH_4OH solutions have been used for etch removal of GaAs oxides in the semiconductor industry, exposure to air again oxidizes the GaAs surface in a short time.²²⁰ In GaAs solar cells, the surface oxides on GaAs accelerate surface recombination and reduce the solar cell performance significantly in a short period of time.^{105,221} Additionally, As_2O_3 is highly toxic, and its hydrolysis product, arsenic acid (H_2AsO_3), can contaminate water sources.¹⁰⁸ Hence, to enhance the durability and performance of GaAs devices, a major challenge of GaAs

semiconductor technology is surface passivation to prevent oxidation in the long term. Researchers have found that sulfur atoms can bind to unsaturated Ga or As atoms on GaAs surfaces, and several compounds containing sulfur, such as $(\text{NH}_4)_2\text{S}$,²²² Na_2S ,¹⁰⁶ trioctylphosphine sulfide,¹⁰⁵ and self-assembled monolayers (SAMs) of alkanethiol, are widely used to passivate GaAs surfaces.²²³ Alkanethiol SAMs deposited on GaAs (100) were first studied by Lunt et al.²²³ and Sheen et al.¹⁰⁷ in 1991. Unlike inorganic salts that produce toxic H_2S in GaAs surface treatment, alkanethiol SAMs on GaAs used for surface passivation are less harmful to the environment and can form a protective layer on GaAs to prevent surface reoxidation.²²⁴ Alkanethiols on Au are a well-known system used by scientists, but studies that employ SAMs on GaAs are still limited.^{17,225} Recently, Muscat and coworkers investigated SAMs of alkanethiols with different chain lengths on GaAs (100) and studied the reoxidation of GaAs(100) with SAMs in air.¹⁶⁴ They found that the packing densities of SAMs on GaAs (100) increased with chain length because interchain interactions reduced the tilt angle of the SAM molecules, allowing more thiols to be absorbed onto the GaAs surface. In 2005, Zharnikov and coworkers studied the orientation of partially fluorinated alkanethiols, $\text{F}(\text{CF}_2)_n(\text{CH}_2)_{11}\text{SH}$ ($n = 6, 8, \text{ and } 10$), on GaAs substrates. For SAMs on Au systems, various kinds of SAMs with multidentate headgroups have been reported.^{157,226} Lee and coworkers synthesized bidentate alkanethiols to form SAMs on Au (111), in which the dithiol headgroups enhanced the stability of the resulting SAMs by suppressing the formation of disulfide.²²⁷⁻²²⁸ In a follow-up study on mixed SAMs, the same group synthesized and deposited partially fluorinated bidentate alkanethiols on Au (111).¹⁸⁶

To investigate bidentate SAMs on GaAs, we deposited and characterized SAMs from bidentate alkanethiol **H16BDT** on GaAs (100) and its partially fluorinated analog **F8H8BDT**, as shown in Figure 4.1. **H16BDT** has a bidentate headgroup and a 16-hydrocarbon spacer, while

F8H8BDT has the same bidentate headgroup and an 8-fluorocarbon in its 16-carbon spacer.²²⁷⁻²²⁸ To compare monodentate alkanethiols that have the same tailgroups, hydrocarbon and fluorinated SAMs on GaAs (100) derived from **H16SH** and **F8H8SH** were prepared, as shown in Figure 4.1. Monodentate **H16SH** and **F8H8SH** have the same tailgroups as **H16BDT** and **F8H8BDT**, respectively, which allows us to study the effect of different headgroups on the surface properties. Additionally, to investigate the effect of different hydrocarbon chain lengths in SAMs, monodentate **H18SH** (octadecanethiol) and **F8H10SH**, which both have 18 carbons in their tailgroups, were deposited on GaAs (100) and characterized. Studying these SAMs on GaAs (100) provided insight into the effects of bidentate headgroups and terminally fluorinated tailgroups of SAMs on GaAs (100). Additionally, the stability and surface passivation behaviors of the investigated SAMs under ambient conditions were tested by XPS, confirming that bidentate alkanethiols can be employed to passivate GaAs surfaces. First, we used an NH₄OH solution followed by an HCl solution to remove the oxide layer on GaAs by etching and expose the As-rich GaAs surface.¹⁶⁴ Then, ellipsometry, contact angle measurements, and X-ray photoelectron spectroscopy (XPS) were used to characterize the investigated SAMs on GaAs (100).

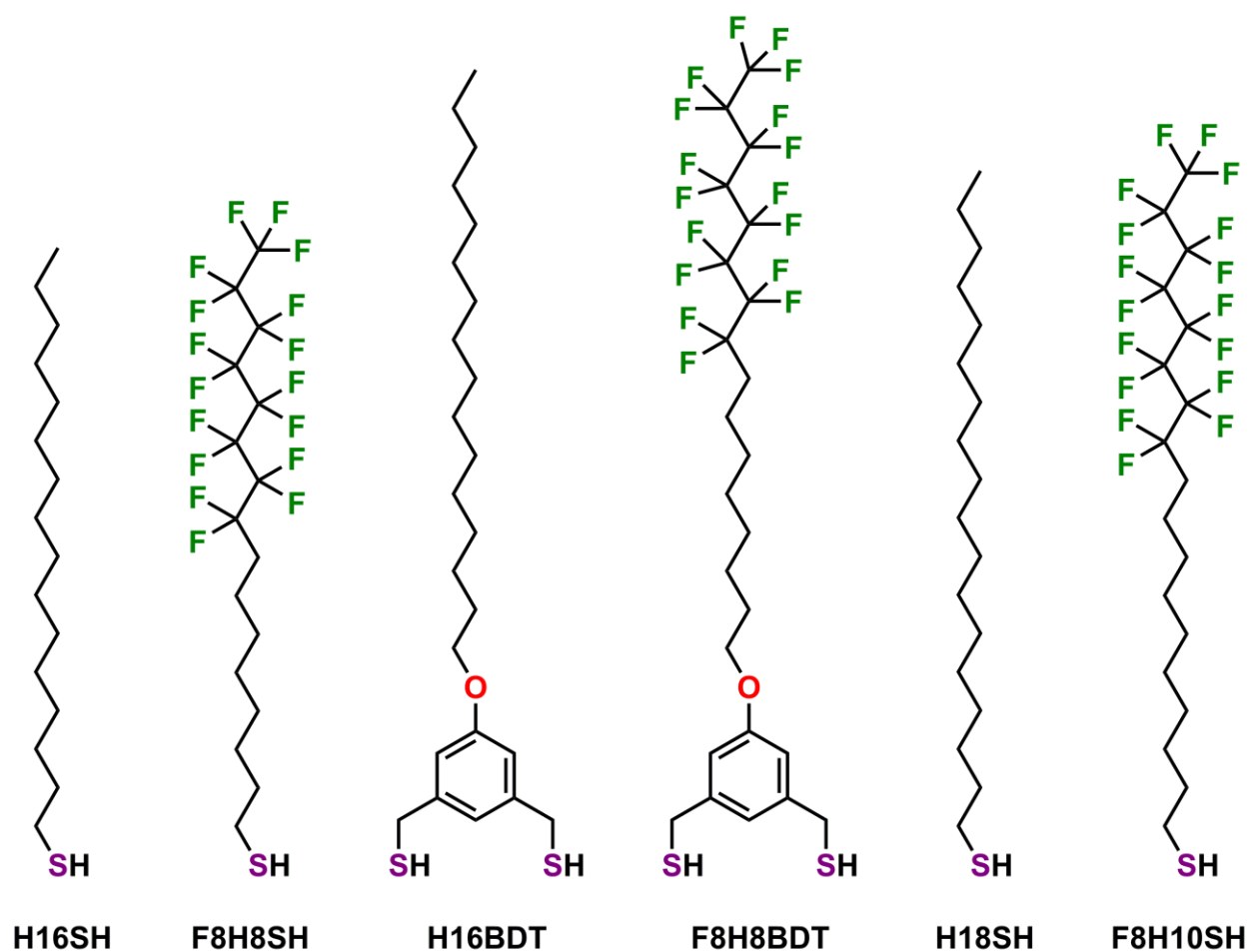


Figure 4.1. Molecular structures of the 6 adsorbates in this study.

4.2. Experimental Procedures

4.2.1. Materials and Methods

In this study, the adsorbates hexadecanethiol (**H16SH**) and octadecanethiol (**H18SH**) were purchased from Sigma-Aldrich and used as received. 9,9,10,10,11,11,12,12,13,13,14,14,15,15,16,16,16-heptafluorohexadecane-1-thio (**F8H8SH**) and 11,11,12,12,13,13,14,14,15,15,16,16,17,17,18,18,18-heptafluorooctadecane-1-thio (**F8H10SH**) were prepared following the synthetic route outlined in the literature.¹⁴⁹ (5-(hexadecyloxy)-1,3-phenylene)dimethanethiol (**H16BDT**) and (5-

(9,9,10,10,11,11,12,12,13,13,14,14,15,15,16,16,16-hepta-deca-fluorohexadecyloxy)-1,3-phenylene)dimethanethiol (**F8H8BDT**) were prepared as described in the literature.¹⁸⁶ The hydrochloric acid solution (HCl, 37%) and ammonium hydroxide solution (NH₄OH, 30%) were purchased from Mallinckrodt Chemicals and used as received. Anhydrous ethanol (EtOH – Aaper Alcohol and Chemical Co.) was degassed by purging with nitrogen gas. Water was purified by an Academic Milli-Q Water System (Millipore Corporation) and then degassed by purging with nitrogen gas before use.

4.2.3. Preparation and Characterization of the SAMs on GaAs

GaAs (100) wafers (diameter = 50.8 mm, thickness = 350 μ m, Si-doped) were purchased from University Wafer, Inc. Solutions of the 6 thiols at a concentration of 1 mM in absolute ethanol (previously degassed) were prepared in 40 mL vials that were cleaned with piranha solution and rinsed thoroughly with deionized water, followed by an absolute ethanol rinse prior to use. The cut GaAs slides (2 cm \times 1 cm) were immersed in an NH₄OH solution (15% w/w) for 5 min, rinsed with water and transferred into an HCl solution (15% w/w) for 5 min to remove the GaAs native oxide layer. Then, the GaAs slides were transferred into the respective thiol solutions without drying and incubated for 8 h at room temperature in the dark. A slide of bare GaAs (100) after etching was used as a reference. Before characterization, all substrates were rinsed with absolute ethanol and dried with ultrapure nitrogen gas.

Thickness measurements were performed on an alpha-SE ellipsometer from J.A. Woollam with the incident angle set to 70°. The refractive index was set to 1.45, which is consistent with the value of organic monolayers used in the previous literature.¹⁶⁸ The thickness value of one sample was derived from the averages of 6 measurements.

Contact angle data were obtained using a compact high-resolution CMOS camera (DCC1645C) and a 12X zoom lens (MVL12X12Z) working with a Matrix Technologies micro-Electrapette 25 that dispensed liquids from a disposable pipette tip. The contact liquids were dispensed at a speed of 1 $\mu\text{L/s}$ to obtain advancing contact angles (θ_a). Specifically, the dynamic sessile drop procedure (in which the liquid-dispensing pipette remains in contact with the drop) was used to collect the contact angle data, and images were taken while dispensing the contact liquid and maintaining the pipette tip centered on the drop. The following contact liquids were used: water (Millipore water with a resistivity of 18.2 $\text{M}\Omega\cdot\text{cm}$), hexadecane (HD – Sigma-Aldrich), and diiodomethane (CH_2I_2 – Sigma-Aldrich). A slide of bare GaAs (100) after etching was used as a reference. Before characterization, all substrates were rinsed with absolute ethanol and dried with ultrapure nitrogen gas. The reported contact angle value is the average of 3 measurements from 3 different locations for each substrate.

X-ray photoelectron spectroscopy (XPS) measurements were performed using a PHI 5700 X-ray photoelectron spectrometer with a monochromatic Al $\text{K}\alpha$ X-ray source ($h\nu = 1486.7$ eV) at an incident angle of 90° relative to the axis of the hemispherical energy analyzer. The takeoff angle from the surface was set to 45° . The tested substrates, bare GaAs (100) after etching and the 6 SAMs, were exposed to air for 30 min and for 2 days for the stability test. The binding energy of As $3d_{5/2}$ in the As 3d region was set to 41.1 eV and used as a reference peak, and each spectrum was aligned with the reference spectrum.¹⁹⁶

4.3. Results and Discussion

4.3.1. Ellipsometric Thickness Measurements.

After the 6 investigated SAMs were deposited on GaAs for 8 h, we measured the average film thickness of the investigated SAMs on GaAs (100) using ellipsometry, as shown in Table 4.1. Table 4.1 also displays the molecular lengths and ellipsometric thicknesses of the corresponding SAMs on Au (111) for comparison. The average thickness of the **H18SH** SAM on GaAs was 21 Å, which is consistent with the value collected by the same type of ellipsometry in the literature.¹⁶⁴

Table 4.1. Ellipsometric thicknesses of SAMs on GaAs derived from the investigated alkanethiols.

Adsorbate	Molecular Length (Å) ^a	Thickness on Au (Å) ^b	Thickness on GaAs (Å)
H16SH	22.4	19	16 ± 1
F8H8SH	22.7	16	16 ± 1
H16BDT	27.5	23	19 ± 1
F8H8BDT	27.8	24	20 ± 1
H18SH	24.9	22	21 ± 1
F8H10SH	25.2	18	19 ± 1

^aMolecular length calculated using Chem3D.

^bThickness of Au obtained from references^{186,203}.

Overall, the ellipsometric thickness of SAMs on GaAs or Au is affected by the molecular packing density (number of molecules per unit area), the molecular lengths, and the orientation of adsorbates.¹⁹⁷ For SAM molecules with the same number of carbons, the molecular length of the fluorinated SAMs (FSAMs) was 0.3 Å. The van der Waals diameter of fluorine is 1.47 Å, which is larger than that of hydrogen (1.20 Å), leading to bulkier fluorocarbon segments in FSAMs.¹⁵⁶⁻¹⁵⁷ Additionally, the van der Waals diameter of helical fluorocarbon chains (5.7 Å) is larger than that of hydrocarbon chains in the trans-extended conformation (4.4 Å).^{17,229} Therefore, the bulky fluorocarbon segments lower the packing densities of FSAMs on Au (111), which lead to thinner thicknesses compared to their nonfluorinated analogs, as shown in Table 4.1.²³⁰ However, among

the 6 investigated SAMs on GaAs (100), **H16SH** and **F8H8SH** had similar thicknesses of 16 Å, while the thicknesses of **H16BDT** and **F8H8BDT** were higher and within experimental error, at ~19-20 Å. **H18SH** had the highest thickness value in the tested samples, but **F8H10SH** was only 2 Å thinner than **H18SH**. It has been reported that longer chain lengths reduce the tilt angle of SAM molecules on GaAs, which increases the packing densities.¹⁶⁴ **H18SH** and **F8H10SH** had higher thicknesses than **H16SH** and **F8H8SH** due to their greater molecular lengths and higher packing densities. In contrast, the bidentate SAMs **H16BDT** and **F8H8BDT** had greater molecular lengths but were thinner than **H18SH** and **F8H10SH**, which may be due to the low packing densities, affected by the bulky bidentate headgroups compared to monodentate thiols. Another plausible reason for the reduction in thickness might arise from the orientation of bidentate SAMs, which adopt a more tilted structure than their monodentate counterparts. Further analysis of the packing densities of SAMs on GaAs (100) is detailed in the XPS section.

4.3.2. Contact Angle Measurements.

The interfacial properties of bare GaAs (100) after etching and the 6 investigated SAMs were characterized using contact angle measurements. We measured advancing contact angles (θ_a) using water and hexadecane as contact liquids on the 6 SAM surfaces. The average contact angle values were derived from the average of 6 data sets. Additionally, the surface energies were calculated using the Owens-Wendt method, which is commonly used to calculate the surface energies of organic thin films.²⁰³⁻²⁰⁶ Table 4.2 summarizes the advancing contact angles and surface energies of the substrates. The contact angle of hexadecane was less than 10° on the freshly etched GaAs surface, which is defined as fully wettable. Instead of hexadecane, we used diiodomethane to measure the advancing contact angles on bare GaAs (100) without the oxide layer, and the contact angle was 45°. The Owens-Wendt method was also used to calculate the

surface energy of bare GaAs (100) against water and diiodomethane, as shown in Table 4.2. Figure 4.2 compares the advancing contact angles and surface energies on the investigated substrates.

The freshly etched GaAs surface without native oxide was hydrophilic and had a relatively high surface energy of 63 mJ/m^2 , which is caused by the unsaturated dangling bonds on GaAs (100) surfaces after etching.²³¹ This finding also explains why freshly etched GaAs surfaces are easily reoxidized in the ambient environment. The contact angles of the SAM surfaces against water were higher than 90° , which are defined as hydrophobic surfaces. The results indicate that depositing SAMs on GaAs significantly lowered the wettability, which changed the GaAs surface from being hydrophilic to hydrophobic. Moreover, FSAMs had higher contact angles against both water and hexadecane compared to nonfluorinated SAMs due to the high hydrophobicity and oleophobicity of fluorocarbons.¹²² Additionally, the 8-carbon fluorocarbon segments at the interfaces resulted in the screening of the FC-HC dipole at the $\text{CH}_2\text{-CF}_2$ junction, causing FSAM surfaces to interact with the contact liquids solely through dispersive (van der Waals) interactions.¹⁵⁷

Table 4.2. Advancing contact angles of the investigated SAMs against water and hexadecane and surface energies of the investigated surfaces.

Surface	Water (θ_a , $^\circ$)	HD (θ_a , $^\circ$)	Surface Energy (mJ/m^2)
GaAs without oxide	39 ± 2	-	63 ± 0.7
H16SH	104 ± 2	37 ± 2	23 ± 0.7
F8H8SH	116 ± 2	72 ± 2	12 ± 0.7
H16BDT	108 ± 2	38 ± 2	22 ± 0.7
F8H8BDT	118 ± 2	76 ± 2	11 ± 0.7
H18SH	108 ± 2	43 ± 2	21 ± 0.7
F8H10SH	119 ± 2	78 ± 2	10 ± 0.7

Compared to water, which has a relatively high surface tension ($\gamma_{LV} = 72.0 \text{ mN/m}$), the low surface tension of hexadecane ($\gamma_{LV} = 27.5 \text{ mN/m}$) led to lower contact angles on all the

investigated films.¹⁷² The nonfluorinated SAMs with hydrocarbon chain tailgroups had contact angle values ranging from 37 to 43° against hexadecane, and **H18SH** had the highest value, 43°. In contrast, FSAMs showed much higher contact angle values than their nonfluorinated analogs. The highest contact angles were observed for **F8H8BDT** and **F8H10SH** due to their higher fluorocarbon chain packing densities compared with those of **F8H8SH**, which was further confirmed by XPS, as discussed in more detail in the XPS section. In addition, hexadecane is a nonpolar liquid consisting of hydrocarbon chains that have strong dispersive interactions with hydrocarbon SAMs.⁹ The 3 nonfluorinated SAMs showed similar contact angle values against water and hexadecane, and the 3 FSAMs had similar wettabilities against both contact liquids as well.

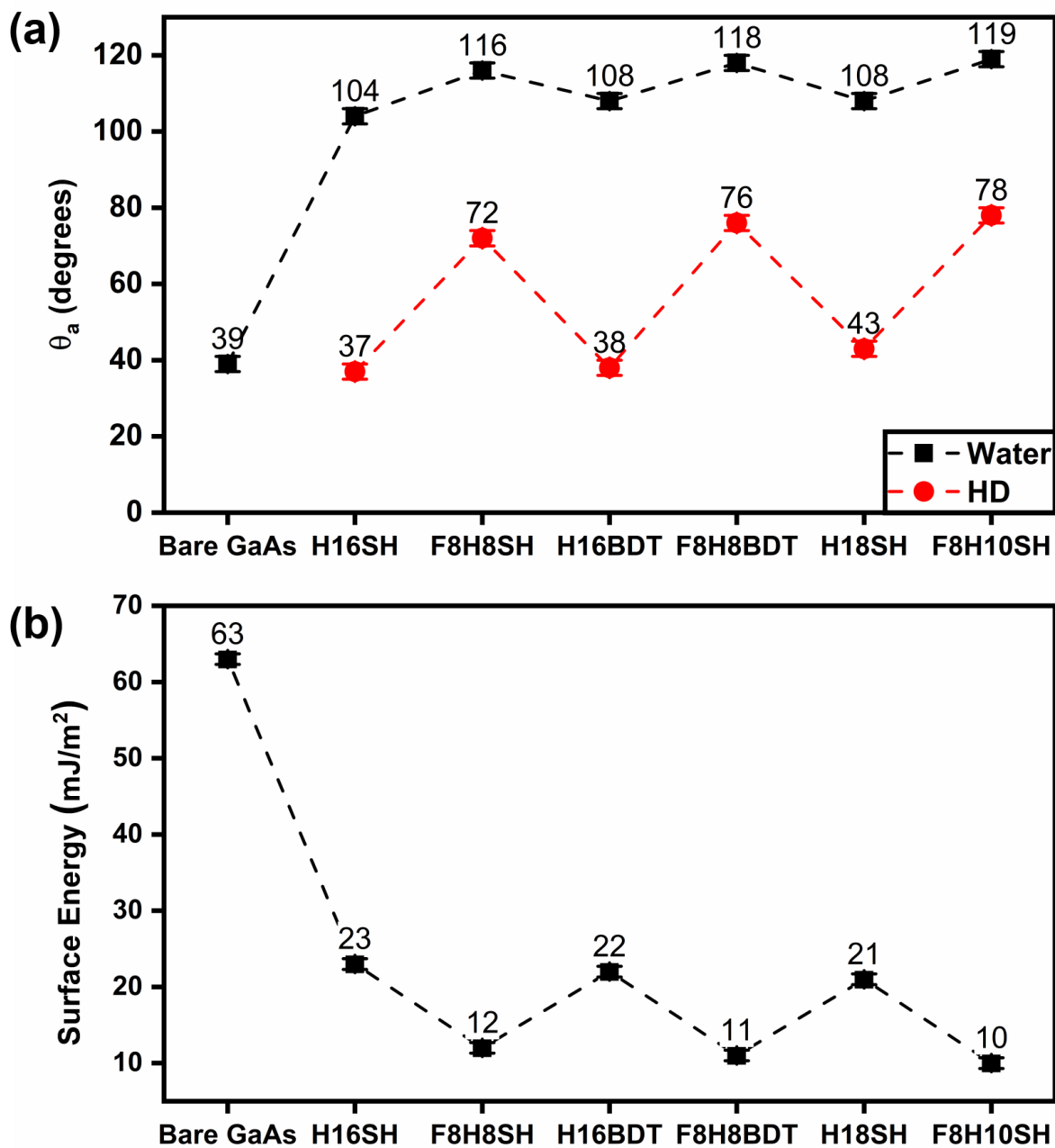


Figure 4.2. (a) Advancing contact angles of water and hexadecane and (b) surface energies of bare GaAs and the investigated SAMs.

In terms of surface energies, all the SAM surfaces had lower surface energies compared to the freshly etched GaAs (100) surface. In addition, FSAMs had lower surface energy values than

their nonfluorinated analogs. However, the surface energies of the 3 different FSAMs and the 3 nonfluorinated SAMs were similar. To investigate the difference in the SAM packing densities on GaAs (100), XPS was used to further analyze the impact of bidentate headgroups and different chain lengths.

4.3.3. XPS Analysis of the Composition and Packing of SAMs.

Figure 4.2a and 4.2b show XPS spectra of Ga 3d of the freshly etched bare GaAs and SAMs after 30 min and 2 days of ambient exposure, while Figure 4.2c and 4.2d show spectra of the As 3d binding region. The precise binding energies of the peaks in the spectra and assignments are provided in Table 4.3 and agree with the literature.^{219,232-234}

In the Ga 3d spectra of all samples, the Ga 3d_{5/2} peak attributed to GaAs was located at 19.3 ± 0.1 eV. Because the spin-orbit splitting of Ga 3d is only 0.43 eV, the GaAs peaks attributed to Ga 3d_{3/2} and Ga 3d_{5/2} appeared as a single peak.²³² For the bare GaAs stored in ambient conditions for 30 min, reoxidation of the surface led to the formation of native oxides in the form of Ga₂O₃, which resulted in a shoulder peak that was located above 20.2 eV and overlapped with the GaAs peak. Two days of air exposure resulted in thickening of the oxide layer on the surface, and the shoulder peak attributed to Ga₂O₃ increased compared to the GaAs peak. In contrast, in the other SAM spectra, after etch removal of the oxide layer and deposition of the SAMs on GaAs (100), no oxide peaks were observed after air exposure for 30 min. After 2 days, as shown in Figure 4.2b, the oxide peak from Ga₂O₃ was barely noticeable.

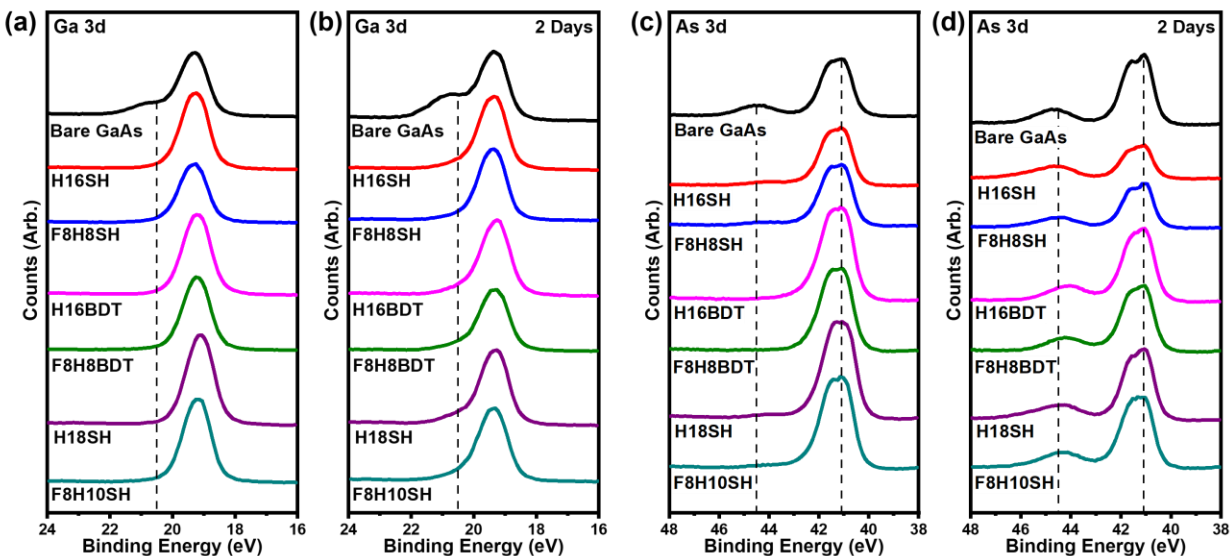


Figure 4.3. XPS spectra of the Ga 3d binding region after (a) 30 min and (b) 2 days of ambient exposure and As 3d after (c) 30 min and (d) 2 days of ambient exposure of the SAMs. The vertical dashed lines are guides to the eye indicating the peak positions.

Similarly, in the As 3d spectra shown in Figure 4.2c and 4.2d, As 3d_{3/2} and As 3d_{5/2} attributed to GaAs appeared as a single peak at 41.1 eV due to the low value of spin-orbit splitting of 0.69 eV.²³⁵ Bare GaAs after air exposure for 30 min and 2 days showed an additional broad peak at 44.5 eV from arsenic oxides, mainly As₂O₃. In contrast, no oxide peak was observed in the spectra of SAMs after 30 min of air exposure. After 2 days, the spectra in Figure 4.2d showed oxide peaks above 43.0 eV in all samples. Figure 4.4 compares the ratio of oxides to bulk of the As 3d integrated intensities (peak areas) after 2 days of air exposure. The results show that bare GaAs without surface passivation had the highest oxide-to-bulk ratio, while the bidentate SAMs **H16BDT** and **F8H8BDT** had the best surface passivation properties. The lattice spacing values of H18SH SAMs on GaAs (100) have been reported to be 4.7 Å and 5.0 Å, and the tilt angle of alkanethiols is 14°. ²³⁶⁻²³⁷ However, the nearest neighbor (NN) spacing of atoms on an ideal GaAs (100) surface is 4.0 Å, which is too small for alkanethiols to bind to every As atom at the GaAs (100) interface. The next nearest neighbor spacing (NNN) of ideal GaAs (100) is 5.6 Å. Another

study by Muscat and coworkers showed that **H18SH** only reaches a surface coverage of 4.2 thiols/nm², while the ideal saturation coverage calculated by As atoms on GaAs (100) is 6.7 thiols/nm².¹⁶⁴ Therefore, we assume that the dithiol headgroup in **H16BDT** and **F8H8BDT** allows more As atoms to reach GaAs, which can passivate the GaAs surface from oxidation.

Table 4.3. Peak assignment and binding energies (eV) from XPS spectra of bare GaAs and **PF PDT** SAM on GaAs (100) by stamping.

Binding Region	Assignment	Binding Energy (eV)	Spin-Orbit Splitting (eV)	branching ratio (3d_{3/2}:3d_{5/2})
Ga 3d	native oxide (Ga ₂ O ₃)	>20.2		
	Ga 3d _{5/2} (GaAs)	19.3 ± 0.1	0.43	2:3
As 3d	native oxide (As ₂ O ₃)	44.5		
	As 3d _{5/2} (GaAs)	41.1 (reference)	0.69	2:3

Interestingly, comparing the monodentate analogs with the same carbon number, **H16SH** and **F8H8SH** and **H18SH** and **F8H10SH**, the fluorinated SAMs had lower oxide-to-bulk ratios than the nonfluorinated SAMs. It has been reported that the oxide layer on GaAs dissolves rapidly and that continuous etching occurs in water at the GaAs surface.¹⁰⁸ In addition, alkanethiols with hydrophilic tailgroups lack the ability to prevent GaAs from undergoing oxidation.²³⁸ Based on these facts, we assume that moisture in ambient conditions accelerates the GaAs oxidation process and that the highly hydrophobic fluorinated tailgroups of FSAMs act as an excellent moisture diffusion barrier.

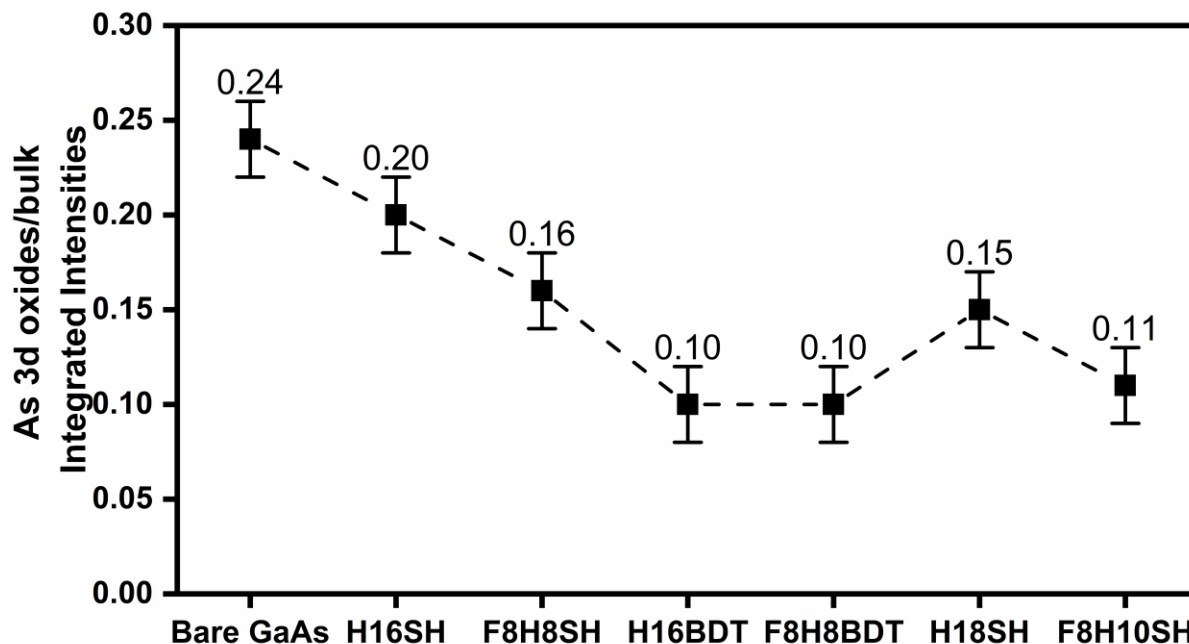


Figure 4.4. Ratio of oxide to bulk of As 3d integrated intensities after 2 days of ambient exposure. The values were derived from an average of 3 data sets.

Similar to the spectra shown in Figure 4.3, the XPS spectra of the S 2p binding region are shown in Figure 4.5a and 4.5a. The XPS spectra of the S 2p region were used to evaluate the binding species of thiol-based SAMs, although the S 2p region overlapped with the Ga 3s peak located at 160.0 eV for alkanethiol SAMs on GaAs.^{197,239} According to the literature, the spin-orbit splitting of the S 2p doublet is 1.18 eV, and the branching ratio ($2p_{1/2}$ to $2p_{3/2}$) is 1 to 2.¹⁹⁶ Compared to bare GaAs, in addition to the large peak at 160.0 eV that is attributed to Ga 3s, a shoulder peak appeared at 162.0 ± 0.1 eV in every SAM spectrum. This peak belongs to the S $2p_{3/2}$ of the doublet from bound thiolates. However, S $2p_{1/2}$ at ~ 163 eV was superimposed by the Ga 3s signal, which proves that the alkanethiols are chemically absorbed onto the GaAs (100) surface.^{164,236} As shown in Figure 4.5b, the S 2p signals from monodentate SAMs decreased noticeably after 2 days of air exposure because of the desorption of SAMs from the GaAs surfaces and the formation of an oxide layer on GaAs. Interestingly, only in the spectra of **H16BDT** and

F8H8BDT did the shoulder peak shift from 162.0 eV to 163.2 eV, which can be attributed to the S 2p_{3/2} of the doublet from unbound thiols.¹⁶³ The “chelate effect” may explain why the bidentate headgroup did not desorb from the GaAs surface in the way monodentate thiols did. Lee and coworkers proved that bidentate thiols can resist the formation of intramolecular disulfides because of the extended distance between the two sulfur atoms in the bidentate headgroup (4.9 Å).²²⁷ As a result of the reoxidation of GaAs (100) surfaces in air, the monodentate SAMs might oxidize to disulfide and desorb from the substrates.²⁴⁰ In contrast, some bidentate SAMs might form unbound thiols on the GaAs surface, while other bidentate thiols remain intact. Despite this partial desorption of the bidentate SAMs as thiols, the “chelate effect” of the bidentate headgroup helped **H16BDT** and **F8H8BDT** SAMs to remain on the GaAs surface. This conclusion is also consistent with the aforementioned results obtained from the XPS spectra in the As 3d binding region.

The XPS spectra of the C 1s binding region are shown in Figure 4.5c and 4.5d. We noticed a small broad peak in the spectrum of bare GaAs from ambient hydrocarbon contamination.²⁴¹ In the spectra of nonfluorinated SAMs, **H16SH**, **H16BDT**, and **H18SH** only showed one peak located at 284.6 ± 0.1 eV in the C 1s binding region, which was attributed to CH₂ and phenyl ring carbons. The similar binding energies of the carbons in the bidentate thiol can also be observed in XPS spectra of **H16BDT** on Au.¹⁸⁶ For the FSAMs, **F8H8SH**, **F8H8BDT**, and **F8H10SH**, three peaks appeared in the spectrum at 293.4 ± 0.1 eV, 291.3 ± 0.1 eV, and 284.6 ± 0.1 eV that are attributed to CF₃, CF₂ in the fluorocarbon chain, and the rest of the hydrocarbons, respectively. Figure 4.6 shows the ratios of the total C 1s integrated intensities (peak areas) divided by the number of carbons (n) and normalized by As 3d. These ratios obtained from the spectra in Figure 4.5c and 4.5d were used to compare the molecular packing densities of SAMs on GaAs (100).^{164,197,226} Since the effective attenuation lengths of hydrocarbon chains and fluorocarbon

chains are identical, the packing densities of both nonfluorinated SAMs and FSAM can be calculated in the same manner.¹⁶⁶ After the SAMs were deposited on GaAs for 30 min, the result shows that **H18SH** had the highest packing density, followed by **H16BDT** and **F8H10SH**, which had similar packing densities within experimental error. **F8H8BDT** had a lower packing density than the abovementioned SAMs but a higher packing density than **H16SH** and **F8H8SH**.

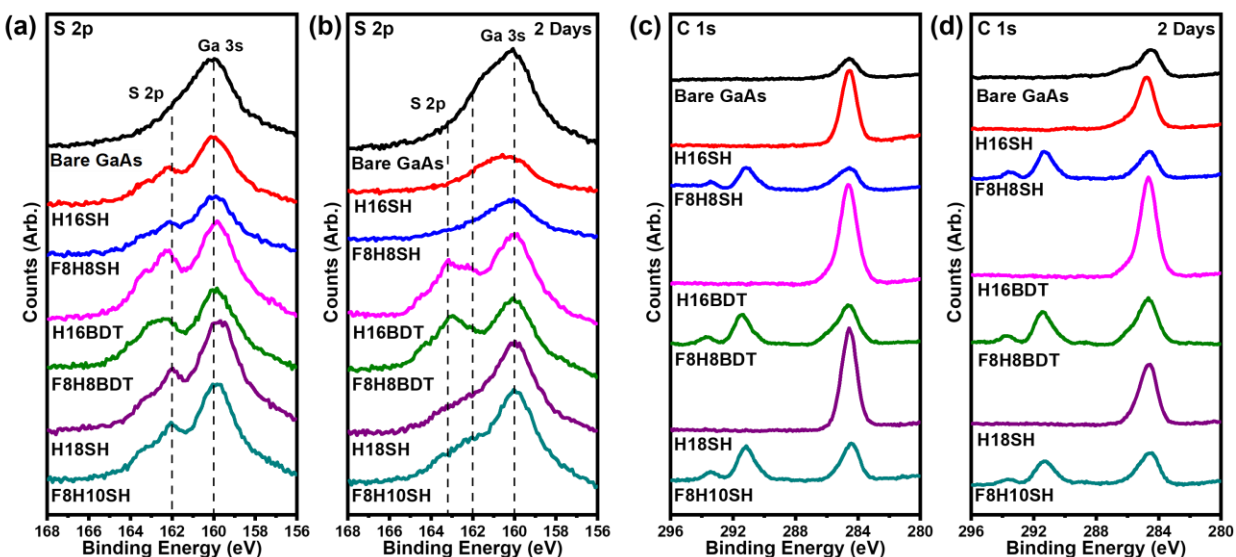


Figure 4.5. XPS spectra of the S 2p after (a) 30 min and (b) 2 days of ambient exposure, C 1s after (c) 30 min and (d) 2 days of ambient exposure of the SAMs. The vertical dashed lines are guides to the eye to indicate the peak positions.

Our observation is consistent with a previous study from Muscat and coworkers, in which a longer chain length led to higher packing densities due to the reduced tilt angle of the tailgroups, which allowed more thiols adsorb onto the GaAs surface.¹⁶⁴ In our case, the packing densities of two FSAMs, **F8H8SH** and **F8H8BDT**, which had lower packing densities than their nonfluorinated analogs, were impacted by the bulky fluorocarbon chains. In addition, the bulky bidentate headgroups led to low packing densities of **H16BDT** and **F8H8BDT**, although they had greater molecular lengths than **H18SH** and **F8H10SH**. Because **H16SH** and **F8H8SH** had the shortest hydrocarbon chain lengths among the 6 investigated SAMs, they also had the lowest

packing densities. With these low molecular packing densities, compared to **H16SH**, it seems that the fluorocarbon segments in **F8H8SH** did not affect the packing density. After 2 days of ambient exposure, the molecular packing densities of the SAMs decreased due to the partial desorption of the SAMs from the GaAs substrates. However, bidentate SAMs retained the highest packing densities compared to any other monodentate SAMs due to the “chelate effect” mentioned above. Moreover, bidentate FSAMs decreased less than their nonfluorinated analogs due to the high hydrophobicity of fluorinated films preventing moisture from diffusing onto the GaAs interfaces.

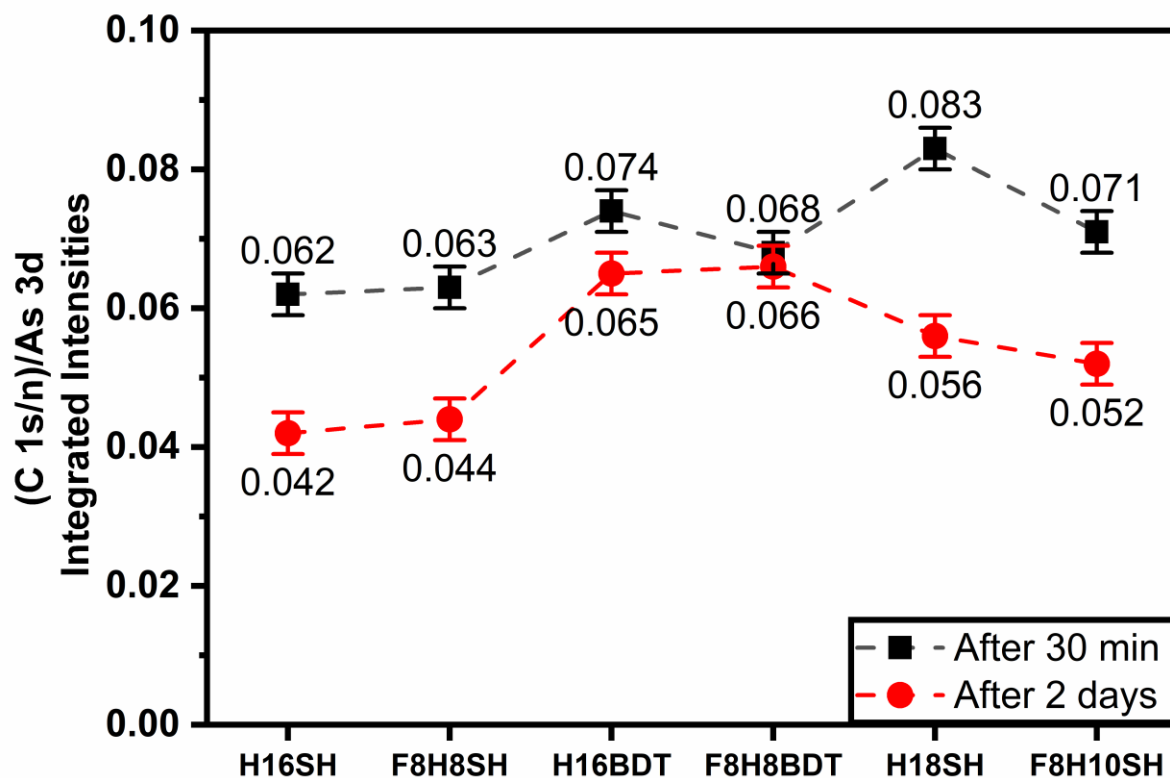


Figure 4.6. Ratio of the total C 1s integrated intensities divided by the number of C atoms (n) to all the As 3d integrated intensities after 30 min (black squares) and 2 days (red circles) of ambient exposure. The values were derived from an average of 3 data sets.

Furthermore, XPS spectra of the F 1s and O 1s binding regions under two different conditions are shown in Figure 4.7. In Figure 4.7a and 4.7b, the FSAMs, **F8H8SH**, **F8H8BDT**,

and **F8H10SH**, exhibit strong signals at ~ 688.8 eV. No fluorine signal was observed in the spectra of bare GaAs and nonfluorinated SAMs. Similarly, after 2 days, the fluorine signals decreased because SAMs were partially desorbed from the GaAs surfaces. Additionally, as shown in Figure 4.7c, bare GaAs exhibited a strong signal located at ~ 531.5 eV in the O 1s region, which might be the result of GaAs oxides that were formed from surface reoxidation and hydrocarbon contamination.^{238,241} In contrast, those oxide signals were barely noticeable in the spectra of the monodentate SAMs. The bidentate SAMs exhibited a small peak at 532.7 eV, which was attributed to the oxygen atom in the bidentate headgroup. After 2 days of air exposure, all the spectra showed peaks at ~ 531.5 eV because of GaAs surface reoxidation. Because of the existence of hydrocarbon contamination and the relatively low intensities of the O 1s signals from SAMs, it is difficult to perform a quantitative analysis based on the integrated intensities such as As 3d and C 1s spectra.

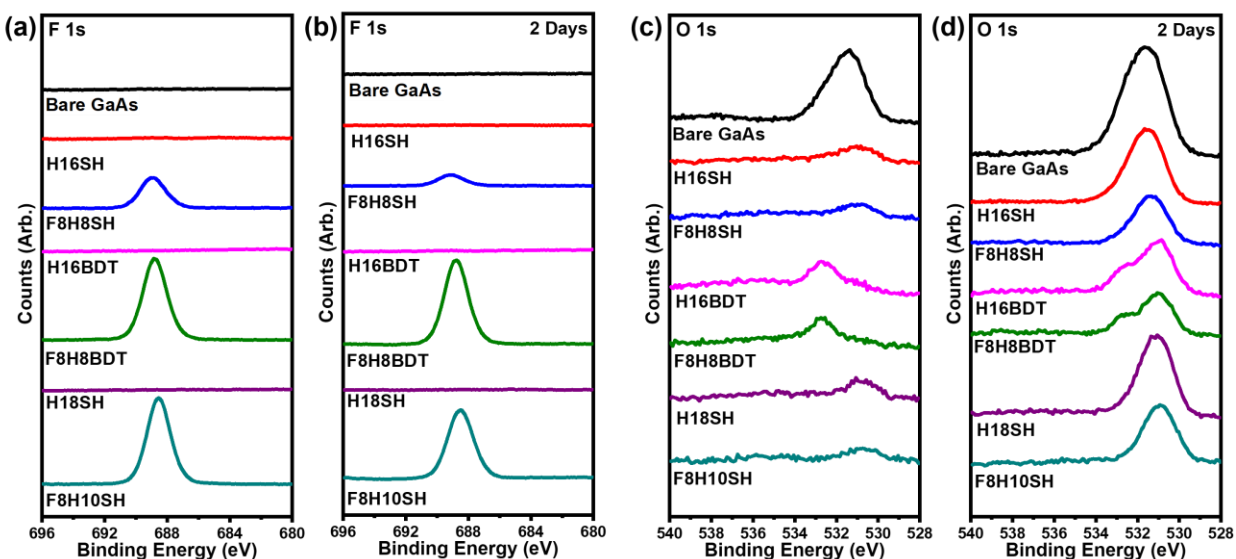


Figure 4.7. XPS spectra of the F 1s after (a) 30 min and (b) 2 days ambient exposure, O 1s after (c) 30 min and (d) 2 days ambient exposure of the SAMs.

4.4. Conclusions

The bidentate alkanethiols **H16BDT** and **F8H8BDT**, as well as their monodentate analogs **H16SH**, **F8H8SH**, **H18SH**, and **F8H10SH**, were deposited on GaAs (100) to form monolayers

for the passivation of GaAs surfaces. The investigated thin films were characterized using ellipsometry, contact angle measurements, and XPS. The results of the contact angle measurements indicate that FSAMs were more hydrophobic and oleophobic than nonfluorinated SAMs. Overall, the FSAMs on GaAs (100) exhibited lower surface energies than nonfluorinated SAMs. Analysis by XPS showed that all the studied alkanethiols can be used for GaAs surface passivation, suppressing surface reoxidation of GaAs. In addition, both bidentate SAMs, **H16BDT** and **F8H8BDT**, had superior surface passivation properties. Furthermore, although **H18SH** had the highest molecular packing densities, **H16BDT** and **F8H8BDT** were most stable after 2 days of ambient exposure. Studying the interfacial properties, chemical composition, and stability of these alkanethiols on GaAs (100) provided insight into the effect of bidentate headgroups and fluorinated segments in alkanethiols on GaAs (100). The bidentate alkanethiols **H16BDT** and **F8H8BDT** with excellent stability can serve as a new type of material for the surface passivation of GaAs.

Chapter 5: Microstructuring GaAs Using Reverse-Patterning Lithography: Implications for Transistors and Solar Cells

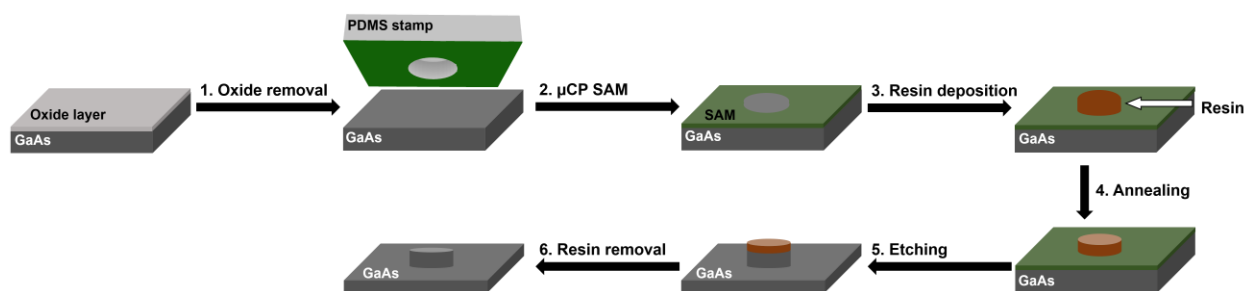
5.1. Introduction

GaAs is an important III–V compound used in applications that require precise and/or demanding properties, such as photovoltaics (PVs) and microwave and radio-frequency (RF) transistors. Although more costly than other semiconductors (e.g., silicon), GaAs exhibits low resistance, low off capacitance, high linearity at high frequencies, high electron mobility, and a direct bandgap.²⁴²⁻²⁴⁴ The high electron mobility allows GaAs transistors to function at much higher frequencies than Si-based devices in RF applications.²⁴⁵ Moreover, GaAs offers outstanding photovoltaic performance due to its direct bandgap.²⁴⁶ For example, compared to Si-based materials, GaAs-based photovoltaic solar cells have been found to exhibit record-breaking conversion efficiencies, such as ~29% for single-junction cells.¹⁰⁴ In RF applications, higher electron mobility allows GaAs amplifiers to function at much higher frequencies than Si-based devices.²¹¹ Moreover, due to the widespread use of 4G networks and the current deployment of 5G, power amplifier modules in cell phones have also begun to implement GaAs as the semiconductor of choice.¹⁰² However, processing GaAs substrates to fabricate devices is difficult, costly, and requires numerous lithographic steps.^{103,214}

Conventional methods used for the fabrication of microelectronic devices include photolithography,²⁴⁷ thermal nanoimprint lithography (T-NIL),²⁴⁸⁻²⁴⁹ and UV-based nanoimprint lithography (UV-NIL).²⁵⁰⁻²⁵¹ The former method requires an expensive photoresist and photomask aligner. Conversely, the latter two methods require plasma treatment or reactive ion etching to remove the residual layer of the polymer resist used prior to the imprinting step.²⁵² In an effort to

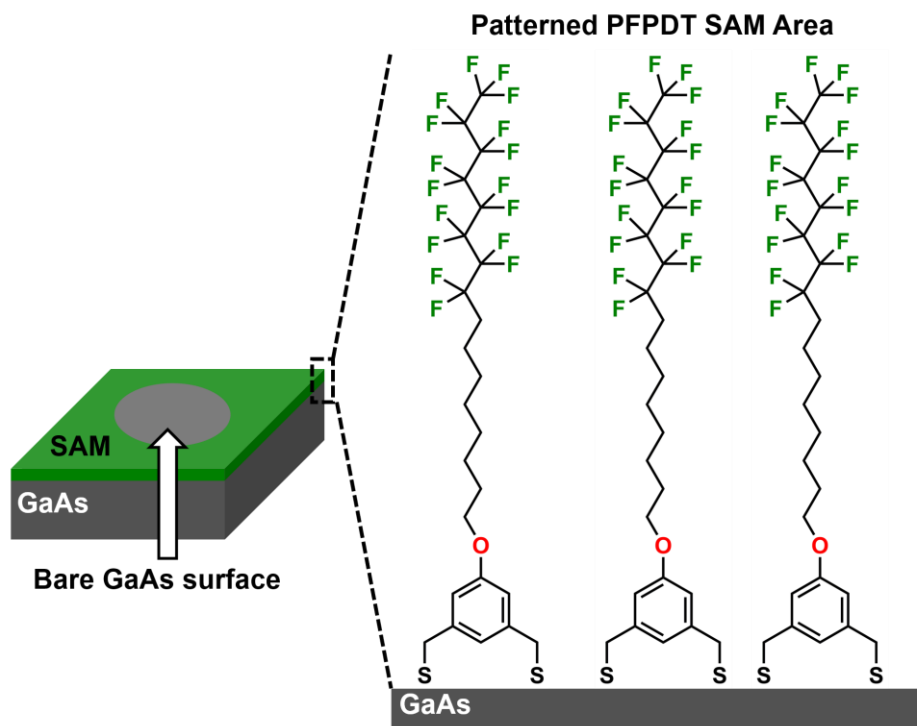
simplify the fabrication of GaAs-based devices, we have developed a cost-efficient method in which the combination of a microcontact printed (μ CP) self-assembled monolayer (SAM) and a polymeric resin as a wet-etching resist was used to microstructure GaAs substrates. The new method, hereafter referred to as "reverse patterning lithography" (RPL; Scheme 5.1), takes advantage of the ability of the sulfur of *n*-alkanethiols to bind to GaAs surfaces to form nanoscale monolayer coatings that are poorly wettable and can be tuned to be anti-adhesive.^{107-108,164,253}

Scheme 5.1. Illustration of Reverse Patterning Lithography for Microstructuring GaAs Substrates



Extensive research conducted by the Lee group on SAMs generated on Au surfaces has shown enhanced thermal and chemical stability for films generated from bidentate adsorbates, when compared to the monodentate counterparts, due to the "chelate effect".^{19,226-227} Furthermore, fluorinated materials, such as fluoropolymers and SAMs, have been shown to exhibit low surface energies, inertness, as well as high hydrophobicity and oleophobicity compared to their hydrocarbon counterparts.¹²² To leverage the enhanced stability of the bidentate headgroup and the hydrophobic and oleophobic nature of fluorocarbons, we designed and synthesized the fluorinated adsorbate, (5-(9,9,10,10,11,11,12,12,13,13,14,14,15,15,16,16,16-heptafluorohexadecyloxy)-1,3-phenylene) dimethanethiol (**PFPDT**), shown in Scheme 5.2, for use as an ink for patterning via microcontact printing (μ CP). The μ CP process generates a hydrophobic and oleophobic thin film on selective areas of the GaAs substrate, which leads to microstructuring of GaAs in the RPL process (see Scheme 5.2).

Scheme 5.2. Illustration of Bidentate Fluorinated (9,9,10,10,11,11,12,12,13,13,14,14,15,15,16,16,16-Heptadeca-fluorohexadecyloxy)-1,3-phenylene)dimethanethiol (**PFPDT**) for μ CP of GaAs Substrates. (5-



A list of materials, the procedure used for the fabrication of the polydimethylsiloxane (PDMS) stamps, as well as in-depth descriptions of the methods used to characterize the substrates are provided in the Supporting Information. As noted above, Scheme 5.2 illustrates the RPL method. Overall, microstructuring of GaAs single crystal substrates can be achieved in 6 steps. The first step in the RPL method involves removal of the native oxide layer atop the GaAs(100) wafer via submersion in ammonia solution (15% w/w) for 5 min followed by submersion into an HCl solution (15% w/w) for an additional 5 min with a water-rinsing step prior to introduction of the substrate into the HCl solution. After removal of the oxide layer, the fluorinated SAM was printed onto the freshly cleaned GaAs surface using a PDMS stamp for 60 sec (step 2, Scheme 5.2). The PDMS stamp was saturated with a 1 mM **PFPDT** solution in EtOH followed by drying

the stamp with a flow of nitrogen. After formation of the hydrophobic pattern, the patterned GaAs surface was dipped into a resin solution made of 10% w/w phenolic resin in methoxypropyl acetate, then pulled out immediately to form a "reverse" resin pattern (Step 3, Scheme 5.2). Note, the resin only covers the bare hydrophilic GaAs area, whereas the hydrophobic **PFPDT** SAM-covered areas remain uncoated. The GaAs sample was then annealed at 120 °C for 5 min to form a hard resin pattern with a thickness of ~0.20 μm at the center (Step 4, Scheme 5.2). After annealing, the GaAs sample was placed into an etching solution (H₂O: H₂O₂: H₂SO₄ = 280:8:1 vol.) for 10 min to form the designed pattern (Step 5, Scheme 5.2). The final step of the process involves the removal of the resin by washing the GaAs substrate with acetone.

5.2. Experimental Section

5.2.1 Materials

The adsorbate (5-(9,9,10,10,11,11,12,12,13,13,14,14,15,15,16,16,16-heptafluorohexadecyloxy)-1,3-phenylene)dimethanethiol (**PFPDT**) was prepared as described in the literature.¹⁸⁶ GaAs(100) wafers (diameter = 50.8 mm, thickness = 350 μm, Si doped) were purchased from University Wafer, Inc. Phenolic resin SP-6700 was purchased from Akrochem[®]; polydimethylsiloxane (PDMS, SYLGARD[®]-184) was purchased from Dow Corning[®]; and the photoresist (AZ 5214) and photoresist developer (AZ400) were purchased from MicroChemicals[®]. Hydrochloric acid solution (HCl, 37%), ammonium hydroxide solution (NH₄OH, 30%), and hydrogen peroxide solution (H₂O₂) were purchased from Macron Fine Chemicals. The anhydrous ethanol (EtOH – Aaper Alcohol and Chemical Co.) was used as received. Water was purified by an Academic Milli-Q Water System (Millipore Corporation) before use. Acetone was purchased from Mallinckrodt Chemicals.

5.2.2 Fabrication of PDMS Stamps

To make the patterned stamp used in reverse patterning lithography (RPL), a 1-micron-thick positive mesa pattern with photoresist (AZ 5214) was deposited on a Si wafer by using a photomask aligner (Karl SUSS MJB3); the positive mesa pattern served as a mold of the patterned stamp. After that, SYLGARD 184 PDMS base (100.0 g) was mixed with the curing agent (10.0 g) in a 10:1 ratio, then placed in a desiccator under vacuum to remove air bubbles. After 1 h, the freshly prepared PDMS mixture was slowly poured onto the patterned photoresist to create a 2-cm deep PDMS layer. Finally, the PDMS/Si wafer was placed in an oven and cured at 80 °C for 1 h to obtain the PDMS stamp having a negative pattern.

5.2.3 Microcontact Printing Procedure

A cotton swab was used to apply a 1 mM **PF PDT** solution in EtOH on a flat PDMS stamp, followed by drying the stamp with a stream of nitrogen. Simultaneously, a pre-cut GaAs slide (2 cm × 1 cm) was placed in ammonia solution (15% w/w) for 5 min, then rinsed with water and transferred into an HCl solution (15% w/w) for 5 min to remove the GaAs oxide layer. The GaAs slide was rinsed with ethanol and dried with nitrogen. Then, the PDMS stamp was placed in contact with the GaAs surface, without applying any force, for 60 sec.

5.2.4 Characterization of the PF PDT-Printed GaAs

Thickness measurements were collected on an alpha-SE ellipsometer from J. A. Woollam with an incident angle set to 70°. The refractive index was set to 1.45, which is consistent with the value used in previous literature studies of organic monolayers.¹⁶⁸

X-Ray photoelectron spectroscopy (XPS) measurements were performed using a PHI 5700 X-Ray photoelectron spectrometer with a monochromatic Al K α X-ray source (h ν = 1486.7 eV)

incident at 90° relative to the axis of the hemispherical energy analyzer. The takeoff angle from the surface was set to 45° . All GaAs samples were placed in an ambient environment for 30 min then rinsed with ethanol and dried with a nitrogen flow prior to measurements. The binding energy of the As $3d_{5/2}$ in the As 3d region was set to 41.1 eV and was used as a reference peak in each spectrum.¹⁹⁶ The spin-orbit splitting (0.69 and 1.18 eV, respectively), and branching ratios of 2/3 ($3d_{3/2}$ to $3d_{5/2}$) and 1/2 ($2p_{1/2}$ to $2p_{3/2}$) were used in the peak deconvolution of the Ga 3d and S 2p peaks.²³⁵

Contact angle data were obtained using a compact high-resolution CMOS camera (DCC1645C) and 12X zoom lens (MVL12X12Z) working with a Matrix Technologies micro-Electrapette 25 dispensing liquids from a disposable pipette tip. Contacting liquids were dispensed at a speed of 1 $\mu\text{L/s}$ to obtain advancing contact angles (θ_a). The specific method used to collect the contact angle data was the dynamic sessile drop procedure (where the liquid dispensing pipette remains in contact with the drop), with images taken during the dispensing of the contacting liquid, maintaining the pipette tip centered on the drop. Adobe[®] Photoshop[®] was used to measure the angles on each side of the dispensed droplets. The following contacting liquids were used: water (Millipore water with a resistivity of 18.2 $\text{M}\Omega\cdot\text{cm}$) and diiodomethane (CH_2I_2 – Sigma-Aldrich).

5.3. Results and Discussion

5.3.1 Analysis of PFPDT SAM Composition on GaAs Using XPS.

To confirm the presence of the monolayer, the GaAs substrates were subjected to elemental analysis using X-ray photoelectron spectroscopy (XPS). Figure 5.1 shows the XPS spectra of the Ga 3d, As 3d, C 1s, F 1s, S 2p, and O 1s binding regions of the bare GaAs and PFPDT-printed GaAs after 30 min of ambient exposure, and Table 1 lists the assigned peaks along with their

binding energies; peak assignments were based on examples found in the literature.^{196,232-234} The Ga 3d binding energy region of both substrates exhibits a peak at 19.3 eV (Figure 5.1A). Due to a spin-orbit splitting of only 0.43 eV, the Ga 3d_{3/2} and Ga 3d_{5/2} peaks are indistinct and appear as a single peak. Furthermore, the bare GaAs (stored in ambient conditions) produces a native oxide layer, Ga₂O₃, which appears as a shoulder at 20.6 eV, overlapping with the GaAs peak. We note that the PFPDT-printed GaAs sample (blue line plotted in Figure 5.1A) fails to exhibit the shoulder associated with the oxide, indicating not only the successful removal of the oxide layer upon treatment with **PFPDT**, but also protection from oxidation of the surface for at least 30 min of ambient exposure.

Similarly, the As 3d binding energy region (Figure 5.1B) produced a single peak due to the small spin-orbit splitting of 0.69 eV for the As 3d_{3/2} and As 3d_{5/2} peaks at 41.1 eV. We also note the presence of arsenic oxides, As₂O₃ and As₃O₅, corresponding to the peak at ~43.0 eV; in contrast, in the spectrum of the **PFPDT**-printed surface there is no oxide peak (blue line plotted in Figure 5.1B). As noted for the Ga 3d spectra, the As 3d spectra of the **PFPDT** SAM protects the GaAs surface from oxidation for at least 30 min under ambient conditions. The presence of the oxides is also apparent in the O 1s spectrum of the bare GaAs surface (Figure 5.1C), with a sharp peak at 531.9 eV, while a markedly less pronounced peak is weakly noticeable in the **PFPDT**-printed surface.

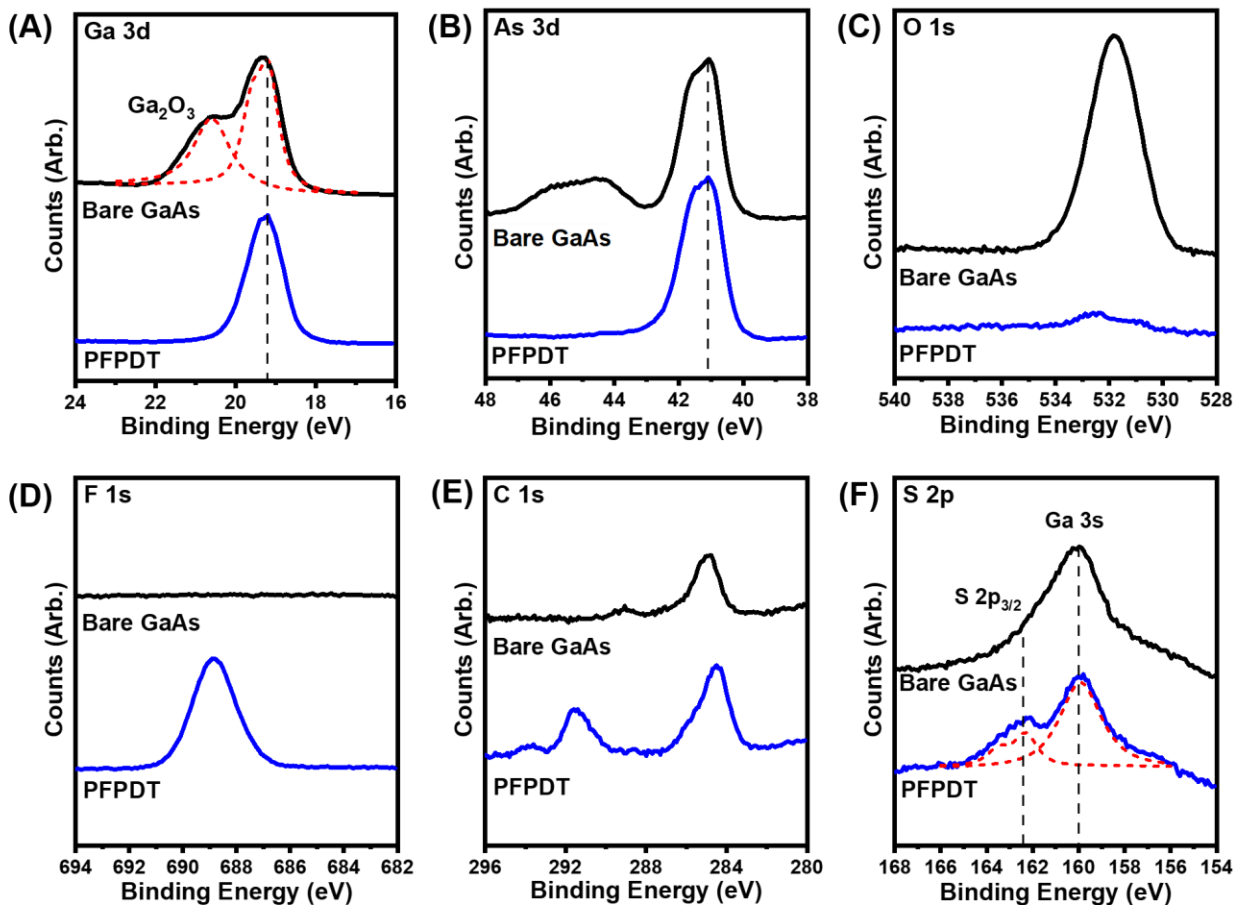


Figure 5.1. XPS spectra of the (A) Ga 3d, (B) As 3d, (C) O 1s, (D) F 1s, (E) C 1s, and (F) S 2p binding regions of the bare GaAs and **PFPDT**-printed GaAs(100) surface. The GaAs surface was exposed to ambient conditions for 30 min. The red dashed lines represent deconvoluted peaks.

Note that the peak at 532.7 eV in the spectrum of the **PFPDT**-printed surface arises from the oxygen atom connected to the phenyl ring. As for the F 1s region (Figure 5.1D), only the **PFPDT**-printed surface produces a prominent peak at 688.9 eV due to the fluorocarbons on the adsorbate, which are absent on the bare GaAs surface. In Figure 5.1E, there is a small peak from ambient hydrocarbon contamination in the C 1s region for the bare GaAs at 284.8 eV that is not present in the **PFPDT**-printed surface.²⁴¹ On the other hand, the three peaks in the spectrum of the **PFPDT**-printed surface can be attributed to the **PFPDT** adsorbate on the surface; specifically, the peaks at 293.4 eV, 291.4 eV, and 284.5 eV are attributed to the CF₃, CF₂, CH₂, and carbons of

the phenyl ring, respectively.²²⁷ Finally, the spectra in the S 2p region in Figure 5.1F was used to evaluate the binding of the thiol headgroup on the GaAs surface. The overlapping Ga 3s peak at 160.0 eV²³⁶ complicates the evaluation of the binding; however, peak deconvolution (red line in Figure 5.1F) reveals a doublet that can be attributed to S 2p_{1/2} (~163.4 eV) and S 2p_{3/2} (~162.3 eV), which are characteristic of a bound thiolate on GaAs.¹⁶⁴

Table 5.1. Peak Assignment and Binding Energies (eV) from XPS Spectra of the Bare GaAs and PFPDT-Printed GaAs(100) Surfaces

Binding Region	Assignment	Binding Energy (eV)		
		Bare GaAs	PFPDT SAM	Reference
Ga 3d	gallium oxides	20.6	-	>19.8
	Ga 3d _{5/2} (GaAs)	19.3	19.3	19.2 ± 0.04
As 3d	arsenic oxides	>43.0	-	>43.0
	As 3d _{5/2} (GaAs)	41.1	41.1	41.1 ± 0.04
C 1s	carbon contamination	284.8	-	284.8
	CF ₃	-	293.4	
	CF ₂	-	291.4	
	CH ₂	-	284.5	
F 1s	F in PFPDT	-	688.9	
S 2p	Ga 3s	160.0	160.0	160.0 ± 0.07
	S 2p _{1/2}	-	163.4	
	S 2p _{3/2}	-	162.3	
O 1s	GaAs oxides	531.9	-	532.0 ± 0.04
	O in PFPDT	-	532.7	

Ellipsometric Thickness and Contact Angle Measurements. To confirm the formation of the monolayer and evaluate its interfacial properties, we characterized the GaAs substrate by ellipsometry before and after removal of the oxide layer as well as after printing with the PFPDT SAM. As shown by the ellipsometry data in Table 2, the PFPDT adsorbate produces a SAM that

is 14 Å thick, even with a short deposition time of 1 min. Although the monolayer is thinner than the corresponding SAM on Au (24 Å) after 48 h of incubation,¹⁸⁶ the monolayer on GaAs produces a hydrophobic and oleophobic film (see Table 2). To demonstrate the interfacial properties of the μ CP-SAM, advancing contact angles using water and diiodomethane were measured, and the surface energies were calculated using the Owens-Wendt method (see Table 2).²⁵⁴

Table 5.2. Ellipsometric Thickness of the **PF PDT** SAM, Advancing Contact Angles of Water and Diiodomethane on the Investigated Surfaces, and Surface Energies of the Investigated Surfaces

Surface	SAM Thickness (Å)	Water (θ_a , °)	CH ₂ I ₂ (θ_a , °)	Surface Energy (mJ/m ²)
GaAs with oxide	-	76 ± 2	45 ± 2	40 ± 1
GaAs without oxide	-	39 ± 2	27 ± 2	63 ± 1
PF PDT SAM	14 ± 1	116 ± 2	80 ± 2	18 ± 1

The contact angle data in Table 2 show that the bare GaAs surface with and without the oxide layer are hydrophilic, with water contact angles of 76° and 39°, respectively, in contrast with the **PF PDT**-printed substrate (water contact angle of 116°). A similar trend was observed with regard to oleophobicity using diiodomethane as the contacting liquid, which gave contact angles of 45°, 63°, and 80° for the GaAs with oxide, without oxide, and **PF PDT**-printed substrate, respectively.

Moreover, the GaAs(100) surface with a native oxide layer exhibited a surface energy of 40 mJ/m², which increased by more than 50% (to 63 mJ/m²) after etching of the oxide layer. In contrast, printing of **PF PDT** on the GaAs surface lowered the surface energy to 18 mJ/m², which is comparable to PTFE (18-19 mJ/m²).^{9,122} The drastically different surface energies of the **PF PDT**-printed and bare GaAs substrate (without the oxide layer) is one of the leading forces behind the dewetting of selective areas observed following our method. However, we also note

that dewetting is also a function of the surface tension and adhesive behavior of the phenolic resin on the GaAs surface. We found that a 10% w/w phenolic resin in methoxy-propyl acetate in combination with the **PF PDT**-printed SAM exhibited the best results for creating clear patterns on GaAs by dip coating (vide infra).

5.3.2 Analysis of the Lithography Results.

After printing the SAM onto the GaAs surface, deposition of the resin, and subsequent annealing at 120 °C for 5 min, the solvent in the resin solution evaporated to give a hard resin pattern. Figure 5.2 shows cross-section profiles and microscope images of the **PF PDT**-printed GaAs surface after steps 4, 5, and 6 of the RPL process using mesas with a diameter of 250.0 μm as a representative example. The cross-section profile shown in Figure 5.2A depicts a mesa with a thickness of 0.20 ± 0.05 μm in the center. The edges exhibited a greater thickness (additional 0.80 ± 0.05 μm) compared to the center region due to a coffee-ring effect, Figure 5.2D, arising from the stamping method.²⁵⁵ Regardless of the disparate resin deposition, Figure 5.2B shows that sharp-edges are obtained after etching with the resin remaining unchanged at the top, Figure 5.2E. Furthermore, after removal of the resin in the final step, the mesa on the GaAs substrate exhibited clear edges with minimal defects, as shown in Figures 5.2C and 5.2F.

The mesas can reach a thickness of 3.0 μm in 10 min, depending on the morphology of the GaAs material and wet etching time. The above results indicate that the phenolic resin acts as a wet-etching resist that is stable in etching solution (i.e., dilute hydrogen peroxide/sulfuric acid) and protects the GaAs surface underneath. The SAM-coated area, on the other hand, is etched due to the oxidizable sulfur groups bound to the GaAs surface. Here, we note a similar etching speed for the SAM-printed GaAs areas as the bare GaAs, which indicates that the SAM layer decomposes within 1 min in the etching solution. However, we note that longer etching times in efforts to

obtain mesas thicker than $3.0\ \mu\text{m}$ lead to deformed edges due to the thinness of the resin as well as the isotropic etching effect of the etching solution.

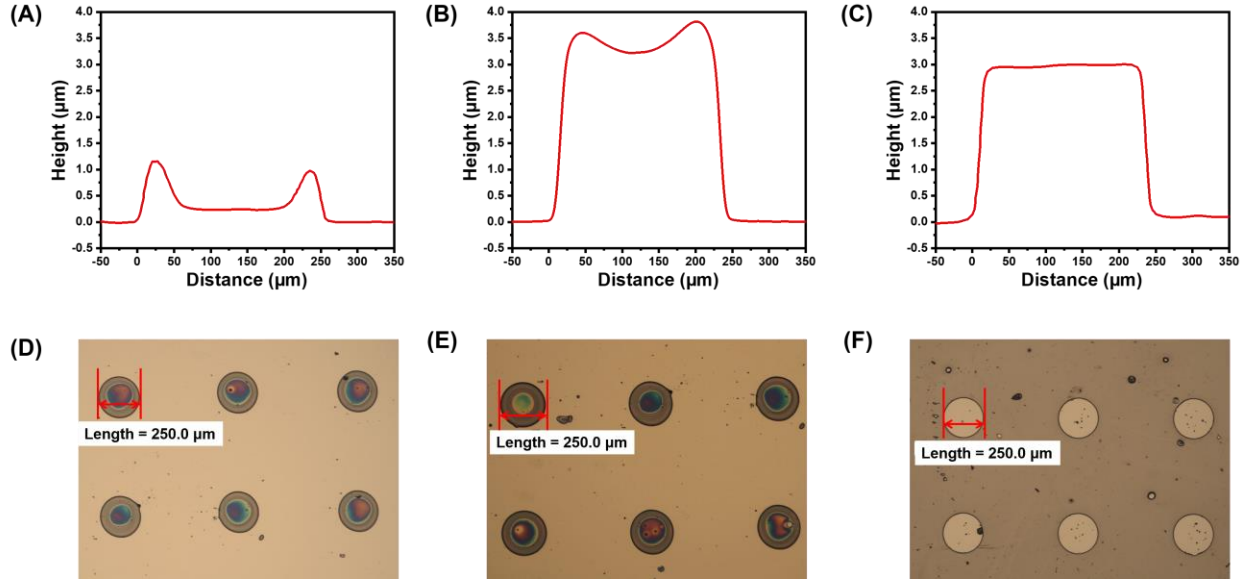


Figure 5.2. Cross-section profiles for mesa with a diameter = $250.0\ \mu\text{m}$ atop GaAs with corresponding microscope images (A, D) before etching, (B, E) after etching, and (C, F) after etching and resin removal.

To determine the resolution of the RPL method, we reduced the diameter of the mesa. As shown in Figure 5.3A, mesas in total with diameters of $100.0\ \mu\text{m}$ were obtained on GaAs with minimal defects following the RPL method. Attempts to decrease the diameter of the mesa further led to incomplete mesas, limiting the RPL method to structures with diameters of $100.0\ \mu\text{m}$. In addition to obtaining mesas with a minimum diameter of $100.0\ \mu\text{m}$, the RPL method can also be used for the large-scale production of mesas on GaAs; ~ 400 mesas were obtained per stamp. To evaluate the versatility of the RPL method, we produced stamps with various shapes and sizes. Figure 5.3B shows the generated structures with sharp edges ranging in size from $200\text{-}1500\ \mu\text{m}$.

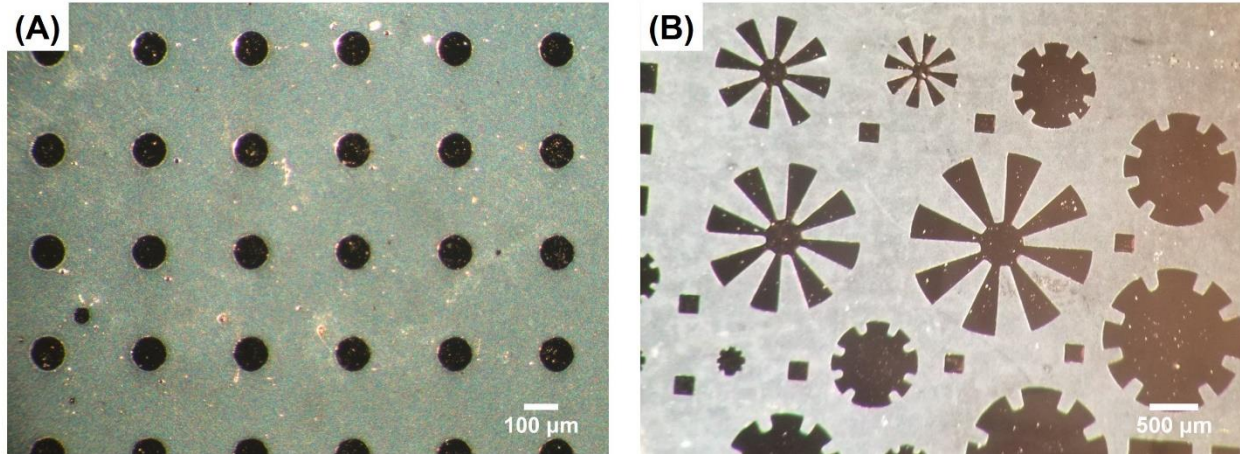


Figure 5.3. Microscope images of (A) mesas with a diameter of 100 μm and (B) microstructures on GaAs of different sizes and shapes.

5.4. Conclusions

In summary, we developed a new microstructuring method for GaAs substrates, reverse patterning lithography (RPL) as an alternative to conventional photolithography. Ellipsometric data and contact angle measurements of the **PFPDT**-printed GaAs surfaces show a 14-Å-thick hydrophobic and oleophobic SAM, which significantly decreased the surface energy of the original oxide-free GaAs surface. Analysis of the printed SAM by XPS showed that the **PFPDT** adsorbate binds chemically to the GaAs surface and prevents its facile reoxidation. Studies using the RPL patterning method illustrated positive pattern formation on GaAs wafers using various designed shapes. The patterns obtained by the RPL method can reach a diameter of 100.0 μm with a depth of up to 3.0- μm thick by wet etching. These results not only validate the feasibility of the RPL method for the formation of microstructures on GaAs substrates, but also provide a new paradigm for microstructuring GaAs substrates that warrants further investigation for the large-scale manufacturing of GaAs-based devices, with particular relevance for transistors and solar cells.

Chapter 6: Conclusions

Over the past few decades, self-assembled monolayers (SAMs) have been widely used as a robust surface modification method. The ability to chemically modify the adsorbates used in generating SAMs, specifically by incorporating fluorine atoms, gives thin films hydrophobic and oleophobic properties as well as reduced adhesion and friction coefficients. The focus of this dissertation is on the development of SAMs on gold and GaAs as surface wettability modifiers. All of the generated SAMs were characterized with the following techniques: ellipsometry, to measure thickness; X-ray photoelectron spectroscopy (XPS), to determine chemical composition; and contact angle measurements, to probe the wettability and surface energy. The SAMs on gold were also characterized by polarization-modulation infrared reflection-absorption spectroscopy (PM-IRRAS), to determine relative crystallinity of the films.

Chapter 2 introduced adsorbates on gold derived from cyclohexyl-terminated SAMs (**HCyHnSH**) and perfluorocyclohexyl-terminated SAMs (**FCyHnSH**) that serve as interfacial polymer mimics on metal substrates. The monolayer films were characterized using ellipsometry, XPS, PM-IRRAS, and contact angle measurements. Analysis by XPS indicated that the **FCyHnSH** SAMs exhibited lower packing densities than their hydrocarbon analogs, and both types of SAMs exhibited lower packing densities than the **H18SH** films, which correlated with the steric bulk of the chain termini in these SAMs. The PM-IRRAS spectra showed that the chain backbones of both **FCyHnSH** and **HCyHnSH** SAMs were less conformationally ordered than normal hydrocarbon analogs. Furthermore, the **HCyHnSH** SAMs exhibited wettability similar to PE, while their fluorocarbon analogs exhibited wettability similar to PTFE for a wide range of contacting liquids with no evidence of surface reconstruction in the SAMs. Therefore, SAMs on gold derived from cyclohexyl-terminated thiols can act as mimics of nanoscale polymer films and

can be used in future studies (e.g., ion-surface collisions and plasma modification) without concerns of surface reconstruction.

Chapter 3 introduced two types of mixed self-assembled monolayers (SAMs) on gold derived from adsorbates terminated with a cyclohexyl tailgroup (**HCyH11SH**) and a phenyl tailgroup (**PhH12SH**) mixed with their perfluorinated analogs, respectively. The XPS results show preferential adsorption of the nonfluorinated adsorbate for the **HCyH11SH / FCyH11SH** samples. The relative solubility, steric bulkiness, and the interaction between the two different adsorbates were determined to be major contributions to the preferential adsorption in the mixed SAMs of this class. In the case of the mixed SAMs derived from **PhH12SH** and **FPhFH11SH**, these two factors compensated for each other and a linear relationship was observed between the mole fraction on the surface and the mole fraction in solution. Moreover, the mixed SAMs were also characterized using PM-IRRAS and contact angle goniometry measurements and the surface energies of the investigated surfaces were calculated using the Owens-Wendt method. In the case of the mixed SAMs derived from mixture of **PhH12SH** and **FPhFH11SH**, the contact angles of two test liquids and the surface energies show a linear relationship with respect to the mole fraction in solution, which was consistent with the composition determined from the XPS data. The results in this study suggest that the interfacial properties can be controlled with minimal loss of packing densities with the **PhH12SH / FPhFH11SH** mixed SAMs on metal surfaces.

Chapter 4 investigated the bidentate alkanethiols **H16BDT** and **F8H8BDT**, as well as the monodentate alkanethiols **H16SH**, **F8H8SH**, **H18SH**, and **F8H10SH** on GaAs(100) for the passivation of GaAs surfaces. The results of the contact angle measurements indicate that FSAMs were more hydrophobic and oleophobic than the nonfluorinated SAM. Overall, the FSAMs on GaAs(100) exhibited lower surface energies than nonfluorinated SAMs. Analysis by XPS showed

that all the studied alkanethiols can be used for GaAs surface passivation, suppressing surface reoxidation of GaAs. Furthermore, **H16BDT** and **F8H8BDT** were the most stable after 2 days of ambient exposure. The bidentate alkanethiols, **H16BDT** and **F8H8BDT**, with excellent stability can serve as a new type of material for the surface passivation of GaAs.

Finally, we developed a new microstructuring method for GaAs substrates, reverse patterning lithography (RPL), as an alternative to conventional photolithography. Studies using the RPL patterning method illustrated positive pattern formation on GaAs wafers using various designed shapes. The patterns obtained by the RPL method can reach a diameter of 100.0 μm with a depth of up to 3.0- μm thick by wet etching. These results not only validate the feasibility of the RPL method for the formation of microstructures on GaAs substrates, but also provide a new paradigm for microstructuring GaAs substrates that warrants further investigation for the large-scale manufacturing of GaAs-based devices, with particular relevance for transistors and solar cells.

Bibliography

1. Nuzzo, R. G.; Allara, D. L. Adsorption of bifunctional organic disulfides on gold surfaces. *J. Am. Chem. Soc.* **1983**, *105*, 4481–4483.
2. Bain, C. D.; Troughton, E. B.; Tao, Y. T.; Evall, J.; Whitesides, G. M.; Nuzzo, R. G. Formation of monolayer films by the spontaneous assembly of organic thiols from solution onto gold. *J. Am. Chem. Soc.* **1989**, *111*, 321–335.
3. Nuzzo, R. G.; Zegarski, B. R.; Dubois, L. H. Fundamental studies of the chemisorption of organosulfur compounds on gold(111). Implications for molecular self-assembly on gold surfaces. *J. Am. Chem. Soc.* **1987**, *109*, 733–740.
4. Kim, S. H.; Asay, D. B.; Dugger, M. T. Nanotribology and MEMS. *Nano Today* **2007**, *2*, 22–29.
5. Nuzzo, R. G. Biomaterials: Stable antifouling surfaces. *Nat. Mater.* **2003**, *2*, 207–208.
6. Alom Ruiz, S.; Chen, C. S. Microcontact printing: A tool to pattern. *Soft Matter* **2007**, *3*, 168–177.
7. Wilbur, J. L.; Kumar, A.; Kim, E.; Whitesides, G. M. Microfabrication by microcontact printing of self-assembled monolayers. *Adv. Mater.* **1994**, *6*, 600–604.
8. Doms, M.; Feindt, H.; Kuipers, W. J.; Shewtanasoontorn, D.; Matar, A. S.; Brinkhues, S.; Welton, R. H.; Mueller, J. Hydrophobic coatings for MEMS applications. *J. Micromech. Microeng.* **2008**, *18*, 055030
9. Yu, T.; Marquez, M. D.; Zenasni, O.; Lee, T. R. Mimicking Polymer Surfaces Using Cyclohexyl- and Perfluorocyclohexyl-Terminated Self-Assembled Monolayers. *ACS Appl Nano Mater* **2019**, *2*, 5809–5816.
10. Maboudian, R.; Ashurst, W. R.; Carraro, C. Self-assembled monolayers as anti-stiction coatings for MEMS: characteristics and recent developments. *Sens. Actuators, A* **2000**, *82*, 219–223.
11. Kasai, T.; Bhushan, B.; Kulik, G.; Barbieri, L.; Hoffmann, P. Micro / nanotribological study of perfluorosilane SAMs for antistiction and low wear. *J. Vac. Sci. Technol., B* **2005**, *23*, 995–1003.
12. Bhushan, B.; Kasai, T.; Kulik, G.; Barbieri, L.; Hoffmann, P. AFM study of perfluoroalkylsilane and alkylsilane self-assembled monolayers for anti-stiction in MEMS/NEMS. *Ultramicroscopy* **2005**, *105*, 176–188.
13. Grönbeck, H.; Curioni, A.; Andreoni, W. Thiols and Disulfides on the Au(111) Surface: The Headgroup–Gold Interaction. *J. Am. Chem. Soc.* **2000**, *122*, 3839–3842.
14. Crudden, C. M.; Horton, J. H.; Ebralidze, I.; Zenkina, O. V.; McLean, A. B.; Drevniok, B.; She, Z.; Kraatz, H. B.; Mosey, N. J.; Seki, T.; Keske, E. C.; Leake, J. D.; Rousina-Webb, A.; Wu, G. Ultra stable self-assembled monolayers of N-heterocyclic carbenes on gold. *Nat. Chem.* **2014**, *6*, 409–414.
15. Onclin, S.; Ravoo, B. J.; Reinhoudt, D. N. Engineering silicon oxide surfaces using self-assembled monolayers. *Angew. Chem. Int. Ed. Engl.* **2005**, *44*, 6282–6304.
16. Delamarche, E.; Michel, B.; Kang, H.; Gerber, C. Thermal Stability of Self-Assembled Monolayers. *Langmuir* **1994**, *10*, 4103–4108.
17. Ulman, A. Formation and Structure of Self-Assembled Monolayers. *Chem. Rev.* **1996**, *96*, 1533–1554.

18. Allara, D. L.; Parikh, A. N.; Rondelez, F. Evidence for a Unique Chain Organization in Long Chain Silane Monolayers Deposited on Two Widely Different Solid Substrates. *Langmuir* **1995**, *11*, 2357–2360.
19. Srisombat, L.; Jamison, A. C.; Lee, T. R. Stability: A key issue for self-assembled monolayers on gold as thin-film coatings and nanoparticle protectants. *Colloids Surf., A* **2011**, *390*, 1–19.
20. Geyer, W.; Stadler, V.; Eck, W.; Zharnikov, M.; Götzhäuser, A.; Grunze, M. Electron-induced crosslinking of aromatic self-assembled monolayers: Negative resists for nanolithography. *Appl. Phys. Lett.* **1999**, *75*, 2401–2403.
21. Angelova, P.; Vieker, H.; Weber, N. E.; Matei, D.; Reimer, O.; Meier, I.; Kurasch, S.; Biskupek, J.; Lorbach, D.; Wunderlich, K.; Chen, L.; Terfort, A.; Klapper, M.; Mullen, K.; Kaiser, U.; Götzhäuser, A.; Turchanin, A. A universal scheme to convert aromatic molecular monolayers into functional carbon nanomembranes. *ACS Nano* **2013**, *7*, 6489–6497.
22. Schmid, M.; Wan, X.; Asyuda, A.; Zharnikov, M. Modification of Self-Assembled Monolayers by Electron Irradiation: The Effect of Primary Energy (10–500 eV). *J. Phys. Chem. C* **2019**, *123*, 28301–28309.
23. Eck, W.; Stadler, V.; Geyer, W.; Zharnikov, M.; Götzhäuser, A.; Grunze, M. Generation of Surface Amino Groups on Aromatic Self-Assembled Monolayers by Low Energy Electron Beams—A First Step Towards Chemical Lithography. *Adv. Mater.* **2000**, *12*, 805–808.
24. Meyerbroker, N.; Zharnikov, M. Modification of nitrile-terminated biphenylthiol self-assembled monolayers by electron irradiation and related applications. *Langmuir* **2012**, *28*, 9583–9592.
25. Turchanin, A.; Götzhäuser, A. Carbon nanomembranes from self-assembled monolayers: Functional surfaces without bulk. *Prog. Surf. Sci.* **2012**, *87*, 108–162.
26. Turchanin, A.; Kafer, D.; El-Desawy, M.; Woll, C.; Witte, G.; Götzhäuser, A. Molecular mechanisms of electron-induced cross-linking in aromatic SAMs. *Langmuir* **2009**, *25*, 7342–7352.
27. Houplin, J.; Dablemont, C.; Sala, L.; Lafosse, A.; Amiaud, L. Electron Processing at 50 eV of Terphenylthiol Self-Assembled Monolayers: Contributions of Primary and Secondary Electrons. *Langmuir* **2015**, *31*, 13528–13534.
28. Amiaud, L.; Houplin, J.; Bourdier, M.; Humblot, V.; Azria, R.; Pradier, C. M.; Lafosse, A. Low-energy electron induced resonant loss of aromaticity: consequences on cross-linking in terphenylthiol SAMs. *Phys. Chem. Chem. Phys.* **2014**, *16*, 1050–1059.
29. Luo, Y.-R. Comprehensive Handbook of Chemical Bond Energies. **2007**, 1–1656.
30. Zharnikov, M.; Grunze, M. Modification of thiol-derived self-assembling monolayers by electron and x-ray irradiation: Scientific and lithographic aspects. *J. Vac. Sci. Technol., B* **2002**, *20*, 1793–1807.
31. Zhang, X.; Vieker, H.; Beyer, A.; Götzhäuser, A. Fabrication of carbon nanomembranes by helium ion beam lithography. *Beilstein J. Nanotechnol.* **2014**, *5*, 188–194.
32. Turchanin, A.; Schnietz, M.; El-Desawy, M.; Solak, H. H.; David, C.; Götzhäuser, A. Fabrication of molecular nanotemplates in self-assembled monolayers by extreme-ultraviolet-induced chemical lithography. *Small* **2007**, *3*, 2114–2119.
33. Cabrera-Sanfeliix, P.; Arnau, A.; Sanchez-Portal, D. First-principles investigation of electron-induced cross-linking of aromatic self-assembled monolayers on Au(111). *Phys. Chem. Chem. Phys.* **2010**, *12*, 1578–1584.

34. Koch, S.; Kaiser, C. D.; Penner, P.; Barclay, M.; Frommeyer, L.; Emmrich, D.; Stohmann, P.; Abu-Husein, T.; Terfort, A.; Fairbrother, D. H.; Ingolfsson, O.; Golzhauser, A. Amplified cross-linking efficiency of self-assembled monolayers through targeted dissociative electron attachment for the production of carbon nanomembranes. *Beilstein J. Nanotechnol.* **2017**, *8*, 2562–2571.
35. Yildirim, C.; Füser, M.; Terfort, A.; Zharnikov, M. Modification of Aromatic Self-Assembled Monolayers by Electron Irradiation: Basic Processes and Related Applications. *J. Phys. Chem. C* **2017**, *121*, 567–576.
36. Mrugalla, A.; Schnack, J. Classical molecular dynamics investigations of biphenyl-based carbon nanomembranes. *Beilstein J. Nanotechnol.* **2014**, *5*, 865–871.
37. Ishida, T.; Hara, M.; Kojima, I.; Tsuneda, S.; Nishida, N.; Sasabe, H.; Knoll, W. High Resolution X-ray Photoelectron Spectroscopy Measurements of Octadecanethiol Self-Assembled Monolayers on Au(111). *Langmuir* **1998**, *14*, 2092–2096.
38. Smith, B. W. Optical projection lithography. In *Nanolithography*, Feldman, M., Ed.; Woodhead Publishing, 2014, pp 1–41.
39. Altissimo, M. E-beam lithography for micro-nanofabrication. *Biomicrofluidics* **2010**, *4*, 026503.
40. Groves, T. R. Electron beam lithography. In *Nanolithography*, Feldman, M., Ed.; Woodhead Publishing, 2014, pp 80–115.
41. Tseng, A. A.; Kuan, C.; Chen, C. D.; Ma, K. J. Electron beam lithography in nanoscale fabrication: recent development. *IEEE Transactions on Electronics Packaging Manufacturing* **2003**, *26*, 141–149.
42. Gölzhäuser, A.; Eck, W.; Geyer, W.; Stadler, V.; Weimann, T.; Hinze, P.; Grunze, M. Chemical Nanolithography with Electron Beams. *Adv. Mater.* **2001**, *13*, 803–806.
43. Gölzhäuser, A.; Geyer, W.; Stadler, V.; Eck, W.; Grunze, M.; Edinger, K.; Weimann, T.; Hinze, P. Nanoscale patterning of self-assembled monolayers with electrons. *J. Vac. Sci. Technol., B* **2000**, *18*, 3414–3418.
44. Barriet, D. Fluorinated self-assembled monolayers: composition, structure and interfacial properties. *Curr. Opin. Colloid Interface Sci.* **2003**, *8*, 236–242.
45. Frey, S.; Heister, K.; Zharnikov, M.; Grunze, M. Modification of semifluorinated alkanethiolate monolayers by low energy electron irradiation. *Phys. Chem. Chem. Phys.* **2000**, *2*, 1979–1987.
46. Chesneau, F.; Hamoudi, H.; Schüpbach, B.; Terfort, A.; Zharnikov, M. Modification of Self-Assembled Monolayers of Perfluoroterphenyl-Substituted Alkanethiols by Low-Energy Electrons. *J. Phys. Chem. C* **2011**, *115*, 4773–4782.
47. Frese, N.; Scherr, J.; Beyer, A.; Terfort, A.; Gölzhäuser, A.; Hampp, N.; Rhinow, D. Multicomponent patterned ultrathin carbon nanomembranes by laser ablation. *Appl. Surf. Sci.* **2018**, *427*, 126–130.
48. Turchanin, A.; El-Desawy, M.; Gölzhäuser, A. High thermal stability of cross-linked aromatic self-assembled monolayers: Nanopatterning via selective thermal desorption. *Appl. Phys. Lett.* **2007**, *90*,
49. Beyer, A.; Godt, A.; Amin, I.; Nottbohm, C. T.; Schmidt, C.; Zhao, J.; Golzhauser, A. Fully cross-linked and chemically patterned self-assembled monolayers. *Phys. Chem. Chem. Phys.* **2008**, *10*, 7233–7238.

50. Tran, K. T. M.; Nguyen, T. D. Lithography-based methods to manufacture biomaterials at small scales. *J. Sci.: Adv. Mater. Devices* **2017**, *2*, 1–14.
51. Turchanin, A.; Golzhauser, A. Carbon Nanomembranes. *Adv. Mater.* **2016**, *28*, 6075–6103.
52. Kankate, L.; Aguf, A.; Grossmann, H.; Schnietz, M.; Tampe, R.; Turchanin, A.; Golzhauser, A. Vapor Phase Exchange of Self-Assembled Monolayers for Engineering of Biofunctional Surfaces. *Langmuir* **2017**, *33*, 3847–3854.
53. Turchanin, A.; Tinazli, A.; El-Desawy, M.; Großmann, H.; Schnietz, M.; Solak, H. H.; Tampé, R.; Götzhäuser, A. Molecular Self-Assembly, Chemical Lithography, and Biochemical Tweezers: A Path for the Fabrication of Functional Nanometer-Scale Protein Arrays. *Adv. Mater.* **2008**, *20*, 471–477.
54. Meyerbröker, N.; Li, Z.-A.; Eck, W.; Zharnikov, M. Biocompatible Nanomembranes Based on PEGylation of Cross-Linked Self-Assembled Monolayers. *Chem. Mater.* **2012**, *24*, 2965–2972.
55. Chesneau, F.; Terfort, A.; Zharnikov, M. Nickel Deposition on Fluorinated, Aromatic Self-Assembled Monolayers: Chemically Induced Cross-Linking as a Tool for the Preparation of Well-Defined Top Metal Films. *J. Phys. Chem. C* **2014**, *118*, 11763–11773.
56. Kuang, J.; Messersmith, P. B. Universal surface-initiated polymerization of antifouling zwitterionic brushes using a mussel-mimetic peptide initiator. *Langmuir* **2012**, *28*, 7258–7266.
57. Schmelmer, U.; Jordan, R.; Geyer, W.; Eck, W.; Golzhauser, A.; Grunze, M.; Ulman, A. Surface-initiated polymerization on self-assembled monolayers: amplification of patterns on the micrometer and nanometer scale. *Angew. Chem. Int. Ed. Engl.* **2003**, *42*, 559–563.
58. Schmelmer, U.; Paul, A.; Kuller, A.; Steenackers, M.; Ulman, A.; Grunze, M.; Golzhauser, A.; Jordan, R. Nanostructured polymer brushes. *Small* **2007**, *3*, 459–465.
59. Amin, I.; Steenackers, M.; Zhang, N.; Beyer, A.; Zhang, X.; Pirzer, T.; Hugel, T.; Jordan, R.; Golzhauser, A. Polymer carpets. *Small* **2010**, *6*, 1623–1630.
60. Eck, W.; Küller, A.; Grunze, M.; Völkel, B.; Götzhäuser, A. Freestanding Nanosheets from Crosslinked Biphenyl Self-Assembled Monolayers. *Adv. Mater.* **2005**, *17*, 2583–2587.
61. Angelova, P.; Götzhäuser, A. Carbon Nanomembranes. *Physical Sciences Reviews* **2017**, *2*,
62. Schnietz, M.; Turchanin, A.; Nottbohm, C. T.; Beyer, A.; Solak, H. H.; Hinze, P.; Weimann, T.; Golzhauser, A. Chemically functionalized carbon nanosieves with 1-nm thickness. *Small* **2009**, *5*, 2651–2655.
63. Zheng, Z.; Nottbohm, C. T.; Turchanin, A.; Muzik, H.; Beyer, A.; Heilemann, M.; Sauer, M.; Golzhauser, A. Janus nanomembranes: a generic platform for chemistry in two dimensions. *Angew. Chem. Int. Ed. Engl.* **2010**, *49*, 8493–8497.
64. Zheng, Z.; Zhang, X.; Neumann, C.; Emmrich, D.; Winter, A.; Vieker, H.; Liu, W.; Lensen, M.; Golzhauser, A.; Turchanin, A. Hybrid van der Waals heterostructures of zero-dimensional and two-dimensional materials. *Nanoscale* **2015**, *7*, 13393–13397.
65. Turchanin, A. Graphene Growth by Conversion of Aromatic Self-Assembled Monolayers. *Annalen der Physik* **2017**, *529*, 1700168.
66. Yang, Y.; Dementyev, P.; Biere, N.; Emmrich, D.; Stohmann, P.; Korzetz, R.; Zhang, X.; Beyer, A.; Koch, S.; Anselmetti, D.; Golzhauser, A. Rapid Water Permeation Through Carbon Nanomembranes with Sub-Nanometer Channels. *ACS Nano* **2018**, *12*, 4695–4701.

67. Zhang, X.; Marschewski, E.; Penner, P.; Weimann, T.; Hinze, P.; Beyer, A.; Golzhauser, A. Large-Area All-Carbon Nanocapacitors from Graphene and Carbon Nanomembranes. *ACS Nano* **2018**, *12*, 10301–10309.
68. Woszczyna, M.; Winter, A.; Grothe, M.; Willunat, A.; Wundrack, S.; Stosch, R.; Weimann, T.; Ahlers, F.; Turchanin, A. All-carbon vertical van der Waals heterostructures: non-destructive functionalization of graphene for electronic applications. *Adv. Mater.* **2014**, *26*, 4831–4837.
69. Matei, D. G.; Weber, N. E.; Kurasch, S.; Wundrack, S.; Woszczyna, M.; Grothe, M.; Weimann, T.; Ahlers, F.; Stosch, R.; Kaiser, U.; Turchanin, A. Functional single-layer graphene sheets from aromatic monolayers. *Adv. Mater.* **2013**, *25*, 4146–4151.
70. Weber, N. E.; Wundrack, S.; Stosch, R.; Turchanin, A. Direct Growth of Patterned Graphene. *Small* **2016**, *12*, 1440–1445.
71. Turchanin, A.; Beyer, A.; Nottbohm, C. T.; Zhang, X.; Stosch, R.; Sologubenko, A.; Mayer, J.; Hinze, P.; Weimann, T.; Götzhäuser, A. One Nanometer Thin Carbon Nanosheets with Tunable Conductivity and Stiffness. *Adv. Mater.* **2009**, *21*, 1233–1237.
72. Kunjuzwa, N.; Nthunya, L. N.; Nxumalo, E. N.; Mhlanga, S. D. The use of nanomaterials in the synthesis of nanofiber membranes and their application in water treatment. In *Advanced Nanomaterials for Membrane Synthesis and its Applications*, Lau, W.-J.; Ismail, A. F.; Isloor, A.; Al-Ahmed, A., Eds.; Elsevier, 2019, pp 101–125.
73. Dementyev, P.; Wilke, T.; Naberezhnyi, D.; Emmrich, D.; Golzhauser, A. Vapour permeation measurements with free-standing nanomembranes. *Phys. Chem. Chem. Phys.* **2019**, *21*, 15471–15477.
74. Yang, Y.; Hillmann, R.; Qi, Y.; Korzetz, R.; Biere, N.; Emmrich, D.; Westphal, M.; Buker, B.; Hutten, A.; Beyer, A.; Anselmetti, D.; Golzhauser, A. Ultrahigh Ionic Exclusion through Carbon Nanomembranes. *Adv. Mater.* **2020**, *32*, e1907850.
75. Weston, M.; Tjandra, A. D.; Chandrawati, R. Tuning chromatic response, sensitivity, and specificity of polydiacetylene-based sensors. *Polymer Chemistry* **2020**, *11*, 166–183.
76. Reppy, M. A.; Pindzola, B. A. Biosensing with polydiacetylene materials: structures, optical properties and applications. *Chem. Commun. (Camb.)* **2007**, 4317–4338.
77. Batchelder, D. N.; Evans, S. D.; Freeman, T. L.; Haeussling, L.; Ringsdorf, H.; Wolf, H. Self-Assembled Monolayers containing Polydiacetylenes. *J. Am. Chem. Soc.* **1994**, *116*, 1050–1053.
78. Cai, M.; Mowery, M. D.; Menzel, H.; Evans, C. E. Fabrication of Extended Conjugation Length Polymers within Diacetylene Monolayers on Au Surfaces: Influence of UV Exposure Time. *Langmuir* **1999**, *15*, 1215–1222.
79. Takajo, D.; Sudoh, K. Mechanism of Chain Polymerization in Self-Assembled Monolayers of Diacetylene on the Graphite Surface. *Langmuir* **2019**, *35*, 2123–2128.
80. Wu, F.; Bhupathiraju, N. V. S. D. K.; Brown, A.; Liu, Z.; Drain, C. M.; Batteas, J. D. Mechanical and Electronic Properties of Diacetylene and Polydiacetylene Self-Assembled Monolayers on Au(111). *J. Phys. Chem. C* **2020**, *124*, 4081–4089.
81. Menzel, H.; Mowery, M. D.; Cai, M.; Evans, C. E. Vertical Positioning of Internal Molecular Scaffolding within a Single Molecular Layer. *J. Phys. Chem. B* **1998**, *102*, 9550–9556.
82. Kim, T.; Crooks, R. M.; Tsen, M.; Sun, L. Polymeric Self-Assembled Monolayers. 2. Synthesis and Characterization of Self-Assembled Polydiacetylene Mono- and Multilayers. *J. Am. Chem. Soc.* **1995**, *117*, 3963–3967.

83. Kim, T.; Chan, K. C.; Crooks, R. M. Polymeric Self-Assembled Monolayers. 4. Chemical, Electrochemical, and Thermal Stability of ω -Functionalized, Self-Assembled Diacetylenic and Polydiacetylenic Monolayers. *J. Am. Chem. Soc.* **1997**, *119*, 189–193.
84. Ford, J. F.; Vickers, T. J.; Mann, C. K.; Schlenoff, J. B. Polymerization of a Thiol-Bound Styrene Monolayer. *Langmuir* **1996**, *12*, 1944–1946.
85. Chan, K. C.; Kim, T.; Schoer, J. K.; Crooks, R. M. Polymeric Self-Assembled Monolayers. 3. Pattern Transfer by Use of Photolithography, Electrochemical Methods, and an Ultrathin, Self-Assembled Diacetylenic Resist. *J. Am. Chem. Soc.* **1995**, *117*, 5875–5876.
86. Yang, W.; Ella-Menye, J. R.; Liu, S.; Bai, T.; Wang, D.; Yu, Q.; Li, Y.; Jiang, S. Cross-linked carboxybetaine SAMs enable nanoparticles with remarkable stability in complex media. *Langmuir* **2014**, *30*, 2522–2529.
87. Chien, H. W.; Cheng, P. H.; Chen, S. Y.; Yu, J.; Tsai, W. B. Low-fouling and functional poly(carboxybetaine) coating via a photo-crosslinking process. *Biomater Sci* **2017**, *5*, 523–531.
88. Wang, Y.; Sun, Y.; Ding, X.; Liang, J.; Cao, X.; Tian, Z.-Q. A combined electro- and photochemical approach to repeatedly fabricate two-dimensional molecular assemblies. *Electrochim. Acta* **2017**, *246*, 823–829.
89. Olsen, C.; Rowntree, P. A. Bond-selective dissociation of alkanethiol based self-assembled monolayers adsorbed on gold substrates, using low-energy electron beams. *J. Chem. Phys.* **1998**, *108*, 3750–3764.
90. Zharnikov, M.; Geyer, W.; Götzhäuser, A.; Frey, S.; Grunze, M. Modification of alkanethiolate monolayers on Au-substrate by low energy electron irradiation: Alkyl chains and the S/Au interface. *Phys. Chem. Chem. Phys.* **1999**, *1*, 3163–3171.
91. Zharnikov, M.; Frey, S.; Heister, K.; Grunze, M. Modification of Alkanethiolate Monolayers by Low Energy Electron Irradiation: Dependence on the Substrate Material and on the Length and Isotopic Composition of the Alkyl Chains. *Langmuir* **2000**, *16*, 2697–2705.
92. Huels, M. A.; Dugal, P.-C.; Sanche, L. Degradation of functionalized alkanethiolate monolayers by 0–18 eV electrons. *J. Chem. Phys.* **2003**, *118*, 11168–11178.
93. Waske, P. A.; Meyerbröker, N.; Eck, W.; Zharnikov, M. Self-Assembled Monolayers of Cyclic Aliphatic Thiols and Their Reaction toward Electron Irradiation. *J. Phys. Chem. C* **2012**, *116*, 13559–13568.
94. Saha, S.; Bruening, M. L.; Baker, G. L. Facile synthesis of thick films of poly(methyl methacrylate), poly(styrene), and poly(vinyl pyridine) from Au surfaces. *ACS Appl. Mater. Interfaces* **2011**, *3*, 3042–3048.
95. Tkachev, M.; Anand-Kumar, T.; Bitler, A.; Guliamov, R.; Naaman, R. Enabling Long-Term Operation of GaAs-Based Sensors. *Engineering* **2013**, *05*, 1–12.
96. Hou, T.; Greenlief, C. M.; Keller, S. W.; Nelen, L.; Kauffman, J. F. Passivation of GaAs (100) with an Adhesion Promoting Self-Assembled Monolayer. *Chem. Mater.* **1997**, *9*, 3181–3186.
97. Masi, G.; Balbo, A.; Esvan, J.; Monticelli, C.; Avila, J.; Robbiola, L.; Bernardi, E.; Bignozzi, M. C.; Asensio, M. C.; Martini, C.; Chiavari, C. X-ray Photoelectron Spectroscopy as a tool to investigate silane-based coatings for the protection of outdoor bronze: The role of alloying elements. *Appl. Surf. Sci.* **2018**, *433*, 468–479.

98. Sui, W.; Zhao, W.; Zhang, X.; Peng, S.; Zeng, Z.; Xue, Q. Comparative anti-corrosion properties of alkylthiols SAMs and mercapto functional silica sol-gel coatings on copper surface in sodium chloride solution. *J. Sol-Gel Sci. Technol.* **2016**, *80*, 567–578.
99. Sharma, H.; Moumanis, K.; Dubowski, J. J. pH-Dependent Photocorrosion of GaAs/AlGaAs Quantum Well Microstructures. *J. Phys. Chem. C* **2016**, *120*, 26129–26137.
100. Savard, S.; Blanchard, L. P.; Léonard, J.; Prud'homme, R. E. Hydrolysis and condensation of silanes in aqueous solutions. *Polym. Compos.* **1984**, *5*, 242–249.
101. Itoh, M. A Chemical Modification of Alkanethiol Self-Assembled Monolayers with Alkyltrichlorosilanes for the Protection of Copper Against Corrosion. *J. Electrochem. Soc.* **1994**, *141*, 2018–2023.
102. Liu, i.; Ma, K.; Mou, S.; Meng, F. A review of recent power amplifier IC. In *2017 10th Global Symposium on Millimeter-Waves*, 2017, pp 87–91.
103. Asadirad, M.; Rathi, M.; Pouladi, S.; Yao, Y.; Dutta, P.; Shervin, S.; Lee, K. H.; Zheng, N.; Ahrenkiel, P.; Selvamanickam, V.; Ryou, J.-H. III-V thin-film photovoltaic solar cells based on single-crystal-like GaAs grown on flexible metal tapes. In *2016 IEEE 43rd Photovoltaic Specialists Conference (PVSC)*; IEEE: Portland, OR, 2016, pp 1954–1956.
104. Green, M. A.; Hishikawa, Y.; Dunlop, E. D.; Levi, D. H.; Hohl-Ebinger, J.; Ho-Baillie, A. W. Y. Solar cell efficiency tables (version 51). *Prog. Photovoltaics Res. Appl.* **2018**, *26*, 3–12.
105. Sheldon, M. T.; Eisler, C. N.; Atwater, H. A. GaAs Passivation with Trioctylphosphine Sulfide for Enhanced Solar Cell Efficiency and Durability. *Adv Energy Mater* **2012**, *2*, 339–344.
106. Carpenter, M. S.; Melloch, M. R.; Lundstrom, M. S.; Tobin, S. P. Effects of Na₂S and (NH₄)₂S edge passivation treatments on the dark current-voltage characteristics of GaAs p-n diodes. *Appl. Phys. Lett.* **1988**, *52*, 2157–2159.
107. Sheen, C. W.; Shi, J. X.; Maartensson, J.; Parikh, A. N.; Allara, D. L. A new class of organized self-assembled monolayers: alkane thiols on gallium arsenide(100). *J. Am. Chem. Soc.* **1992**, *114*, 1514–1515.
108. Kirchner, C.; George, M.; Stein, B.; Parak, W. J.; Gaub, H. E.; Seitz, M. Corrosion Protection and Long-Term Chemical Functionalization of Gallium Arsenide in an Aqueous Environment. *Adv. Funct. Mater.* **2002**, *12*, 266–276.
109. Lenk, T. J.; Hallmark, V. M.; Hoffmann, C. L.; Rabolt, J. F.; Castner, D. G.; Erdelen, C.; Ringsdorf, H. Structural Investigation of Molecular Organization in Self-Assembled Monolayers of a Semifluorinated Amidethiol. *Langmuir* **1994**, *10*, 4610–4617.
110. Tam-Chang, S.-W.; Biebuyck, H. A.; Whitesides, G. M.; Jeon, N.; Nuzzo, R. G. Self-Assembled Monolayers on Gold Generated from Alkanethiols with the Structure RNHCOCH₂SH. *Langmuir* **1995**, *11*, 4371–4382.
111. Sastry, M.; Patil, V.; Mayya, K. S. Selective Binding of Divalent Cations at the Surface of Self-Assembled Monolayers of an Aromatic Bifunctional Molecule Studied on a Quartz Crystal Microbalance. *J. Phys. Chem. B* **1997**, *101*, 1167–1170.
112. Kim, J. H.; Shin, H. S.; Kim, S. B.; Hasegawa, T. Hydrogen-Bonding Networks of Dialkyl Disulfides Containing the Urea Moiety in Self-Assembled Monolayers. *Langmuir* **2004**, *20*, 1674–1679.

113. Thomas, J. C.; Goronzy, D. P.; Dragomiretskiy, K.; Zosso, D.; Gilles, J.; Osher, S. J.; Bertozzi, A. L.; Weiss, P. S. Mapping Buried Hydrogen-Bonding Networks. *ACS Nano* **2016**, *10*, 5446–5451.
114. Valiokas, R.; Östblom, M.; Svedhem, S.; Svensson, S. C. T.; Liedberg, B. Thermal Stability of Self-Assembled Monolayers: Influence of Lateral Hydrogen Bonding. *J. Phys. Chem. B* **2002**, *106*, 10401–10409.
115. Boal, A. K.; Rotello, V. M. Intra- and Intermonolayer Hydrogen Bonding in Amide-Functionalized Alkanethiol Self-Assembled Monolayers on Gold Nanoparticles. *Langmuir* **2000**, *16*, 9527–9532.
116. Carey, R. I.; Folkers, J. P.; Whitesides, G. M. Self-Assembled Monolayers Containing ω -Mercaptoalkyl Boronic Acids Adsorbed onto Gold Form a Highly Cross-Linked, Thermally Stable Borate Glass Surface. *Langmuir* **1994**, *10*, 2228–2234.
117. Fabre, B.; Hauquier, F. Boronic Acid-Functionalized Oxide-Free Silicon Surfaces for the Electrochemical Sensing of Dopamine. *Langmuir* **2017**, *33*, 8693–8699.
118. Bishop, C. A. Chapter 11 Polymer Coating Basic Information. In *Vacuum Deposition Onto Webs, Films and Foils (Third Edition)*, Bishop, C. A., Ed.; William Andrew Publishing: Boston, 2015, pp 221–239.
119. Grainger, D. W.; Stewart, C. W. Fluorinated Coatings and Films: Motivation and Significance. *ACS Symp. Ser.* **2001**, *787*, 1–14.
120. Plunkett, R. J. Tetrafluoroethylene Polymers US 2,230,654, February 4, 1941.
121. Patrick, C. R. Thermal Stability of Polytetrafluoroethylene. *Nature* **1958**, *181*, 698–698.
122. Lee, S.; Park, J. S.; Lee, T. R. The wettability of fluoropolymer surfaces: influence of surface dipoles. *Langmuir* **2008**, *24*, 4817–4826.
123. Jones, B. Fluoropolymers for Coating Applications. *J. Coat. Technol. Res.* **2008**, *5*, 44–48.
124. Yamamoto, T. Computer modeling of polymer crystallization – Toward computer-assisted materials' design. *Polymer* **2009**, *50*, 1975–1985.
125. Brown, E. N.; Rae, P. J.; Dattelbaum, D. M.; Clausen, B.; Brown, D. W. In-situ Measurement of Crystalline Lattice Strains in Polytetrafluoroethylene. *Experimental Mechanics* **2007**, *48*, 119–131.
126. Brown, E. N.; Dattelbaum, D. M. The Role of Crystalline Phase on Fracture and Microstructure Evolution of Polytetrafluoroethylene (PTFE). *Polymer* **2005**, *46*, 3056–3068.
127. Brown, E. N.; Trujillo, C. P.; Gray, G. T.; Rae, P. J.; Bourne, N. K. Soft Recovery of Polytetrafluoroethylene Shocked Through the Crystalline Phase II-III Transition. *J. Appl. Phys.* **2007**, *101*, 024916.
128. Clark, E. S. The molecular Conformations of Polytetrafluoroethylene: Forms II and IV. *Polymer* **1999**, *40*, 4659–4665.
129. Bunn, C. W.; Howells, E. R. Structures of Molecules and Crystals of Fluoro-Carbons. *Nature* **1954**, *174*, 549–551.
130. Schrauwen, B. A. G.; Janssen, R. P. M.; Govaert, L. E.; Meijer, H. E. H. Intrinsic deformation behavior of semicrystalline polymers. *Macromolecules* **2004**, *37*, 6069–6078.
131. Allam, I. M. Solid Lubricants for Applications at Elevated-Temperatures - a Review. *J. Mater. Sci.* **1991**, *26*, 3977–3984.
132. Zhang, X.; Shi, F.; Niu, J.; Jiang, Y. G.; Wang, Z. Q. Superhydrophobic Surfaces: From Structural Control to Functional Application. *J. Mater. Chem.* **2008**, *18*, 621–633.

133. Yuan, Y.; Lee, T. R. Contact Angle and Wetting Properties. In *Surface Science Techniques*, Bracco, G.; Holst, B., Eds.; Springer Berlin Heidelberg: Berlin, Heidelberg, 2013, pp 3–34.
134. Andena, L.; Rink, M.; Polastri, F. Simulation of PTFE sintering: Thermal stresses and deformation behavior. *Polym. Eng. Sci.* **2004**, *44*, 1368–1378.
135. Holmes-Farley, S. R.; Bain, C. D.; Whitesides, G. M. Wetting of Functionalized Polyethylene Film Having Ionizable Organic Acids and Bases at the Polymer-Water Interface: Relations Between Functional Group Polarity, Extent of Ionization, and Contact Angle with Water. *Langmuir* **1988**, *4*, 921–937.
136. Grundke, K.; Poschel, K.; Synytska, A.; Frenzel, R.; Drechsler, A.; Nitschke, M.; Cordeiro, A. L.; Uhlmann, P.; Welzel, P. B. Experimental Studies of Contact Angle Hysteresis Phenomena on Polymer Surfaces - Toward the Understanding and Control of Wettability for Different Applications. *Adv. Colloid Interface Sci.* **2015**, *222*, 350–376.
137. Sedev, R. V.; Petrov, J. G.; Neumann, A. W. Effect of Swelling of a Polymer Surface on Advancing and Receding Contact Angles. *J. Colloid Interface Sci.* **1996**, *180*, 36–42.
138. Erbil, H. Y. The Debate on the Dependence of Apparent Contact Angles on Drop Contact Area or Three-Phase Contact Line: A Review. *Surf. Sci. Rep.* **2014**, *69*, 325–365.
139. Podestà, A.; Fantoni, G.; Milani, P.; Guida, C.; Volponi, S. Nanotribological characterization of industrial polytetrafluorethylene-based coatings by atomic force microscopy. *Thin Solid Films* **2002**, *419*, 154–159.
140. Perry, S. S.; Tysoe, W. T. Frontiers of fundamental tribological research. *Tribol. Lett.* **2005**, *19*, 151–161.
141. Myshkin, N. K.; Petrokovets, M. I.; Kovalev, A. V. Tribology of polymers: Adhesion, friction, wear, and mass-transfer. *Tribology International* **2005**, *38*, 910–921.
142. Telegdi, J.; Rigó, T.; Kálmán, E. Nanolayer Barriers for Inhibition of Copper Corrosion. *Corros. Eng., Sci. Technol.* **2013**, *39*, 65–70.
143. Halik, M.; Klauk, H.; Zschieschang, U.; Schmid, G.; Dehm, C.; Schutz, M.; Maisch, S.; Effenberger, F.; Brunnbauer, M.; Stellacci, F. Low-Voltage Organic Transistors with an Amorphous Molecular Gate Dielectric. *Nature* **2004**, *431*, 963–966.
144. Senaratne, W.; Andruzzi, L.; Ober, C. K. Self-Assembled Monolayers and Polymer Brushes in Biotechnology: Current Applications and Future Perspectives. *Biomacromolecules* **2005**, *6*, 2427–2448.
145. Mir, M.; Alvarez, M.; Azzaroni, O.; Knoll, W. Comparison of Different Supramolecular Architectures for Oligonucleotide Biosensing. *Langmuir* **2008**, *24*, 13001–13006.
146. Zheng, H.; Zhang, F.; Zhou, N.; Sun, M.; Li, X.; Xiao, Y.; Wang, S. Self-assembled monolayer-modified ITO for efficient organic light-emitting diodes: The impact of different self-assemble monolayers on interfacial and electroluminescent properties. *Organic Electronics* **2018**, *56*, 89–95.
147. Smith, D. L.; Wysocki, V. H.; Colorado, R.; Shmakova, O. E.; Graupe, M.; Lee, T. R. Low-Energy Ion–Surface Collisions Characterize Alkyl- and Fluoroalkyl-Terminated Self-Assembled Monolayers on Gold. *Langmuir* **2002**, *18*, 3895–3902.
148. Colorado, R.; Lee, T. R. Wettabilities of Self-Assembled Monolayers on Gold Generated from Progressively Fluorinated Alkanethiols. *Langmuir* **2003**, *19*, 3288–3296.

149. Graupe, M.; Koini, T.; Wang, V. Y.; Nassif, G. M.; Colorado, R.; Villazana, R. J.; Dong, H.; Miura, Y. F.; Shmakova, O. E.; Lee, T. R. Terminally perfluorinated long-chain alkanethiols. *J. Fluorine Chem.* **1999**, *93*, 107–115.
150. Frey, S.; Heister, K.; Zharnikov, M.; Grunze, M.; Tamada, K.; Colorado, R.; Graupe, M.; Shmakova, O. E.; Lee, T. R. Structure of Self-Assembled Monolayers of Semifluorinated Alkanethiols on Gold and Silver Substrates. *Isr. J. Chem.* **2000**, *40*, 81–97.
151. Pujari, S. P.; Scheres, L.; Weidner, T.; Baio, J. E.; Stuart, M. A.; van Rijn, C. J.; Zuilhof, H. Covalently Attached Organic Monolayers onto Silicon Carbide from 1-Alkynes: Molecular Structure and Tribological Properties. *Langmuir* **2013**, *29*, 4019–4031.
152. Barriet, D.; Chinwangso, P.; Lee, T. R. Can Cyclopropyl-Terminated Self-Assembled Monolayers on Gold Be Used to Mimic the Surface of Polyethylene? *ACS Applied Materials Interfaces* **2010**, *2*, 1254–1265.
153. Fukushima, H.; Seki, S.; Nishikawa, T.; Takiguchi, H.; Tamada, K.; Abe, K.; Colorado, R.; Graupe, M.; Shmakova, O. E.; Lee, T. R. Microstructure, Wettability, and Thermal Stability of Semifluorinated Self-Assembled Monolayers (SAMs) on Gold. *J. Phys. Chem. B* **2000**, *104*, 7417–7423.
154. Colorado Jr, R.; Lee, T. R. Physical organic probes of interfacial wettability reveal the importance of surface dipole effects. *J. Phys. Org. Chem.* **2000**, *13*, 796–807.
155. O'Hagan, D. Understanding organofluorine chemistry. An introduction to the C-F bond. *Chem. Soc. Rev.* **2008**, *37*, 308–319.
156. Bondi, A. Van Der Waals Volumes and Radii. *J. Phys. Chem.* **1964**, *68*, 441–451.
157. Zenasni, O.; Jamison, A. C.; Lee, T. R. The impact of fluorination on the structure and properties of self-assembled monolayer films. *Soft Matter* **2013**, *9*, 6356–6370.
158. Chidsey, C. E. D.; Loiacono, D. N. Chemical Functionality in Self-Assembled Monolayers - Structural and Electrochemical Properties. *Langmuir* **1990**, *6*, 682–691.
159. Zenasni, O.; Jamison, A. C.; Marquez, M. D.; Lee, T. R. Self-assembled monolayers on gold generated from terminally perfluorinated alkanethiols bearing propyl vs. ethyl hydrocarbon spacers. *J. Fluorine Chem.* **2014**, *168*, 128–136.
160. Laibinis, P. E.; Whitesides, G. M.; Allara, D. L.; Tao, Y. T.; Parikh, A. N.; Nuzzo, R. G. Comparison of the Structures and Wetting Properties of Self-Assembled Monolayers of *n*-Alkanethiols on the Coinage Metal Surfaces, Copper, Silver, and Gold. *J. Am. Chem. Soc.* **1991**, *113*, 7152–7167.
161. Vickerman, J. C.; Gilmore, I. S. *Surface Analysis—The Principal Techniques*; 2nd ed.; John Wiley & Sons: Chichester, 2009.
162. Hutt, D. A.; Leggett, G. J. Influence of Adsorbate Ordering on Rates of UV Photooxidation of Self-Assembled Monolayers. *J. Phys. Chem.* **1996**, *100*, 6657–6662.
163. Castner, D. G.; Hinds, K.; Grainger, D. W. X-ray photoelectron spectroscopy sulfur 2p study of organic thiol and disulfide binding interactions with gold surfaces. *Langmuir* **1996**, *12*, 5083–5086.
164. Mancheno-Posso, P.; Muscat, A. J. Self-assembly of alkanethiolates directs sulfur bonding with GaAs(100). *Appl. Surf. Sci.* **2017**, *397*, 1–12.

165. Park, J. S.; Vo, A. N.; Barriet, D.; Shon, Y. S.; Lee, T. R. Systematic Control of the Packing Density of Self-Assembled Monolayers Using Bidentate and Tridentate Chelating Alkanethiols. *Langmuir* **2005**, *21*, 2902–2911.
166. Colorado, R.; Lee, T. R. Attenuation Lengths of Photoelectrons in Fluorocarbon Films. *J. Phys. Chem. B* **2003**, *107*, 10216–10220.
167. Zenasni, O.; Marquez, M. D.; Jamison, A. C.; Lee, H. J.; Czader, A.; Lee, T. R. Inverted Surface Dipoles in Fluorinated Self-Assembled Monolayers. *Chem. Mater.* **2015**, *27*, 7433–7446.
168. Porter, M. D.; Bright, T. B.; Allara, D. L.; Chidsey, C. E. D. Spontaneously Organized Molecular Assemblies. 4. Structural Characterization of *n*-Alkyl Thiol Monolayers on Gold by Optical Ellipsometry, Infrared Spectroscopy, and Electrochemistry. *J. Am. Chem. Soc.* **1987**, *109*, 3559–3568.
169. MacPhail, R. A.; Strauss, H. L.; Snyder, R. G.; Elliger, C. A. Carbon-Hydrogen Stretching Modes and the Structure of *n*-Alkyl Chains. 2. Long, All-Trans Chains. *J. Phys. Chem.* **1984**, *88*, 334–341.
170. Snyder, R. G.; Strauss, H. L.; Elliger, C. A. Carbon-Hydrogen Stretching Modes and the Structure of *n*-Alkyl Chains. 1. Long, Disordered Chains. *J. Phys. Chem.* **1982**, *86*, 5145–5150.
171. Liu, D.; He, Z.; Su, Y.; Diao, Y.; Mannsfeld, S. C. B.; Bao, Z.; Xu, J.; Miao, Q. Self-Assembled Monolayers of Cyclohexyl-Terminated Phosphonic Acids as a General Dielectric Surface for High-Performance Organic Thin-Film Transistors. *Adv. Mater.* **2014**, *26*, 7190–7196.
172. Smallwood, I. M. *Handbook of Organic Solvent Properties*; John Wiley & Sons:: New York, 1996.
173. Wohlfarth, C. Surface tension of N-methylformamide. In *Supplement to IV/16*, Lechner, M. D., Ed.; Springer Berlin Heidelberg: Berlin, Heidelberg, 2008, pp 56–56.
174. Fowkes, F. M.; Riddle, F. L.; Pastore, W. E.; Weber, A. A. Interfacial Interactions Between Self-Associated Polar Liquids and Squalane Used to Test Equations for Solid Liquid Interfacial Interactions. *Colloids Surf.* **1990**, *43*, 367–387.
175. Shon, Y. S.; Lee, S.; Colorado, R.; Perry, S. S.; Lee, T. R. Spiroalkanedithiol-Based Sams Reveal Unique Insight Into the Wettabilities and Frictional Properties of Organic Thin Films. *J. Am. Chem. Soc.* **2000**, *122*, 7556–7563.
176. Ewbank, J. D.; Kirsch, G.; Schafer, L. Electron-Diffraction Study of Hydrogen Isotope-Effects in Cyclohexane. *J. Mol. Struct.* **1976**, *31*, 39–45.
177. Aggarwal, S. L.; Sweeting, O. J. Polyethylene: Preparation, Structure, and Properties. *Chem. Rev.* **1957**, *57*, 665–742.
178. Cui, M.; Wang, Y.; Wang, H.; Wu, Y.; Luo, X. A label-free electrochemical DNA biosensor for breast cancer marker BRCA1 based on self-assembled antifouling peptide monolayer. *Sensors and Actuators B: Chemical* **2017**, *244*, 742–749.
179. Taufik, S.; Barfidokht, A.; Alam, M. T.; Jiang, C.; Parker, S. G.; Gooding, J. J. An antifouling electrode based on electrode–organic layer–nanoparticle constructs: Electrodeposited organic layers versus self-assembled monolayers. *J. Electroanal. Chem.* **2016**, *779*, 229–235.
180. Yapu, Z. Stiction and anti-stiction in MEMS and NEMS. *Acta Mechanica Sinica* **2003**, *19*, 1–10.
181. Marquez, M. D.; Zenasni, O.; Jamison, A. C.; Lee, T. R. Homogeneously Mixed Monolayers: Emergence of Compositionally Conflicted Interfaces. *Langmuir* **2017**, *33*, 8839–8855.

182. Folkers, J. P.; Laibinis, P. E.; Whitesides, G. M. Self-assembled monolayers of alkanethiols on gold: comparisons of monolayers containing mixtures of short- and long-chain constituents with methyl and hydroxymethyl terminal groups. *Langmuir* **1992**, *8*, 1330–1341.
183. Folkers, J. P.; Laibinis, P. E.; Whitesides, G. M.; Deutch, J. Phase behavior of two-component self-assembled monolayers of alkanethiolates on gold. *J. Phys. Chem.* **1994**, *98*, 563–571.
184. Smith, R. K.; Reed, S. M.; Lewis, P. A.; Monnell, J. D.; Clegg, R. S.; Kelly, K. F.; Bumm, L. A.; Hutchison, J. E.; Weiss, P. S. Phase Separation within a Binary Self-Assembled Monolayer on Au{111} Driven by an Amide-Containing Alkanethiol. *J. Phys. Chem. B* **2001**, *105*, 1119–1122.
185. Stranick, S. J.; Parikh, A. N.; Tao, Y. T.; Allara, D. L.; Weiss, P. S. Phase Separation of Mixed-Composition Self-Assembled Monolayers into Nanometer Scale Molecular Domains. *J. Phys. Chem.* **1994**, *98*, 7636–7646.
186. Lee, H. J.; Jamison, A. C.; Lee, T. R. Two Are Better than One: Bidentate Adsorbates Offer Precise Control of Interfacial Composition and Properties. *Chem. Mater.* **2016**, *28*, 5356–5364.
187. Kissa, E. *Fluorinated Surfactants and Repellents, Second Edition*; Taylor & Francis: 2001.
188. Banks, R. E.; Smart, B. E.; Tatlow, J. C. *Organofluorine Chemistry: Principles and Commercial Applications*; Springer: 1994.
189. Arima, Y.; Iwata, H. Effect of wettability and surface functional groups on protein adsorption and cell adhesion using well-defined mixed self-assembled monolayers. *Biomaterials* **2007**, *28*, 3074–3082.
190. Balamurugan, S.; Ista, L. K.; Yan, J.; Lopez, G. P.; Fick, J.; Himmelhaus, M.; Grunze, M. Reversible protein adsorption and bioadhesion on monolayers terminated with mixtures of oligo(ethylene glycol) and methyl groups. *J. Am. Chem. Soc.* **2005**, *127*, 14548–14549.
191. Liu, J.; Kind, M.; Schupbach, B.; Kafer, D.; Winkler, S.; Zhang, W.; Terfort, A.; Woll, C. Triptycene-terminated thiolate and selenolate monolayers on Au(111). *Beilstein J. Nanotechnol.* **2017**, *8*, 892–905.
192. Dichiarante, V.; Tirota, I.; Catalano, L.; Terraneo, G.; Raffaini, G.; Chierotti, M. R.; Gobetto, R.; Baldelli Bombelli, F.; Metrangolo, P. Superfluorinated and NIR-luminescent gold nanoclusters. *Chem. Commun.* **2017**, *53*, 621–624.
193. Fenwick, O.; Van Dyck, C.; Murugavel, K.; Cornil, D.; Reinders, F.; Haar, S.; Mayor, M.; Cornil, J.; Samorì, P. Modulating the charge injection in organic field-effect transistors: fluorinated oligophenyl self-assembled monolayers for high work function electrodes. *J. Mater. Chem. C* **2015**, *3*, 3007–3015.
194. Hsu, S. M.; Lin, Y. C.; Chang, J. W.; Liu, Y. H.; Lin, H. C. Intramolecular interactions of a phenyl/perfluorophenyl pair in the formation of supramolecular nanofibers and hydrogels. *Angew. Chem. Int. Ed. Engl.* **2014**, *53*, 1921–1927.
195. Lee, S.; Puck, A.; Graupe, M.; Colorado, R.; Shon, Y.-S.; Lee, T. R.; Perry, S. S. Structure, Wettability, and Frictional Properties of Phenyl-Terminated Self-Assembled Monolayers on Gold. *Langmuir* **2001**, *17*, 7364–7370.
196. Moulder, J. F.; Chastain, J.; Sobol, P. E.; Bomben, K. D. *Handbook of x-ray photoelectron spectroscopy*; Perkin-Elmer: Eden Prairie: MN, 1992.
197. Rittikulsittichai, S.; Park, C. S.; Jamison, A. C.; Rodriguez, D.; Zenasni, O.; Lee, T. R. Bidentate Aromatic Thiols on Gold: New Insight Regarding the Influence of Branching on the Structure,

- Packing, Wetting, and Stability of Self-Assembled Monolayers on Gold Surfaces. *Langmuir* **2017**, *33*, 4396–4406.
198. Matthew, J. *Surface analysis by Auger and x-ray photoelectron spectroscopy*; John Wiley & Sons, Ltd: 2004; Vol. 36. p. 1647–1647.
 199. Kang, H.; Lee, H.; Kang, Y.; Hara, M.; Noh, J. Two-dimensional ordering of benzenethiol self-assembled monolayers guided by displacement of cyclohexanethiols on Au(111). *Chem. Commun. (Camb.)* **2008**, 5197–5199.
 200. Mezour, M. A.; Voznyy, O.; Sargent, E. H.; Lennox, R. B.; Perepichka, D. F. Controlling C₆₀ Organization through Dipole-Induced Band Alignment at Self-Assembled Monolayer Interfaces. *Chem. Mater.* **2016**, *28*, 8322–8329.
 201. Liu, Z.; Bol, A. A.; Haensch, W. Large-scale graphene transistors with enhanced performance and reliability based on interface engineering by phenylsilane self-assembled monolayers. *Nano Lett.* **2011**, *11*, 523–528.
 202. Chen, H.; Guo, X. Unique role of self-assembled monolayers in carbon nanomaterial-based field-effect transistors. *Small* **2013**, *9*, 1144–1159.
 203. Chinwangso, P.; St Hill, L. R.; Marquez, M. D.; Lee, T. R. Unsymmetrical Spiroalkanedithiols Having Mixed Fluorinated and Alkyl Tailgroups of Varying Length: Film Structure and Interfacial Properties. *Molecules* **2018**, *23*,
 204. Yang, Y.; Jamison, A. C.; Barriet, D.; Lee, T. R.; Ruths, M. Odd–Even Effects in the Friction of Self-Assembled Monolayers of Phenyl-Terminated Alkanethiols in Contacts of Different Adhesion Strengths. *J. Adhes. Sci. Technol.* **2010**, *24*, 2511–2529.
 205. Bai, J.; Cameron, J.; Wang, Q.; Yan, C.; Yao, C.; Chen, M.; Meng, H.; He, C.; Xu, X. Self-assembled monolayers induced performance difference in organic single crystal field-effect transistors. *Organic Electronics* **2019**, *75*,
 206. Jung, M.-H.; Choi, H.-S. Characterization of octadecyltrichlorosilane self-assembled monolayers on silicon (100) surface. *Korean J. Chem. Eng.* **2010**, *26*, 1778–1784.
 207. Belghachi, A.; Helmaoui, A.; Cheknane, A. High efficiency all-GaAs solar cell. *Prog. Photovoltaics Res. Appl.* **2010**, *18*, 79–82.
 208. Dutta, P.; Rathi, M.; Ahrenkiel, P.; Gao, Y.; Mehrotra, A.; Galstyan, E.; Iliev, M.; Makarenko, B.; Forrest, R.; Freundlich, A.; Selvamanickam, V. Epitaxial thin film GaAs deposited by MOCVD on Low-Cost, Flexible Substrates for High Efficiency Photovoltaics. *Ieee Phot Spec Conf* **2013**, 3393–3396.
 209. Dietrich, C. P.; Fiore, A.; Thompson, M. G.; Kamp, M.; Höfling, S. GaAs integrated quantum photonics: Towards compact and multi-functional quantum photonic integrated circuits. *Laser Photonics Rev* **2016**, *10*, 870–894.
 210. Cheney, D.; Douglas, E.; Liu, L.; Lo, C.-F.; Gila, B.; Ren, F.; Pearton, S. Degradation Mechanisms for GaN and GaAs High Speed Transistors. *Materials* **2012**, *5*, 2498–2520.
 211. Chen, W.; Wang, Z.; Chen, X.; Zhang, S. Radio frequency power amplifier for wireless communication. In *Microwave Wireless Communications*, 2016, pp 261–300.
 212. Green, M. A.; Dunlop, E. D.; Hohl-Ebinger, J.; Yoshita, M.; Kopidakis, N.; Ho-Baillie, A. W. Y. Solar cell efficiency tables (Version 55). *Prog. Photovoltaics Res. Appl.* **2019**, *28*, 3–15.

213. Morales-Acevedo, A. Effective absorption coefficient for graded band-gap semiconductors and the expected photocurrent density in solar cells. *Sol. Energy Mater. Sol. Cells* **2009**, *93*, 41–44.
214. Pouladi, S.; Rathi, M.; Khatiwada, D.; Asadirad, M.; Oh, S. K.; Dutta, P.; Yao, Y.; Gao, Y.; Sun, S.; Li, Y.; Shervin, S.; Lee, K.-H.; Selvamanickam, V.; Ryou, J.-H. High-efficiency flexible III-V photovoltaic solar cells based on single-crystal-like thin films directly grown on metallic tapes. *Prog. Photovoltaics Res. Appl.* **2019**, *27*, 30–36.
215. Sun, Y.; Faucher, J.; Jung, D.; Vaisman, M.; McPheeters, C.; Sharps, P.; Perl, E.; Simon, J.; Steiner, M.; Friedman, D.; Lee, M. L. Thermal stability of GaAs solar cells for high temperature applications. In *2016 IEEE 43rd Photovoltaic Specialists Conference (PVSC)*: Portland, OR, 2016, pp 2385–2388.
216. Bailey, S.; Raffaele, R. Space Solar Cells and Arrays. In *Handbook of Photovoltaic Science and Engineering*, 2005, pp 413–448.
217. Han, N.; Yang, Z. X.; Wang, F.; Dong, G.; Yip, S.; Liang, X.; Hung, T. F.; Chen, Y.; Ho, J. C. High-Performance GaAs Nanowire Solar Cells for Flexible and Transparent Photovoltaics. *ACS Appl. Mater. Interfaces* **2015**, *7*, 20454–20459.
218. Gérard, I.; Debiemme-Chouvy, C.; Vigneron, J.; Bellenger, F.; Kostelitz, S.; Etcheberry, A. Local oxide growth on the n-GaAs surface studied by small area XPS. *Surf. Sci.* **1999**, *433-435*, 131–135.
219. Feng, L.; Zhang, L. D.; Liu, H.; Gao, X.; Miao, Z.; Cheng, H. C.; Wang, L.; Niu, S. Characterization Study of Native Oxides on GaAs(100) Surface by XPS. *Proc Spie* **2013**, *8912*, 89120N–89120N.
220. Liu, Z.; Sun, Y.; Machuca, F.; Pianetta, P.; Spicer, W. E.; Pease, R. F. W. Preparation of clean GaAs(100) studied by synchrotron radiation photoemission. *J. Vac. Sci. Technol., A* **2003**, *21*, 212–218.
221. Zhou, L.; Bo, B.; Yan, X.; Wang, C.; Chi, Y.; Yang, X. Brief Review of Surface Passivation on III-V Semiconductor. *Crystals* **2018**, *8*,
222. Brennan, B.; Milojevic, M.; Hinkle, C. L.; Aguirre-Tostado, F. S.; Hughes, G.; Wallace, R. M. Optimisation of the ammonium sulphide (NH₄)₂S passivation process on In_{0.53}Ga_{0.47}As. *Appl. Surf. Sci.* **2011**, *257*, 4082–4090.
223. Lunt, S. R. Passivation of GaAs surface recombination with organic thiols. *J. Vac. Sci. Technol., B* **1991**, *9*, 2333-2336.
224. Zhou, L.; Chu, X.; Chi, Y.; Yang, X. Property Improvement of GaAs Surface by 1-Octadecanethiol Passivation. *Crystals* **2019**, *9*,
225. Park, C. S.; Colorado, R.; Jamison, A. C.; Lee, T. R. Thiol-Based Self-Assembled Monolayers: Formation, Organization, and the Role of Adsorbate Structure. In *Reference Module in Materials Science and Materials Engineering*, 2016.
226. Chinwangso, P.; Jamison, A. C.; Lee, T. R. Multidentate adsorbates for self-assembled monolayer films. *Acc. Chem. Res.* **2011**, *44*, 511–519.
227. Rittikulsittichai, S.; Park, C. S.; Marquez, M. D.; Jamison, A. C.; Frank, T.; Wu, C. H.; Wu, J. I.; Lee, T. R. Inhibiting Reductive Elimination as an Intramolecular Disulfide Dramatically Enhances the Thermal Stability of SAMs on Gold Derived from Bidentate Adsorbents. *Langmuir* **2018**, *34*, 6645–6652.

228. Lee, H. J.; Jamison, A. C.; Yuan, Y.; Li, C. H.; Rittikulsittichai, S.; Rusakova, I.; Lee, T. R. Robust carboxylic acid-terminated organic thin films and nanoparticle protectants generated from bidentate alkanethiols. *Langmuir* **2013**, *29*, 10432–10439.
229. Lu, H.; Zeysing, D.; Kind, M.; Terfort, A.; Zharnikov, M. Structure of Self-Assembled Monolayers of Partially Fluorinated Alkanethiols with a Fluorocarbon Part of Variable Length on Gold Substrate. *J. Phys. Chem. C* **2013**, *117*, 18967–18979.
230. Tamada, K.; Ishida, T.; Knoll, W.; Fukushima, H.; Colorado, R.; Graupe, M.; Shmakova, O. E.; Lee, T. R. Molecular Packing of Semifluorinated Alkanethiol Self-Assembled Monolayers on Gold: Influence of Alkyl Spacer Length. *Langmuir* **2001**, *17*, 1913–1921.
231. Cornejo, C. E.; Bertram, M. E.; Diaz, T. C.; Narayan, S. R.; Ram, S.; Kavanagh, K. L.; Herbots, N.; Day, J. M.; Ark, F. J.; Dhamdhere, A.; Culbertson, R. J.; Islam, R. Measuring Surface Energies of GaAs (100) and Si (100) by Three Liquid Contact Angle Analysis (3LCAA) for Heterogeneous Nano-Bonding™. *MRS Advances* **2018**, *3*, 3403–3411.
232. Lu, H.; Kind, M.; Terfort, A.; Zharnikov, M. Structure of Self-Assembled Monolayers of Partially Fluorinated Alkanethiols on GaAs(001) Substrates. *J. Phys. Chem. C* **2013**, *117*, 26166–26178.
233. Lu, H.; Zharnikov, M. Structure-Building Forces in Biphenyl-Substituted Alkanethiolate Self-Assembled Monolayers on GaAs(001): The Effect of the Bending Potential. *J. Phys. Chem. C* **2015**, *119*, 27401–27409.
234. Shaporenko, A.; Adlkofer, K.; Johansson, L. S. O.; Ulman, A.; Grunze, M.; Tanaka, M.; Zharnikov, M. Spectroscopic Characterization of 4'-Substituted Aromatic Self-Assembled Monolayers on GaAs(100) Surface. *J. Phys. Chem. B* **2004**, *108*, 17964–17972.
235. McGuinness, C. L.; Shaporenko, A.; Zharnikov, M.; Walker, A. V.; Allara, D. L. Molecular Self-Assembly at Bare Semiconductor Surfaces: Investigation of the Chemical and Electronic Properties of the Alkanethiolate–GaAs(001) Interface. *J. Phys. Chem. C* **2007**, *111*, 4226–4234.
236. McGuinness, C. L.; Shaporenko, A.; Mars, C. K.; Uppili, S.; Zharnikov, M.; Allara, D. L. Molecular self-assembly at bare semiconductor surfaces: preparation and characterization of highly organized octadecanethiolate monolayers on GaAs(001). *J. Am. Chem. Soc.* **2006**, *128*, 5231–5243.
237. McGuinness, C. L.; Blasini, D.; Masejewski, J. P.; Uppili, S.; Cabarcos, O. M.; Smilgies, D.; Allara, D. L. Molecular self-assembly at bare semiconductor surfaces: characterization of a homologous series of n-alkanethiolate monolayers on GaAs(001). *ACS Nano* **2007**, *1*, 30–49.
238. Wieliczka, D. M.; Ding, X.; Dubowski, J. J. X-ray photoelectron spectroscopy study of self-assembled monolayers of alkanethiols on (001) GaAs. *J. Vac. Sci. Technol., A* **2006**, *24*, 1756–1759.
239. Budz, H. A.; Biesinger, M. C.; LaPierre, R. R. Passivation of GaAs by octadecanethiol self-assembled monolayers deposited from liquid and vapor phases. *J. Vac. Sci. Technol., B* **2009**, *27*, 637–648.
240. Voznyy, O.; Dubowski, J. J. Structure of thiol self-assembled monolayers commensurate with the GaAs (001) surface. *Langmuir* **2008**, *24*, 13299–13305.
241. Shaporenko, A.; Adlkofer, K.; Johansson, L. S. O.; Tanaka, M.; Zharnikov, M. Functionalization of GaAs Surfaces with Aromatic Self-Assembled Monolayers: A Synchrotron-Based Spectroscopic Study. *Langmuir* **2003**, *19*, 4992–4998.
242. Nagatsuma, T.; Kasamatsu, A. In *Terahertz Communications for Space Applications*, 2018 Asia-Pacific Microwave Conference (APMC), 6-9 Nov. 2018; 2018, pp 73–75.

243. Fukuda, G.; Yoshida, S.; Kobayashi, Y.; Noji, T.; Tashiro, S.; Kawasaki, S. In *Cryogenic GaAs high gain and low-noise amplifier module for radio astronomy*, 2012 Asia Pacific Microwave Conference Proceedings, 4-7 Dec. 2012; 2012, pp 905–907.
244. Camarchia, V.; Pirola, M.; Quaglia, R.; Jee, S.; Cho, Y.; Kim, B. The Doherty Power Amplifier: Review of Recent Solutions and Trends. *IEEE Trans. Microwave Theory Tech.* **2015**, *63*, 559–571.
245. Ye, P. D.; Wilk, G. D.; Yang, B.; Kwo, J.; Chu, S. N. G.; Nakahara, S.; Gossmann, H. J. L.; Mannaerts, J. P.; Hong, M.; Ng, K. K.; Bude, J. GaAs metal–oxide–semiconductor field-effect transistor with nanometer-thin dielectric grown by atomic layer deposition. *Appl. Phys. Lett.* **2003**, *83*, 180–182.
246. Yoon, J.; Jo, S.; Chun, I. S.; Jung, I.; Kim, H. S.; Meitl, M.; Menard, E.; Li, X.; Coleman, J. J.; Paik, U.; Rogers, J. A. GaAs photovoltaics and optoelectronics using releasable multilayer epitaxial assemblies. *Nature* **2010**, *465*, 329–333.
247. Seisyan, R. P. Nanolithography in microelectronics: A review. *Tech. Phys.* **2011**, *56*, 1061–1073.
248. Acikgoz, C.; Hempenius, M. A.; Huskens, J.; Vancso, G. J. Polymers in conventional and alternative lithography for the fabrication of nanostructures. *Eur. Polym. J.* **2011**, *47*, 2033–2052.
249. Chen, Y. Applications of nanoimprint lithography/hot embossing: a review. *Appl Phys a-Mater* **2015**, *121*, 451–465.
250. Vogler, M.; Wiedenberg, S.; Mühlberger, M.; Bergmair, I.; Glinsner, T.; Schmidt, H.; Kley, E.-B.; Grützner, G. Development of a novel, low-viscosity UV-curable polymer system for UV-nanoimprint lithography. *Microelectron. Eng.* **2007**, *84*, 984–988.
251. Qin, D.; Xia, Y.; Whitesides, G. M. Soft lithography for micro- and nanoscale patterning. *Nat. Protoc.* **2010**, *5*, 491–502.
252. Kao, P. C.; Chu, S. Y.; Chen, T. Y.; Zhan, C. Y.; Hong, F. C.; Chang, C. Y.; Hsu, L. C.; Liao, W. C.; Hon, M. H. Fabrication of Large-Scaled Organic Light Emitting Devices on the Flexible Substrates Using Low-Pressure Imprinting Lithography. *IEEE Trans. Electron Devices* **2005**, *52*, 1722–1726.
253. Lercel, M. J. Self-assembled monolayer electron-beam resists on GaAs and SiO₂. *J Vac. Sci. Technol., B* **1993**, *11*, 2823–2828.
254. Rudawska, A.; Jacniacka, E. Analysis for determining surface free energy uncertainty by the Owen–Wendt method. *Int. J. Adhes. Adhes.* **2009**, *29*, 451–457.
255. Seo, C.; Jang, D.; Chae, J.; Shin, S. Altering the coffee-ring effect by adding a surfactant-like viscous polymer solution. *Sci Rep* **2017**, *7*, 500.